Modulation of gold nanoparticle surface chemistry to target glioblastoma cells for SERS based imaging

Inauguraldissertation

zur

Erlangung der Würde eines Doktors der Philosophie

vorgelegt der

Philosophisch-Naturwissenschaftlichen Fakultät

der Universität Basel

von

Floriana Burgio

von Italien

Basel, 2020

Genehmigt von der Philosophisch-Naturwissenschaftlichen Fakultät auf Antrag Von

Prof. Dr. Uwe Pieles

Prof. Dr. Jörg Huwyler

Basel, den 19. November 2019

Prof. Dr. Martin Spiess
Dekan

Abstract

Surgery is the mainstay treatment of brain tumors, however complete resection is rarely achieved, especially when dealing with grade IV glioblastoma (GBM). GBM is the most lethal brain tumor worldwide with an average survival not longer than 15 months. A reason of this dismal outcome is the lack of intraoperative visualization techniques for the objective identification of true tumor borders and infiltrating tumor cells. Hence, the improvement of GBM visualization during surgical operation is the motivation of this project.

Recent developments of handheld fiber optic probes and lasers for low cost systems, together with sensitivity enhancement techniques such as surface enhanced Raman scattering (SERS), have ruled Raman spectroscopy as one of the most promising technologies for surgical guidance. This technique could overcome the limitations of current intraoperative modalities such as neuronavigation, magnetic resonance imaging and fluorescence guided surgery. For increased sensitivity, metallic nanostructures are preferred because they strongly interact with light, due to surface plasmon resonance (SPR), and produce a much higher level of amplification compared to flat surfaces. Among the nanostructures, gold nanoparticles (GNPs) have found wide application in SERS based imaging studies for their higher biocompatibility and versatile functionalization. When properly engineered, visualization can be targeted on tumor-specific biomolecules providing an accurate mapping of tumor spread. For optimized intraoperative visualization of GBM, detection can be tuned to the near-infrared (NIR) window by acting both on the size and shape of GNPs. This enables to overcome the interfering autofluorescence and to reach a deeper tissue penetration. However, surface chemistry becomes essential to create SERS tags for a fast, sensitive and specific detection of tumor cells.

Due to the absence of comprehensive studies on the impact of GNPs surface functionalization on SERS based imaging, this thesis elucidates the effect of Raman

reporter, inert protective polyethylene glycol (PEG) and anti-epidermal growth factor receptor (EGFR) antibody on colloidal stability, cellular binding specificity, detection sensitivity and speed. EGFR was the target of choice because its gene amplification is the most common molecular hallmark in about 60% of GBM and protein overexpression on cell cytoplasmic membrane makes it easily accessible.

Based on the findings, GNPs with dense surface coverage of Raman reporter or PEG produced the maximum imaging sensitivity and binding specificity, respectively. However, GNPs with dense Raman reporter surface coverage were liable to non-specific binding and colloidal aggregation. Conversely, GNPs with dense PEG surface coverage owned the highest stability but underwent more than 90% reduction of SERS sensitivity. Higher integration time (from 0.05 to 0.5 sec) or shorter working distance (from 16.5 to 0.3 mm) to counteract the decreased SERS sensitivity were not considered in view of the final application *in vivo*. GNPs with surface coverage made of 50% Raman reporter and 50% PEG owned the optimal mixture for an immediate Raman detection of *in vitro* human GBM cells (LN229wtEGFR, BS153 and U87MG) while minimizing non-specific binding on EGFR-negative cells (IMA2.1). Further, SERS signal was comparable independently on the different EGFR expression level or the presence of EGFRvIII in BS153. The latter is the constitutively active receptor whose presence is associated to the lack of response during fluorescence based visualization of GBM. It was also shown that excess of Raman reporter did not add any significant contribution to SERS sensitivity. Similarly, the conjugation efficiency decreased by 35% through the addition of 10 times the concentration of antibody, compared to the lower concentration. This excess quantity of antibody showed no improvement of binding affinity of GNPs to tumor cells.

Because the blood brain barrier (BBB) limits the therapeutic access to brain tumor, the ability of GNPs to cross an *in vitro* BBB made of a monoculture of human endothelial cells (hCMEC/D3) is crucial for successful intraoperative visualization. About 0.1% of GNPs, with specific ratio of immobilized functionalities, was able to cross the cell monolayer preserving its integrity and eliciting no cytotoxic effects. Similar results were obtained *in vivo*.

By providing an in-depth investigation, this work stresses the significance of identifying the appropriate surface chemistry to improve the biomedical potential of

GNPs in SERS based imaging applications. At the same time, it provides an *in vitro* demonstration that SERS based imaging can be implemented intraoperatively for immediate visualization of GBM offering an adequate alternative for the detection of those GBM or low-grade brain tumors that show variable or no response to fluorescence guided surgery, the current state-of-art for GBM intraoperative visualization.

Table of contents

1. Introduction

Up to today, surgery represents the state-of-art treatment in cancer management [1], [2]. It aims at removing entirely the tumor or, if it is not feasible, at reducing its size (debulking tumor) in order to relieve the most severe symptoms and to make subsequent therapies more effective [3]. Complete resection works best for solid tumors limited in a restricted area [4]. In these cases, surgeons are able to remove the solid mass together with a rim of normal tissue around it to make sure that the complete cancer has been excised. However, resection of safety margins is not viable when surgeons deal with tumors located in a sensitive area such as brain where unnecessary removal of normal tissue can lead to impairment of neurological functions and quality of life. Furthermore, a sharp delineation between tumor and healthy brain tissue would facilitate a more complete tumor resection but remains an unmet challenge in high-grade brain tumors as GBM. In fact, GBM has blurred tumor borders due to highly infiltrative tumor cells that invade the surrounding parenchyma hindering the possibility to remove them entirely. Investigation of brain tumor recurrences has consistently shown that 80-90% of these occurs within the original treatment field, identifying as the cause the residual tumor cells due to incomplete resection [5]. Beside subjective assessments such as texture palpation or visual inspection, neurosurgeons can rely on the use of a variety of intraoperative guidance technologies as discussed in the following section.

1.1 Intraoperative glioblastoma guidance technologies

For tailored surgical approach, the state-of-art methods are listed stressing the 'pros' and 'cons' of each.

Neuronavigation is a computational process that combines pre and

intraoperative data creating a translation map between imaging displayed on the screen and real spatial position [6]. Major limitation is the positional accuracy of only 2-3 mm because of intraoperative brain shift due to cerebrospinal fluid loss, decompression and parenchyma displacement [7], [8].

Intraoperative magnetic resonance imaging (iMRI) is based on the same principle as MRI, and either a specific *in situ* donut MRI scanner or a parallel stationary MRI scanner in an adjacent diagnostic room are used [6], [7]. iMRI gives accurate real-time information to be used for further planning optimization and assessment of the progress of the surgery [7]. Senft *et al.* showed its effectiveness: 96% of patients had complete tumor resection compared to 68% in the control group. Although iMRI value is undisputed, its use is limited due to additional operating time (average of 1 h more is required), equipment size and associated costs (5-8 million USD for the installation) [9]. Additional, low magnetic field strength neglects invasive cancer cells and repeated injections or dosages of gadolinium are necessary due to short blood half-life [6], [7], [10].

Intraoperative ultrasonography (iUS) is helpful when the tumor is not isoechoic with the brain or the density difference is greater [11]. Freehand movement of a US probe allows for acquisition of image volume in three dimensions (3D) at any time during surgery [6], [7]. Erdogan *et al.* reported 87% of agreement between iUS and post-operative contrast enhanced MRI in detecting tumor residue in a prospective study of 32 patients [12]. iUS is cheap and easily repeatable but acquisition is operator dependent, interpretation of the images requires training and experience and deep tumors cannot be identified due to low resolution [6], [7].

Intraoperative functional mapping and monitoring are essential for safe excision of GBM when it is near to eloquent brain areas such as somatosensory, motor and language cortex with minimal risks for neurological deficits. While motor mapping can be performed in asleep or awake patients, for language mapping awake surgery is needed [13]. Using these functional methods, resection can be extended to the functional borders placed in the peritumoral tissue invaded by the tumor cells beyond

the anatomical borders [11].

Intraoperative tissue fluorescence has the power to provide real-time information with no interference of brain shift while being still affordable. It demands microscopes equipped with appropriate filters to detect fluorescent light emission of specific agents. Fluorescence can be induced by: i) metabolic activity; ii) passive permeability; iii) targeted probes; iv) and autofluorescence [14].

5-aminolevulinic acid (5-ALA) as a fluorescent pro-agent represents the state-of-art for fluorescence guided surgery of GBM. It was approved in Europe in 2007 while in US in 2017, and it is now used in over 40 countries [7]. 5-ALA is an endogenous metabolite converted to fluorescent protoporphyrin IX (PPIX), which chelates with iron in presence of enzyme ferrochelatase (FECH) to produce heme. Heme is then converted into bilirubin by heme oxygenase-1 (HO-1) [15]. In most of GBM cells, FECH enzyme is missing or has reduced activity resulting in the accumulation of PPIX into the tumor tissue. When excited with blue-violet light, PPIX emits a red fluorescence allowing for differentiation between tumor and healthy cells. 5-ALA derived fluorescence has been shown to be more sensitive compared to preoperative MRI contrast enhancement and positron emission tomography (PET) [16], [17]. Higher sensitivity enabled surgeons to achieve a double rate of complete resection and 6 months progression-free survival rates than patients who underwent conventional microsurgery under white light. Typically, 5-ALA is administered orally to the patients 4 h before the operation at a dose of 20 mg/kg body weight [18]. Nonetheless, this methodology faces several hurdles: i) low-grade gliomas do not respond to the administration; ii) fluorescence is not homogeneous in the periphery of the tumor and depends on the cell density; iii) false positive cases have been reported due to the presence of reactive astrocytes and macrophages [14], [19]–[22]; iv) sensitivity to prolonged exposure of light decreases the contrast; v) and penetration depth achieved with blue light is shallow [23]. Conversely, GBM cells do not show fluorescence depending on the EGFR activation and the presence of its constitutively active variant, EGFRvIII. Indeed, receptor activation has a downstream effect on HO-1, whose activity results in accelerated heme depletion with consequent shift of enzymatic activity in favor of increased PPIX metabolism by FECH (Figure 1) [15]. In attempt to reduce fluorescence variability in GBM cell lines and to

achieve a more objective fluorescence visualization, recent findings have shown the possibility to increase the signal pharmacologically and to quantify the concentration of PPIX by mean a microscope (Qp9-microscope) specially built for this purpose [24].
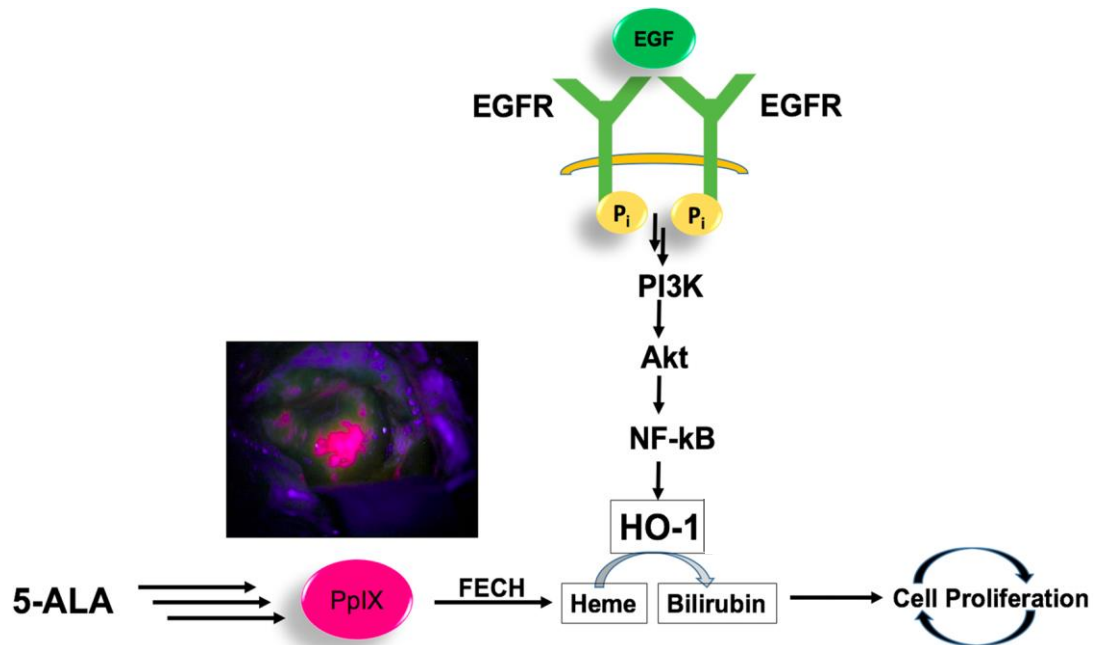
Figure 1. 5-ALA metabolism and its connection with EGFR activation in GBM cells. 5-ALA is metabolized into PPIX, which after excitation allows for visualization of the tumor as pink mass. Upon binding of the EGF, receptor activation promotes HO-1 activity, through the PI3K/AKT/NF-κB cascade, inducing the conversion of heme in bilirubin and the reduction of PPIX in the cells [15].

Fluorescein and indocyanine green (ICG) are responsible of passive permeability induced fluorescence. Accumulation follows the principle of the enhanced retention and permeability (EPR) effect therefore is not tumor specific. Fluorescein displays a yellow-green fluorescence visualized by the naked eye at high dose of 5-10 mg/kg body weight [7], [11]. Due to limited specificity and sensitivity concerns, surgeons risk to remove healthy tissue or to leave behind tumor tissue, respectively [25]. ICG stains tumoral and peritumoral blood flow and vascularization. The typical dose is 0.3 mg/kg body weight. It emits in the NIR region allowing for a deeper visualization in the tumoral tissue. Non-specific binding to proteins and rapid clearance (t1/2 ≤ 5 min) are the main drawbacks in the brain tumor surgery [7].

Next generation fluorophores contain targeted agents to address tumors. With high specificity and low toxicity, they have already reached the early clinical trials phase. Some examples are alkyl-phosphocholine analogues, chlorotoxin (TumorPaint), EGFR-

targeted or αvβ3 integrin-targeted agents and phospholipids nanoparticles. All of them are usually conjugated to NIR fluorophores [14].

Implementation of Raman imaging as an adjunct technique for neurosurgical guidance has gained special focus due to its undoubtedly potential (Figure 2). First, it requires no need of either labeling or complex sample preparation; second, it is non-invasive and non-disruptive causing no harm to the patient; third, high spatial resolution, sensitivity and selectivity enable a fast and real-time discrimination between malignant and benign tissue even down to molecular level, preventing removal of normal tissue and minimizing the volume of residual tumor with a considerable positive impact on patient survival [26]. All these features make Raman imaging able to address the main current clinical matter: the lack of intraoperative methods with sufficient or clinically relevant sensitivity and specificity for an objective identification of the tumor margins and the microscopic infiltrating foci [27].

The feasibility of Raman imaging for neurosurgical guidance has been explored by several groups. It was used to delineate tumor tissue, both *ex* and *in vivo*, in a human GBM xenograft mouse model and in human brain tumor surgical specimens resulting in a near perfect agreement between Raman detection of tumor infiltration and histological staining [28]. Likewise, it was employed to distinguish GBM from gray matter and necrosis with 99.6 and 97.8% accuracy in the training set and validation cohorts, respectively [29]. A miniaturized handheld fiber optic probe was adopted to discriminate cancer cells from the surrounding non-cancerous tissue due to their intrinsic fingerprint spectra. Real-time information were obtained *in vivo* in 17 patients during brain tumor resection with at least 90% accuracy and resolution of as few as 17 cancer cells/0.0625 mm^2, overcoming 5-ALA induced fluorescence that mainly revealed bulk tumors [30].

Beside label free detection, nanoparticles based labeling has been introduced to counteract the intrinsically weak signal of Raman spectroscopy making it a much more powerful tool. Gold core-satellite assembly nanoparticles were used to clearly distinguish fixed or living GBM from normal cells with a Raman intensity 5 to 15 times higher for GBM [23]. Similarly, integrin-targeted surface enhanced resonance Raman spectroscopy (SERRS) nanoparticles were shown to depict the true tumoral microscopic

extent *in vivo* in a GBM mouse model with a detection sensitivity in the femtomolar range [31]. The handheld fiber optic probe described above was adopted in conjugation with silica SERS nanoparticles in a GBM mouse model reducing the acquisition time from 10-20 to 0.1 s. Furthermore, SERS nanoparticles suffer from negligible loss in signal over time. Compared to the instrumentation commonly present in the operation room, the handheld scanner has the advantage of being easy to handle and flexible allowing to investigate the tumor resection bed from any directions [5].

In attempt to improve surgical outcomes, multimodal brain imaging has been assumed. Triple-modality nanoparticles were designed to combine MRI, photoacoustic and Raman imaging and the key factors of each of these techniques: localization of brain tumor and delineation of its margins before and during the operation using MRI; high spatial resolution and 3D imaging using photoacoustic; high-sensitivity, specificity and surface resolution of tumor margins using Raman [10]. pH-responsive nanoparticles were designed for guiding brain tumor visualization and resection by sensing acidic tumor microenvironments via simultaneous activation of MRI and SERRS. The acidic environment, typical of solid tumor, promoted nanoparticles self-assembly while those diffusing in the normal brain, at neutral pH environment, were washed away. Since extracellular acidification is a hallmark of all solid tumors, this strategy does not depend on tumor genotypes or phenotypes [32].

Figure 2. Schematic representation of Raman guided surgery. A) The main tumor mass is resected (black shadow). B) Raman fingerprint spectrum allows to identify and to remove residual cancer cells and infiltrating foci on the edges and beyond the resection cavity. C) Complete removal of tumor mass is achieved.

Engineered nanoparticles, together with Raman spectroscopy, have the potential to revolutionize the diagnosis and treatment of brain tumors. A deep and full characterization of their surface functionalization is required since it affects their performance in terms of colloidal stability and their interaction with cells in terms of

sedimentation, dissolution, formation of a protein corona and binding specificity. The most common approach to functionalize nanoparticles as SERS tags is illustrated in figure 3.
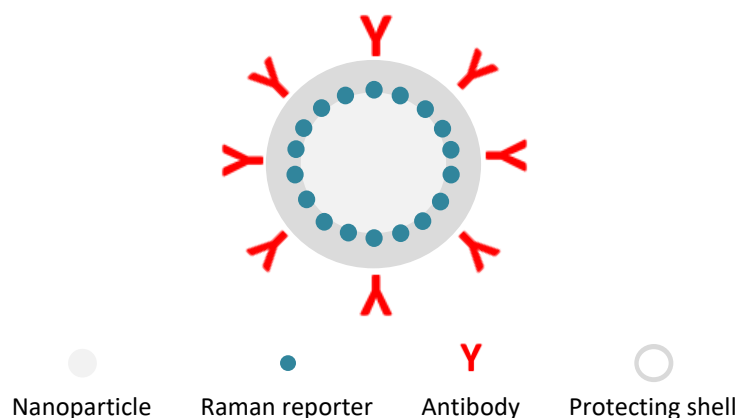
Figure 3. Schematic structure of a SERS tag. The Raman reporter molecules encase the nanoparticle. A protective shell made of a polymer increases the stability and provides the surface to attach the antibodies.

A nanoparticle is surrounded by a layer of Raman reporter (a Raman active molecule), followed by a protective shell. To target specifically SERS tags to tumor, antibodies or other affinities ligands are used [33].

Non-specific binding can represent a bottleneck in improving detection sensitivity and tagging specificity. Nanoparticles tend to be "sticky" and to bind non-specifically to the cellular membrane causing high levels of background that degrades the signal-to-noise ratio and produces false positives [26], [34], [35]. This effect highlights the importance of controlling surface modification to find an optimum balance between inert and receptor specific active functionalities in order to achieve maximum SERS intensity and minimize nanoparticle non-specific interactions [35].

In this thesis, SERS based imaging is the technique that has been investigated for improved intraoperative visualization of GBM cells. Hence, elucidation of the optical methodology behind this technique as well as of its evolution over the time is reported in the upcoming section.

1.2 Raman spectroscopy

Raman spectroscopy is an optical methodology measuring the frequency shift of the inelastic scattering of light. When a monochromatic laser beam hits the molecule, energy is exchanged between intramolecular vibrations bonds and photons producing a change in the bond's vibrational state. Most of the scattered photons has unaltered energy (elastic or Rayleigh scattering). Minor part of scattered photons experiences a change of energy (inelastic or Raman scattering). Gain of energy is termed anti-Stokes, whereas loss of energy is termed Stokes (Figure 4) [36].
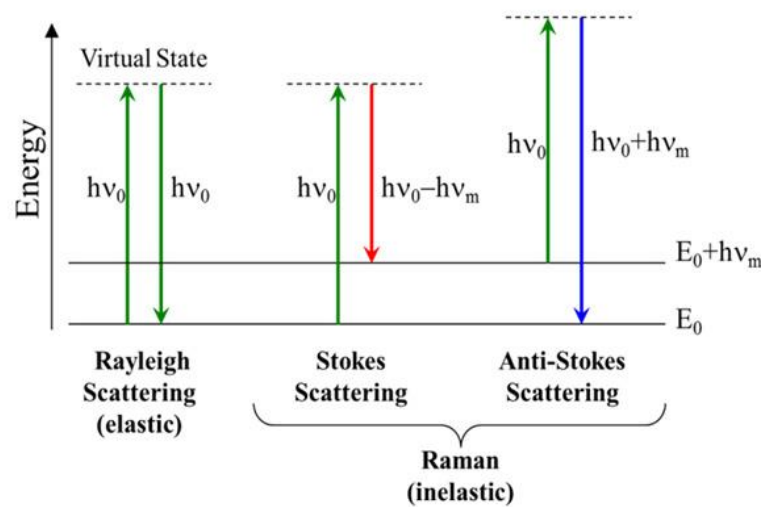
Figure 4. Jablonski diagram representing quantum energy transitions for Rayleigh and Raman scattering. After interaction with the incident photon, the molecule is excited to a virtual energy state. If the energy of the emitted photon, when the molecule relaxes to a lower energy level, is equal to that of the incident photon, the process is elastic and it is known as Rayleigh scattering. If the energy is lower or higher, the process is inelastic and it is known as Stokes or Anti-Stokes scattering, respectively [37].

This change in the photon's energy is known as 'Raman shift'. Collision of photons with different biochemical bonds within the tissue generates several Raman shifts, which taken together generate the 'Raman spectrum'. The Raman spectrum gives fingerprint information that resolve the molecular composition in cells or tissues providing a truly objective picture of the pathology. The intensity of Raman scattering is proportional to the magnitude of the change in the molecular polarization where polarizability results from the displacement of the electrons from the equilibrium position as a consequence of the molecular vibrations [36]. However, the weakness of spontaneous Raman scattering (for every 1-10 million photons bombarding a sample, only one will result in

Raman scattering) has hindered the spread of Raman spectroscopy until advanced instrumentation and enhancement Raman techniques have been discovered (Figure 5).
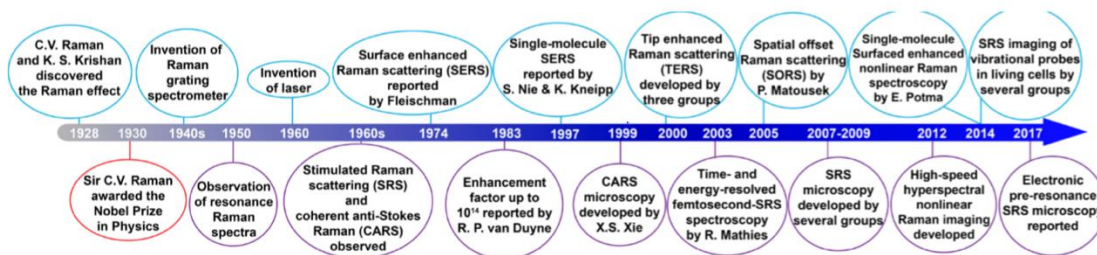
Figure 5. Evolution of Raman spectroscopy. Raman spectroscopy timeline from its discovery to the most recent advanced techniques [38].

1.2.1 Evolution of Raman spectroscopy

In resonance Raman scattering (RRS) the excitation wavelength is chosen to overlap with (or be very close to) an electronic transition. This typically means in an area of ultraviolet-visible (UV-Vis) absorption. Such overlap boosts the scattering efficiency by factors of 10^2-10^6. However, since the excitation falls in the UV-Vis region, fluorescence background represents a substantial problem [39].

Coherent anti-Stokes Raman scattering (CARS) uses three laser fields instead of the traditional single laser. They are a pump field at frequency of ω_p, a Stokes field at ω_S and a probe field at ω_{pr}. When the energy difference of the pump and Stokes beams (ω_p–ω_S) equals the frequency of a molecular vibration mode (Ω), the Raman resonance occurs. This resonance is then probed by the third field at ω_{pr} generating an anti-Stokes field at (ω_p–ω_S+ω_{pr}) [40]. The Raman active mode of interest is the only extremely strong peak in the Raman spectrum providing a speed advantage over spontaneous Raman.

Like CARS, stimulated Raman scattering (SRS) is based on two incident photons but produces a signal at the same frequency than the excitation wavelength. Thus, SRS offers a linear dependence on concentration and shows identical spectra to spontaneous Raman with no interference complications from the non-resonance background like in CARS [41].

Tip enhanced Raman spectroscopy (TERS) combines the spatial resolution of atomic force microscopy with the chemical information of Raman spectroscopy. An excitation laser beam is pointed on the apex of a metallic coated tip creating a confined and enhanced electromagnetic field. Sample, positioned at nanometer distance from the tip, experiences this enhancement leading to an increased Raman scattering [41].

Surface enhanced hyper Raman scattering (SEHRS) is the two-photon excited analogue of SERS (see next paragraph). SEHRS allows to acquire complementary spectroscopic information for improved understanding of molecule–nanostructure interactions and to probe molecules at lower concentrations due to higher sensitivity [42].

SERS is a surface sensitive technique that results in the enhancement of Raman scattering when molecule is absorbed on a metal surface allowing for its highly sensitive structural detection at low concentrations [41]. Given the importance of this technique in this work, the concepts judged important for a clear understanding are emphasized below.

1.2.2 Surface enhanced Raman spectroscopy

1.2.2.1 Localized surface plasmon resonance

SERS enhancement comes mainly through the electromagnetic effect (Figure 6A), which takes advantage of a unique phenomenon on certain metal nanoparticles called localized SPR (LSPR). It is an optically excited electron wave resonance state that happens when the conductive band electrons at metallic nanostructure surface (localized surface plasmons) are excited by an external electromagnetic field (Figure 6B). The coherent oscillation of electrons generates a secondary electromagnetic field, which is added to the external electromagnetic field resulting in a signal intensity amplification. This makes nanoparticles highly sensitive transducers of small changes in the local refractive index. These changes become visible as a red shift of the absorption spectrum of the molecules upon coupling on the nanoparticles [43], [44]. The SERS enhancement factor is typically 10^6–10^8-fold [33].
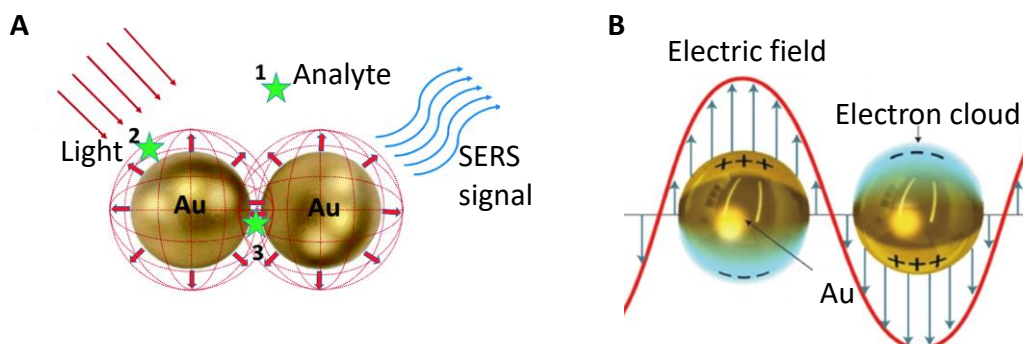
Figure 6. Illustration of SERS and LSPR. A) SERS consists in the enhancement of the Raman scattering when the analyte is attached or close to the metal surface (position 2). The analyte undergoes the highest electromagnetic field in the 'hot spot' where the metal particles are close (position 3). The further the analyte, the weaker the electromagnetic field (position 1) [adapted from 45]. B) SERS enhancement is attributable to the LSPR effect generated from the collective oscillation of electrons in response to an external electric field [46].

A smaller contribution to the enhancement is instead given from a charge transfer effect between the absorbed molecules with appropriate acceptor or donor orbitals and the metal substrate. This process is also known as first layer effect because the molecules directly in contact with the surface of the nanoparticles mainly contribute to chemical effect and exhibit a stronger enhancement in comparison to the adjacent layers [43], [44].

1.2.2.2 Substrates for SERS

Good SERS substrates are rough electrodes or colloidal suspensions made of gold, silver or copper. They are strongly wavelength-dependent meaning that exhibit a good enhancement in a limited excitation wavelength range. Most SERS substrates are designed to operate with visible/NIR excitation (400-1'000 nm), which is the typical range of interest for molecular Raman scattering experiments [36]. Silver produces the highest enhancement factor because interband transitions fall in the UV range leading to reduce absorption in the visible or NIR range. Conversely, in case of gold and copper, interband transitions fall in the visible range reducing SERS amplification [47].

1.2.2.3 Intrinsic and extrinsic detection methods

Two detection methods can be distinguished: intrinsic and extrinsic. Intrinsic SERS targets the molecule of interest directly supplying structural information useful to

identify even small difference between similar samples. However, the targeted molecule needs to be Raman active and its concentration high enough to be detected. Instead, extrinsic SERS detects the targeted molecule indirectly because it marks a Raman reporter. This detection method requires further functionalization in order to target the molecule of interest [33].

1.2.2.4 Influence of chemico-physical properties of nanoparticles on SERS

For optimized SERS enhancement, LSPR position can be tuned due to its dependence mainly on the size, shape and aggregation state of nanoparticles. Increased size causes a red shift of LSPR and higher SERS intensity because of the presence of more available electrons. However, this is valid until nanoparticles size approaches the scale of the excitation wavelength: for these particles the enhancement diminishes due to the radiation damping effect. When particles are too small, the effective conductivity and light scattering properties diminish [48], [49]. In addition to the position, the morphology also changes the number of LSPR peaks accordingly to the way in which nanoparticles can be polarized. While nanospheres present only one peak, nanorods have two peaks, once longitudinal and the other one transversal. The highest SERS enhancement up to 10^{14}-fold is usually recorded in localized areas known as 'hot spots'. They can be either gaps smaller than 2 nm, formed when two or more nanoparticles cluster, or sharp corners and tips in anisotropic nanoparticles. In the latter case, the lightning rod effect causes the dipolar field to be focused at the tip allowing the nanoparticles to behave as an optical antenna. The analyte does not need to be in direct contact with the surface of nanoparticles. Indeed, it has been reported that SERS enhancement extends to a distance of 10 nm but diminishes following the distance dependence: $I = (1 + r/a)^{-10}$, where I is the SERS intensity, a is the radius of the nanoparticle and r is the distance of the analyte from the metallic surface [43], [50]. In case of extrinsic SERS, it is worth mentioning that the selection of both the Raman reporter and the protective coating layer plays a role in the final electromagnetic enhancement. The Raman reporter must: i) be polarizable to be Raman active; ii) be photostable for prolonged exposure to the laser with no significant decay of the signal; iii) and have high binding affinity to elicit chemical enhancement mechanism. Molecules

with sulfur or amine, such as DTTC, R6G, crystal violet and some small molecules containing thiol such as p-BDT, are preferred because they strongly bind to gold via the gold thiolate bond [51]–[54]. A study comparing two organic chromophores, malachite green (MG) and its isothiocyanate derivative (MGITC), showed that the enhancement factor of MGITC was ~200-fold higher than MG under the same experimental conditions [55]. Fluorescent dyes and other chromophores are often used because they have large Raman scattering cross sections. Raman reporters can also match the excitation wavelength inducing SERRS and further enhance the Raman signal [31]. Beside existing Raman reporters, molecules can be specially synthesized for improving their binding to gold. For instance, lipoic acid was added to a triphenylmethine dye as a linker to covalently attach the reporter on gold colloid [56]. As alternative, molecules positively charged can be coupled to negatively charged nanoparticles although they can be prone to desorption.

About the SERS protective coating, it should not interfere with the detection of the Raman reporter and it should not cause its displacement [33]. The protective shells consist of mono or multilayers of polyelectrolytes or silica even though the latter was reported to cause adsorption competition with Raman reporter or reduction of SERS signal up to 60% [5], [10], [57]–[60]. PEG is often preferred because it prevents reporter leaching and nanoparticles aggregation [32], [53], [56]. Most important, PEG significantly improves circulation time of nanoparticles, a necessary requisite for GBM imaging as discussed in depth shortly [59], [61].

1.2.2.5 Chemico-physical properties of nanoparticles for SERS based imaging of glioblastoma

Of all nanostructures, application of GNPs as SERS tags for SERS guided surgery is based on three major advantages, i.e., remarkable biocompatibility, negligible toxicity and amenability to functionalization [62]. Formulation of an ideal molecular imaging agent requires satisfying some criteria. It must: i) avoid opsonization and clearance by the reticuloendothelial system (RES); ii) be selectively delivered to the brain and be able to cross the BBB; iii) be extensively retained in the tumor so that a single injection is enough for preoperative planning and intraoperative resection; iv) emit a signal stable for the

whole duration of the surgery that lasts in average 4 h; v) and be active in the NIR region known as a 'clear window' for optical imaging because the blood and water absorption spectra are minimal and the depth of penetration is higher [31], [62], [53]. All these features can be tailored by controlling the physico-chemical properties of GNPs. Both size and shape contribute to clearance, *in vivo* biodistribution, strength of adhesion and internalization rate in the cells and SERS enhancement. Particles of 60-80 nm are the most efficient for SERS in the NIR region [53]. GNPs smaller than 5 nm are rapidly eliminated through renal clearance [63], [64]. GNPs bigger than 200 nm are usually prone to opsonization. Proteins of the immune system, known as opsonins, are absorbed on the GNPs surface so that monocytes and macrophages can promptly recognize, remove from the blood stream and bring the GNPs to the liver, spleen and bone marrow [63]. Considering that blood and liver account for the accumulation of approximately 70-80% of the injected GNPs, the gold bioavailability in the brain is limited for imaging [65]. Different strategies can be applied to improve circulation time. Neutral surface charge reduces recognition by the RES but, at the same time, makes GNPs susceptible to aggregation. Positive or negative charge increases macrophages uptake but improves particles stability and their interaction with the cells. Alternatively, addition of PEG can create an extra hydration layer resulting in a 'stealth' behavior and circumventing the RES [61], [63].

1.2.2.6 Passive and active targeting of glioblastoma

Passive permeation of PEGylated GNPs within transport-permissive brain microvasculature is a size-dependent process with respect to both GNPs core size as well as PEG chain length [66]. Approximatively 0.3% of 10 nm GNPs was shown to pass through the BBB after 24 h from the injection and this percentage dropped as soon as size increased [65]. However, accumulation of GNPs with a final size of 120 nm was successfully reported in GBM bearing mouse [5], [10].

To improve the passage of GNPs through the BBB and to enrich the amount of gold in the brain, an effective strategy is the active targeting. It relies on two kinds of transports: absorption mediated transport (AMT) and receptor mediated transcytosis (RMT). AMT uses cation proteins or cell-penetrating peptides to trigger the interaction between the

GNPs and the negatively charged membrane of brain capillary endothelial cells. Nevertheless, it is a non-specific process leading to accumulation of GNPs in non-targeted or non-diseased area. For increased targeting specificity, RMT appeals for immobilization of target receptor specific biomolecules on the GNPs surface. Targeting moieties commonly used for GBM are: i) proteins such as transferrin, fibroblast growth factor and low-density lipoprotein-receptor-related protein-1; ii) peptides such as trans-activating transcriptor and RGDyK; iii) and antibodies against transferrin receptors or EGFR [61], [67]. Antibodies can be employed in their native form, as single-chain variable fragments or affibodies [53], [68]. Conjugation of these ligands allows for a remarkably more intense and lasting tumor enhancement with respect to the unconjugated counterpart.

Among the different brain malignant tumor types, GBM was chosen because this tumor is considered the most challenging to resect due to the diffuse pattern of tumor spread. Detailed definition, classification, diagnosis and strategies of treatment are described in the following section.

1.3 Glioblastoma

Gliomas account for the 80% of malignant brain tumors arising from glial cells such as astrocytes, oligodendrogliomas or ependymal cells [69]. According to the 2016 World Health Organization (WHO) classification, which takes into account the molecular parameters in addition to the histopathologic appearance, two main categories can be defined: i) diffuse gliomas whose main feature is a highly infiltrative pattern in the central nervous system parenchyma; ii) and more circumscribed gliomas of which astrocytoma and ependymomas are the most representative [70]. Constituting more than 50% of all gliomas, grade IV GBM is the most frequent tumor belonging to former category (Figure 7) [69], [71].
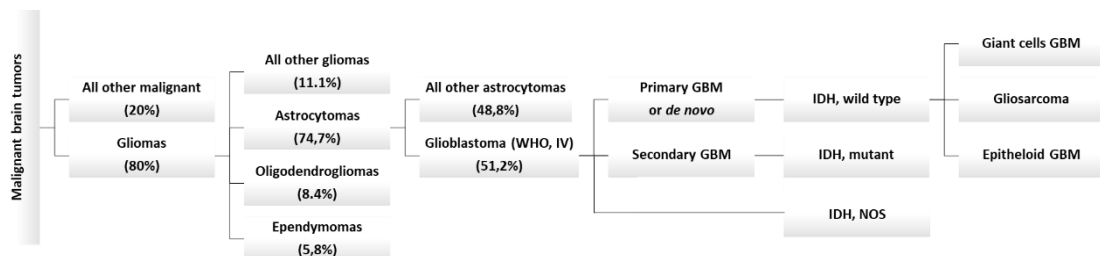
Figure 7. Statistical distribution of gliomas and classification of GBM according to the 2016 WHO.

GBM can be primary or secondary depending on whether it appears *de novo* or it progresses from a lower WHO grade tumor, respectively. Primary GBM is more common in men with a median age of 62 and only 8.8% is diagnosed in children. Conversely, secondary GBM affects mainly women with a median age of 45 [71].

Even though GBM was thought to be characterized by a heterogeneous histological appearance only, whence the name multiforme, newly acquired knowledge regarding molecular abnormalities or genetic alterations has led to the definition of specific GBM types. Based on the presence or absence of isocitrate dehydrogenase (IDH) gene mutations, it is possible to distinguish: i) GBM: IDH-wildtype; ii) GBM: IDH-mutant; iii) and GBM: NOS (not otherwise specified). Primary GBM is IDH-wildtype and it is further discriminated in giant cells GBM, gliosarcoma and epithelioid GBM. IDH catalyzes the conversion of isocitrate into α-ketoglutarate within the citric acid cycle. Present in secondary GBM, IDH mutation causes a hypermethylation phenotype, changes in cellular metabolism and responses to hypoxic and oxidative stress. The third category,

GBM: NOS, encompasses all kind of GBM lacking of specific information to be assigned to one of the previous classes [11].

1.3.1 Etiology, incidence and prognosis

Its formation cannot be prevented since the exact causes remain elusive although exposure to ionizing radiation might be associated with an increased risk of glioma [69], [71]. It has a global incidence of two to three per 100.000 adults per year and a median survival rate not longer than 15 months [11], [71]. This disheartening prognosis makes GBM the most challenging and lethal brain tumor worldwide.

1.3.2 Unique challenging features

GBM consists of a mass with a central necrotic core surrounded by thick and irregular margins. Abnormal accumulation of fluid (infiltrative edema) around the tumor causes further brain swelling exacerbating the symptoms (Figure 8A). The following features make the clinical management arduous and challenging:

- Localization: GBM is usually localized in the supratentorial compartment. Lesions have origin in the deep white matter to infiltrate often into the cortex. In the worst case, it can extend across the corpus callosum to the opposite hemisphere assuming the characteristic butterfly shape (Figure 8B). GBM rarely forms metastases outside of the central nervous system [71];

- Highly infiltrative pattern: cells invading individually or in small groups the normal brain parenchyma are hallmarks of GBM. Invasion occurs preferentially along the existing brain structures but even through the blood vessels and the white matter. Infiltrating tumor cells usually form deeply seated structures beyond the margins for maximal resection eluding the current visualization technique and giving rise to tumor relapse [68];

- Resistance or limited response to conventional therapies: GBM cells are not only resistant to chemotherapy and ionizing radiation, but those conditions prompt them to invasive behaviors [72].
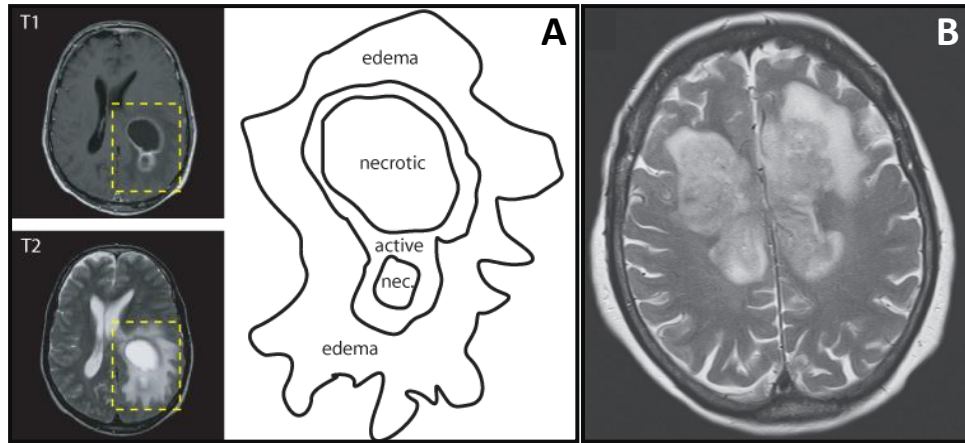
Figure 8. Illustration of GBM structure. A) T1 and T2-weighted images of GBM and a schematic representation of GBM structure: a necrotic core with asymmetric margins is surrounded by edema [73]. B) MRI image of a bifrontal lesion across the corpus callosum with the butterfly shape [74].

1.3.3 Aberrations of epidermal growth factor receptor

The most common alteration concerns the EGFR. EGFR belongs to the ErbB receptors family with tyrosine-kinase activity. It is a single chain transmembrane protein of 170 kDa made up of three domains: i) an extracellular ligand-binding domain; ii) a hydrophobic transmembrane domain; iii) and a cytoplasmic domain with tyrosine kinase activity (Figure 9). The binding of the ligand to the ectodomain promotes the formation of transient homo or heterodimers and autophosphorylation of tyrosine residues within the carboxy terminal tail of the receptors. This recruits several cytoplasmic proteins, which initiate an intracellular signaling via several pathways leading to cell proliferation, survival, apoptosis, invasion and migration [75]. These pathways include the phosphoinositide 3-kinase, mitogen-activated protein kinase, signal transducer and activator of transcription 3 and Src family kinases [76].

Dysregulated EGFR signaling is a frequent hallmark that leads to a more aggressive GBM phenotype. This can be due to mechanisms such as EGFR overexpression at the cell membrane, enhanced autocrine activation or *EGFR* mutation and malfunction in receptor degradation. Occurring in almost 60% of primary GBM, while only in 10% of secondary GBM, EGFR overexpression is often a consequence of *EGFR* focal amplification at 7p12 or mutation. Approximately 50% of GBM overexpressing EGFR also shows concomitant expression of its truncated yet constitutively active form: EGFRvIII [76], [77]. EGFRvIII is a tumor specific mutation arising from an in-frame

deletion of exons 2–7 of the coding sequence that results in a shorter extracellular domain (Figure 9). EGFRvIII has a molecular mass of approximately 145 kDa [78]. Due to low level of autophosphorylation, receptor internalization is defective causing a longer presence at the cell surface and amplified mitogenic effects [79]. EGFRvIII expression has been associated with a dismal prognosis since GBM becomes resilient to therapies [76].
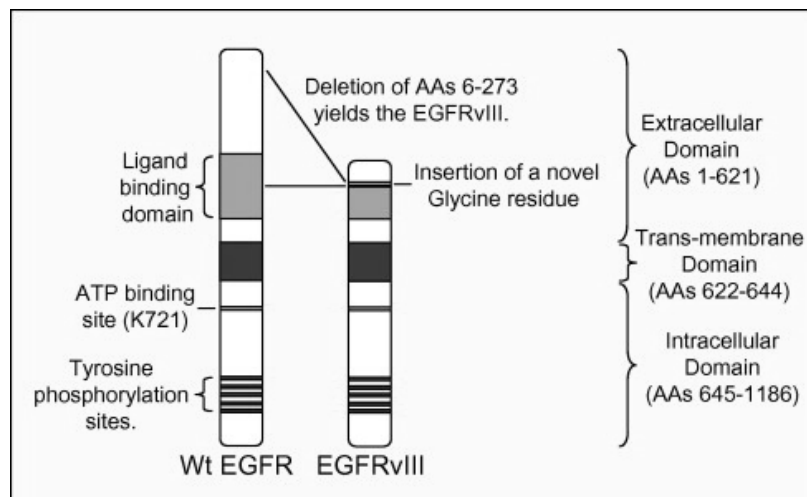
Figure 9. Schematic representation of EGFR wild type and EGFRvIII. EGFR consists of three domains: extracellular with the ligand binding site, transmembrane and intracellular. EGFRvIII lacks amino acids 6–273 and presents a new glycine residue between amino acids 5 and 274. This deletion makes the receptor constitutively active and ligand-independent [80].

1.3.4 Diagnosis

Depending on the part of the brain where the GBM initiates, symptoms may vary from non-specific headaches to specific neurological deficits and disturbances such as:

- Changes in mood and in ability to think;
- Changes in sensory and memory issues;
- Speech difficulty;
- Seizures [11], [3].

In addition to a neurological exam, the diagnosis is refined with imaging evaluation through MRI, PET and computerized tomography (CT) scan. CT is a fast and inexpensive method to supply initial data but MRI, with and without gadolinium contrast media, is usually preferred due to higher accuracy in sense of extension and specificity. Instead, PET uses biochemically active molecules labeled with radiotracers such as the glucose analog 18F-fluorodeoxyglucose to provide metabolic information of the tumor.

However, to achieve a correct diagnosis, histological assessments of sample obtained either by biopsy or resection should be performed [11].

1.3.5 Treatment

First line of treatment of GBM is surgery followed by radiotherapy and chemotherapy. However, when lesion is too extended or close to sensitive areas, biopsy could be preferred since it carries fewer risks compared to the complete resection [81].

As stated above, surgery still remains the state-of-art treatment in GBM management. Increasing the extent of resection to a minimum of 70% of the initial tumor volume has been associated to a more favorable prognosis with a nearly 5-months or greater than 40% increase in survival [82], [83]. Nonetheless, complete resection is achieved in fewer than 20% of cases [18].

Radiotherapy uses external high-energy beams, such as X-rays or protons, to kill or slow the growth of tumor cells. Specialized delivery systems direct radiations at the site of the tumor while minimizing the radiation dose to the surrounding brain. Although radiotherapy hits even the healthy cells, by the time the next treatment is given, most of them can repair the damage. This process is repeated for a total of 10 to 30 treatments, usually given once a day, 5 days a week [84].

Chemotherapy is based on the use of Temozolomide (TMZ) or Lomustine (also referred as CCNU). They are alkylating agents that act by introducing a DNA mismatch in the replication cycle leading to cell death [1]. A daily dose of 150 to 200 mg/m^2 of body-surface area is administered for 5 days every 28 days. Concomitant treatment with radiotherapy plus TMZ has shown to improve survival [85]. Common side effects arising from both types of treatments are fatigue, nausea, swelling, infertility and stroke [86].

Recently introduced, tumor treating field (TTF) is a new technology that relies on the application of a low intensity, intermediate frequency and alternating electric field to inhibit cell mitosis. TTF restrains DNA damage repair, impairs cellular migration and

invasion and upregulates autophagy [87]. The use of TTF together with TMZ has shown to improve progression-free survival and overall survival [88].

Novel approaches are under investigation such as vaccines, angiogenesis or small molecule tyrosine kinase inhibitors, monoclonal antibodies and RNA-based agents. Being a signature of GBM, it is not surprising that EGFR has been frequently chosen as first target of therapy.

So-called small molecules tyrosine kinase inhibitors such as Gefitinib (Iressa®) and Erlotinib (Tarceva®) interfere with tyrosine kinase activity of the receptor thus altering the signal transduction cascade. None of these molecules has been approved for GBM due to unacceptable side effects, limited efficacy or difficult brain penetrance [79].

Monoclonal antibodies usually prevent the binding of the cognate ligand to the relative receptor. Bevacizumab (Avastin®) targets the vascular endothelial growth factor receptor and blocks the generation of new tumor-associated blood vessels [1], [2]. It is clinically used only for recurrent disease and symptoms alleviation. Cetuximab (Erbitux®) acts on the EGFR as an antibody-blocking with no receptor activation. It is also believed to induce receptor internalization and destruction [79]. Monoclonal antibody, mAb806, has been engineered for targeting the EGFRvIII. It recognizes a region usually hidden in EGFR impairing receptor autophosphorylation. Recent studies have shown that different mutations of EGFR cause conformational changes making the hidden region accessible to the antibody [89].

Receptor inhibition can be even achieved at the transcription or translation level by mean antisense RNA, RNA interference and ribozymes. Pre-clinical outcomes in this field are very promising [1], [79].

Feasibility and safety of so-called chimeric antigen receptor-T cells have been shown in the treatment of GBM. Patients own T cells are modified in the lab to recognize the EGFRvIII. After recognition, primary T-cell activation occurs and leads to cytokines

release, degranulation and T-cell proliferation [90].

One of the reasons why GBM is so aggressive and difficult to treat is the presence of the BBB, which precludes access of a wide variety of therapeutic or imaging agents to the tumor [91].

1.4 The blood brain barrier

The BBB is a highly selective semipermeable interface between the blood circulation and the central nervous system at the microvasculature level, whose main task is to protect against circulating harmful substances or pathogens that could cause brain infections, while allowing vital nutrients to reach the brain [92]. The first line of this barrier consists of a monolayer of endothelial cells delimiting the capillary lumen. It is characterized by tight cell-cell junctions (TJs) and a lack of fenestrations. The presence of TJs reduces the paracellular movement of substances and contributes to the high transendothelial electrical resistance (TEER) of >1,500 $\Omega*cm^2$ [92]. However, transcellular transport is still allowed due to the presence of several classes of nutrient transporters and efflux pumps (Figure 10) [93].
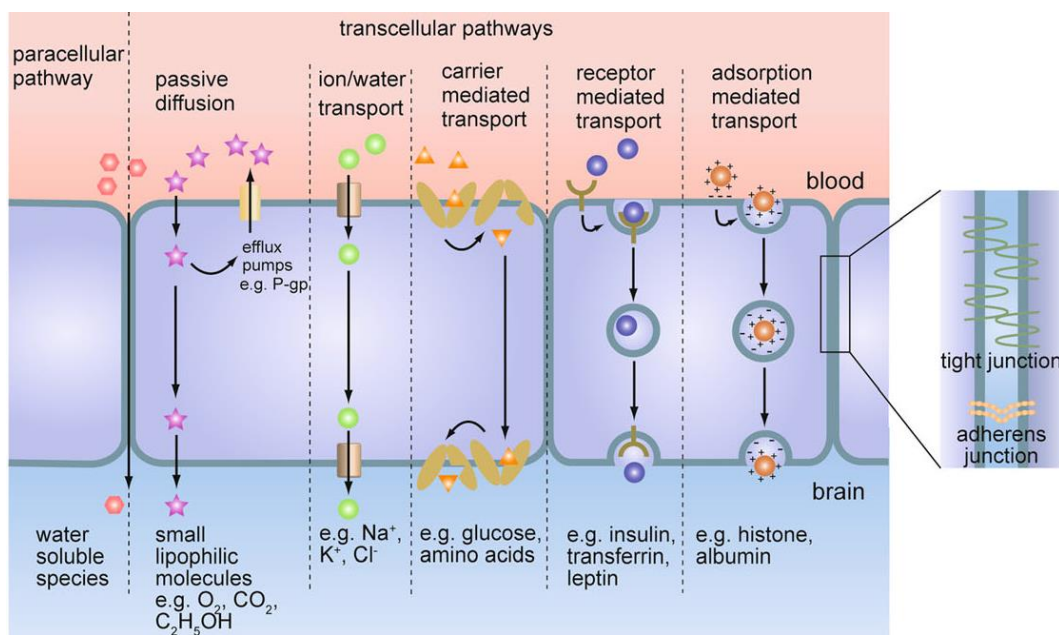
Figure 10. Transport system at the BBB. Despite TJs reduce the paracellular transport, the passage of substances is possible through transcellular pathways. Solute carrier family allows the passive transport of polar nutrients such as glucose and amino acids. Efflux pumps of the ATP-binding cassette superfamily pump out potentially toxic substances; while larger molecules and proteins such as transferrin, insulin and IgG are delivered through RMT or AMT [93].

Pericytes stick to the endothelial cells on the abluminal side. Both cell types are enclosed by the basal lamina, a membrane of 30 to 40 nm contiguous with the plasma membrane of astrocyte end-feet (Figure 11A). It is composed of collagen type IV, heparin sulfate proteoglycans, laminin, fibronectin and other extracellular matrix proteins. Main

components of the TJs are transmembrane proteins such as junctional adhesion molecules, occludins and claudins. In the cytoplasm, there are several accessory proteins associated with them. The most known are the zonula occludens (ZO) proteins, which belong to the membrane-associated guanylate kinase family [94]. When tumor occurs, BBB integrity is damaged due to extensive abnormal angiogenesis and loss of TJs with the consequent formation of large gaps. These gaps may measure as much as 0.5 to 1 nm, although smaller gaps are more common. Together, they open a direct communication between the vascular lumen and the basement membrane or directly to the brain parenchyma. Indeed, in the most abnormal vessels, the basal lamina is absent or, if present, is a thin and irregular line. In addition, the glial sheath is represented only by rare tumor cells close to the basal lamina with large areas of the basal lamina in direct continuity with the extracellular space (Figure 11B) [95]. This disruption enables on one hand the spread of tumor cells through the blood with formation of metastasis, on the other hand the increased extravasation of agents from the blood into tumor tissue. Such behavior is the base of EPR effect [96]. However, BBB disruption is not uniform and tumors often contain subregions with intact and especially robust BBB (or blood tumor barrier, BTB), leading to cancer cell treatment resistance.
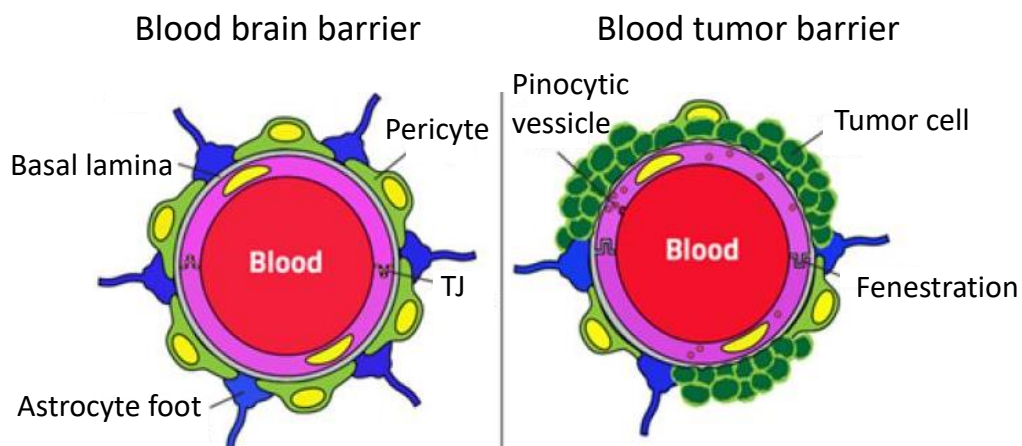
Figure 11. Schematic illustration of BBB and BTB. The BBB is made of three cell types: brain capillary endothelial cells, pericytes and astrocytes. Endothelial cells are tightly in contact to prevent paracellular transport. In case of tumor, the barrier undergoes structural changes: the major one concerns the loss of TJs to leave place to fenestrations making the barrier leaky [97].

1.4.1 Strategies for overcoming the impermeability of the BBB

To date, different approaches have been adopted to temporally disrupt or bypass the

BBB allowing oversized GNPs to enter the tumor.

Osmotic agents such as mannitol or bradykinin analogues are commonly used but result in widespread BBB disruption with the potential for deleterious consequences [98].

Convection-enhanced delivery can confine the lesion to a specific area placing several catheters directly within or around the tumor mass. A positive pressure is applied pushing the infusate into the extracellular fluid without inducing systemic toxicity [99]. Major pitfalls are related to safety concerns of open surgery and leakage of the infusate or reflux along the catheter tract [100].

Focused ultrasound (FUS) with lipid-encased gas-filled microbubbles increases permeability in a focal and reversible manner. When low frequency US waves are applied transcranially, the intravascular microbubbles oscillate in the acoustic field eliciting mechanical forces against the TJs of the endothelial cells that line the vessel wall [99]. FUS is safe and minimally invasive. The ensuing BBB disruption lasts at most for approximately 4 hours [98].

The disruption of the BBB requires that GNPs cross the BBB only in pre-treated areas, implying a priori knowledge of tumor invasion boundaries. This is counterintuitive since using diagnostic GNPs aims at achieving an ultra-sensitive detection of tumor edges at a macroscopic and microscopic level [62].

1.4.2 *In vitro* models of the BBB

Investigation of the ability of GNPs to cross the BBB and to reach the brain is essential to predict the performance of GNPs in a clinical context. Besides *in silico* and *in vivo* models, *in vitro* BBB models offer a valid tool to study different aspects of the BBB functions and interactions with potential drug candidates (such as uptake, mechanisms of transports and cytotoxicity). So far, transwell models or microfluidic devices are available. Availability of human primary brain material is limited and restricted to biopsy

or autopsy material, thus endothelial cell lines isolated from human or animal sources are used. Despite the endothelial cells are not the only component of the BBB, they are believed to mainly contribute to the formation of the barrier. They can be cultured alone or together with astrocytes or pericytes.

The human brain endothelial cell line, hCMEC/D3, has been used to establish a well characterized *in vitro* BBB model [101]. This cell line displays a stable and physiologically normal endothelial phenotype and keeps most of the structures and biochemical properties of brain endothelium *in vivo* [102]. It is worth mentioning that hCMEC/D3 cell line is characterized by low TEER levels ranging from 5 to 50 $\Omega*cm^2$ and reduced expression of ZO-1 and claudin-5 when cells are grown to confluence on transwell inserts [103]. Nevertheless, cell monolayer displays a highly restricted permeability to standard drugs in good correlation with *in vivo* permeability values from brain perfusion studies, confirming its suitability for transendothelial permeability analyses [102].

2. Motivation and aims of the thesis

Complete resection of contrast enhancing malignant brain tumors is achieved in less than 20% of cases. This is due to the difficulty to sharply delineate tumor margins and to identify infiltrative cancer cells specially in case of GBM [5], [18]. Therefore, improving intraoperative visualization of cancer cells is the motivation that gives rise to this project. SERS based imaging of GBM is promising to fulfil most of the requirements that current intraoperative guidance techniques have not met yet. A handheld Raman scanner, easy to use and able to interrogate the resection bed from any directions, is currently under clinical trial [5]. GNPs, if properly engineered, are able to cross the BBB and their detection in the NIR window counters the autofluorescence and increases the penetration depth [5], [10], [53]. In addition, SERS signal, when no fluorescent Raman reporters are used, is photo-stable ensuring a strong detection for the whole-time frame of the surgical operation [23]. However, successful visualization of GBM cells strongly depends on formulation of GNPs with increased sensitivity and binding affinity. To accomplish this task, surface functionalization of GNPs must consider a balance between inert and receptor specific active surface molecules. Indeed, we hypothesize that final performance of SERS tags, in terms of maximal colloidal stability and SERS signal, highest receptor binding affinity and lowest non-specific binding, depends on the proper mixture of Raman reporter, inert protective layer of PEG and antibody (Figure 1).

In order to establish a sensitive and selective intraoperative guidance technology for GBM detection, this thesis includes:

i) the preparation of SERS tags with several ratios of Raman reporter, inert protective PEG coating and antibody;

ii) the investigation of how these ratios affect colloidal stability, cellular binding specificity *in vitro* on cultured human GBM cell lines and Raman sensitivity;

iii) the determination of the optimum incubation time, concentration and surface chemistry to achieve the maximum SERS intensity while minimizing GNPs aggregation and non-specific binding;

iv) the modulation of SERS tags surface charge to reduce non-specific binding;

v) the establishment of an *in vitro* BBB model for evaluating the ability of SERS tags to cross the BBB before further *in vivo* investigation.
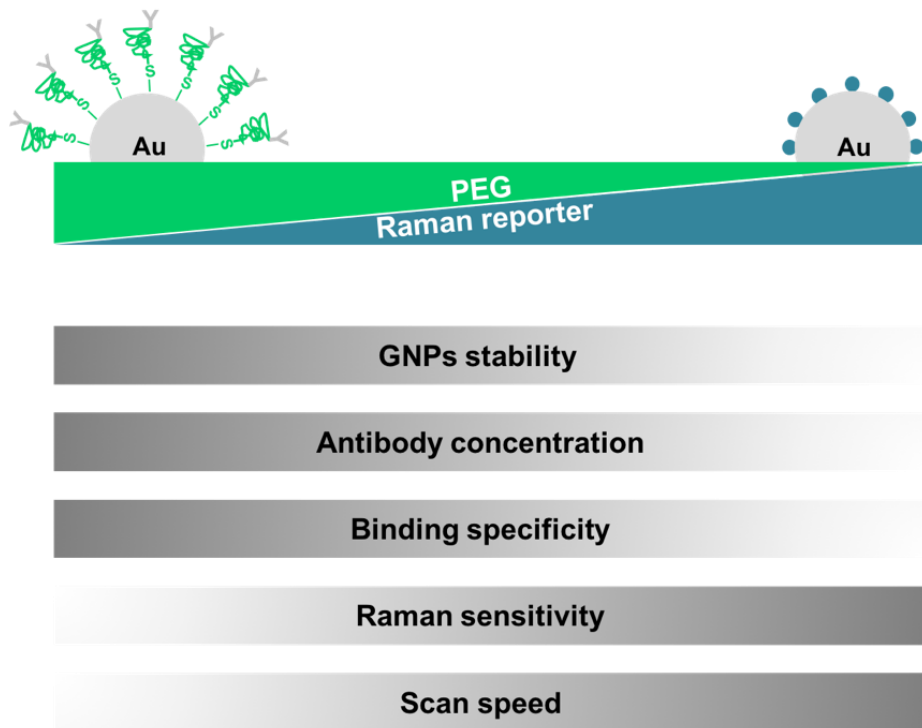
Figure 1. Influence of surface chemistry on SERS tags performance. The mixture of Raman reporter and PEG acts on gold colloidal stability, Raman signal intensity, cellular receptor binding affinity, non-specific binding and scan speed. Full PEG surface coverage is supposed to elicit a higher binding specificity and GNPs stability and to allow the conjugation of higher antibody concentrations. Conversely, full Raman reporter surface coverage is supposed to boost the Raman sensitivity reducing the acquisition time.

3. Results

3.1 SERS tags preparation and characterization

Tags for SERS based imaging of GBM were developed by coating 60 nm GNPs (Figure 1A) with 1,4-Benzendithiol (1,4-BDT) (Figure 1B) used as Raman reporter (Figure 1C). Unconjugated GNPs were then produced by sequentially backfilling remaining free spaces with first carboxy-PEG-thiol (cPEG) followed by methoxy-PEG-thiol (mPEG) to improve binding specificity and biocompatibility (Figure 1D). To target specifically GNPs towards tumor cells, antibodies against EGFR were covalently conjugated producing anti-EGFR GNPs (Figure 1E).
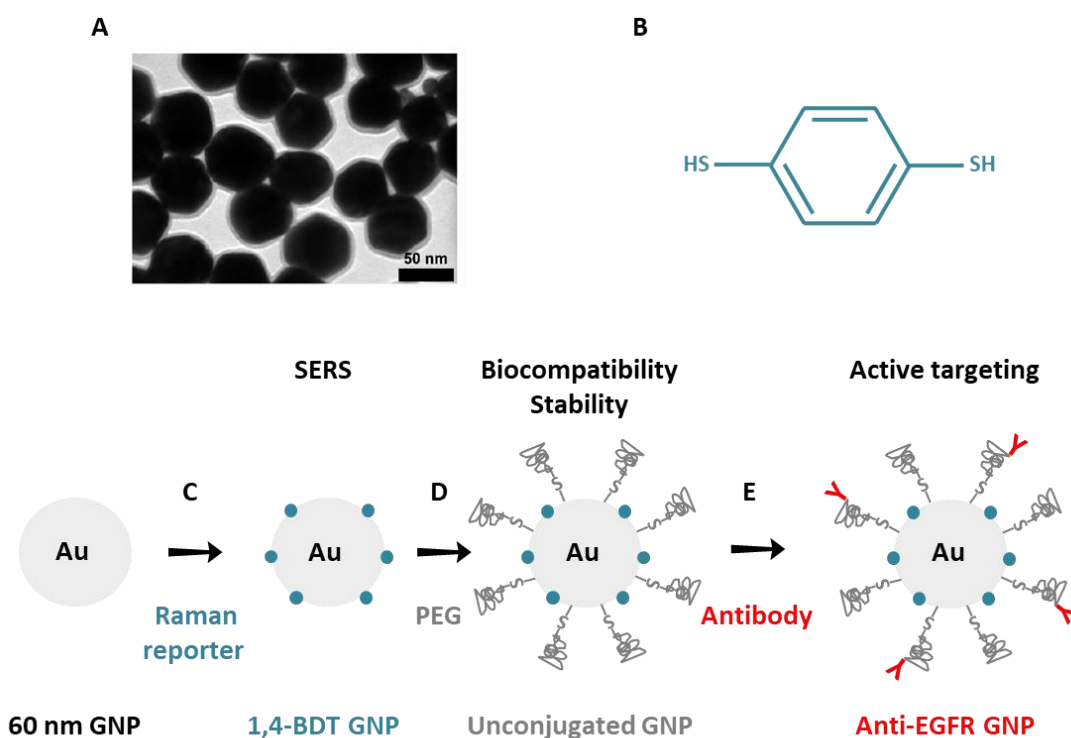
Figure 1. Design of tags for SERS based imaging of GBM. A) Transmission electron microscopy picture of 60 nm GNPs in citrate buffer. Image taken with EM 900 transmission electron microscope (Zeiss), acceleration voltage 50 kV. Scale bar 50 nm. B) Chemical structure of 1,4-BDT used as Raman reporter. C) The Raman reporter, 1,4-BDT, is immobilized on gold surface for maximal SERS sensitivity (1,4-BDT GNP). D) PEG is used to create an inert shell for improved stability and to prevent non-specific binding (unconjugated GNP). E) Anti-EGFR antibodies are then conjugated for active targeting (anti-EGFR GNP).

Several surface coverage percentages of Raman reporter and PEG were tested. Considering a perpendicular orientation of Raman reporter with a footprint of approx. 0.09 nm^2, and a mushroom configuration of PEG with a footprint of 0.35 nm^2, the theoretical number of molecules required for a 100% surface coverage of the gold area of 11'304 nm^2 was calculated for each ratio (Table 1). From now on, each chemistry ratio is reported in function of the Raman reporter surface coverage used.

Raman reporter (μM)	Raman reporter surface coverage (%)	Raman reporter molecules	cPEG molecules	mPEG molecules	Total PEG surface coverage (%)
4	100	128'000	0	0	0
2	50	64'000	5'000	11'000	50
1	25	32'000	5'000	19'000	75
0.4	10	12'800	5'000	24'000	90
0	0	0	5'000	27'000	100

Table 1. Theoretical calculation of molecules required to form a monolayer. Concentrations of Raman reporter and corresponding surface coverages or number of molecules are reported. Both cPEG and mPEG were used, thus the number of the respective molecules and the total PEG surface coverage are listed.

3.1.1 Raman reporter coupling for SERS
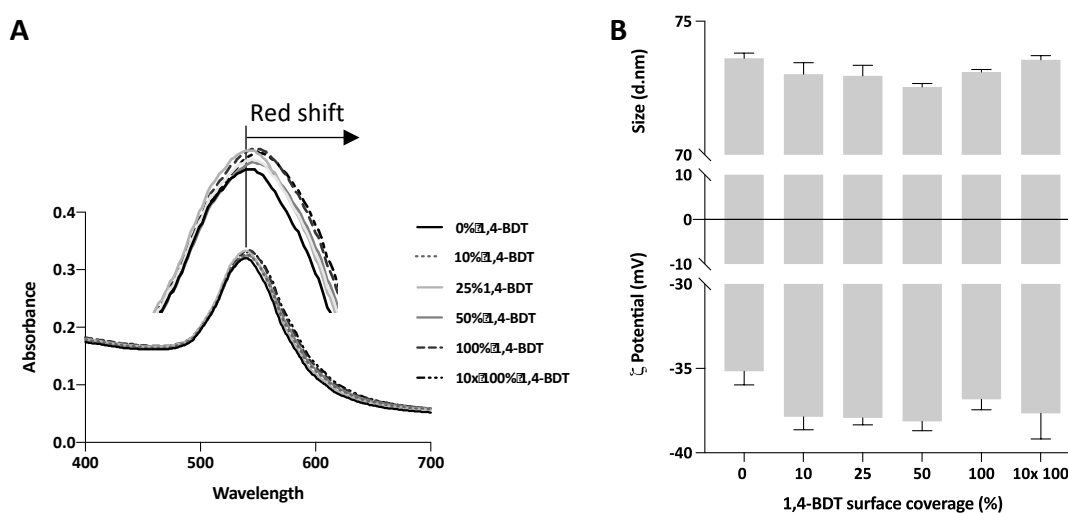
Figure 2. Optical and physical properties of 1,4-BDT GNPs. A) Absorption peak of GNPs coated with increasing 1,4-BDT surface coverages. UV-Vis extinction spectra acquired with Sinergy H1 microplate reader (BioTek Instrument, GmbH). B) Hydrodynamic size and negative zeta potential correlated to increasing 1,4-BDT surface coverages. Analysis done with Zetasizer ZS dynamic light scattering instrument (Malvern Panalytical Ltd, UK), T 25°C, pH 7, n=3, mean ± SD.

SERS tags were produced by coating GNPs with theoretically increasing surface coverages of 1,4-BDT, from 0 to 100%. 10-fold excess (10x 100%) Raman reporter was even tested to ensure the complete surface saturation. UV-Vis spectra were recorded as first and fast control of surface modification. LSPR, centered at 540 nm for bare GNPs, experienced a progressive red shift up to 5 nm with 10-fold excess Raman reporter, as a result of the increased local refractive index at the GNPs surface (Figure 2A). However, both the hydrodynamic size and the zeta potential stayed unchanged even at the highest Raman reporter surface coverage (Figure 2B).

3.1.1.1 SERS signal enhancement

The amplification of the fingerprint spectrum as soon as the Raman reporter comes in contact with the GNPs surface can be observed by comparing the spectra of 1,4-BDT free or immobilized on gold colloidal suspension (Figure 3). Both spectra exhibited several peaks including two strong bands at 1'068 cm^{-1} and 1'556 cm^{-1}, corresponding to ring breathing and ring stretching vibrations, respectively, while the Raman mode at 2'556 cm^{-1} was visible only in the spectrum of free 1,4-BDT.
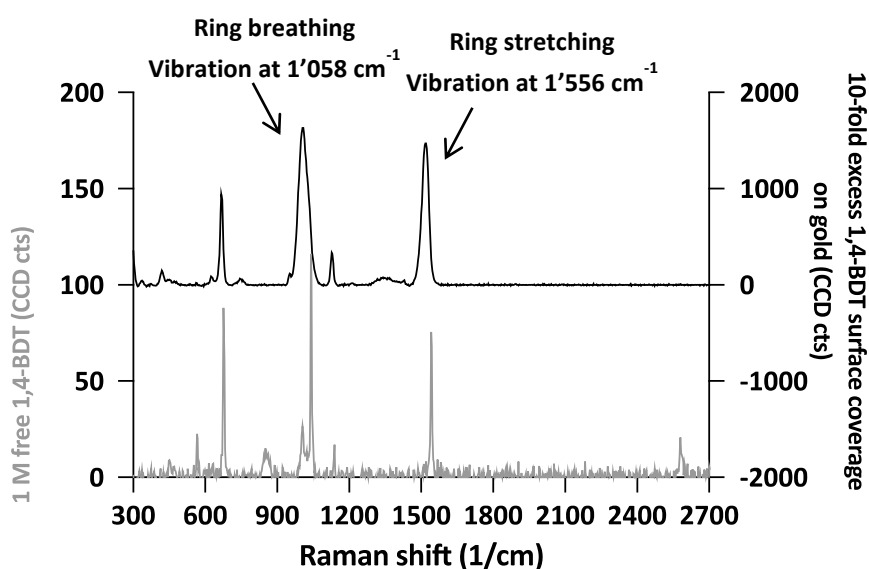
Figure 3. SERS enhancement mechanism. Raman spectrum of 1 M free 1,4-BDT used as reference solution (gray curve) and SERS spectrum of 10-fold excess 1,4-BDT absorbed on gold surface (black curve). Arrows indicate the two most characteristic bands of 1,4-BDT at 1'058 cm^{-1} and 1'556 cm^{-1}, corresponding to ring breathing and ring stretching vibrations, respectively. Measurements done with confocal Raman microscope (WITec GmbH, Germany), λ_{ex} 785 nm, laser power 60 mW, integration time 0.5 s, accumulation 10, 100x objective.

3.1.1.2 Influence of Raman reporter surface coverage on SERS intensity

SERS spectra were collected to determine how intensity changes in relation to increasing Raman reporter surface coverages and to identify the one giving the strongest signal for a clear detection of GNPs during imaging. Equal concentrations of GNPs were used to get rid of any variation due to different number of particles. Experimental measurements showed that the enhancement of SERS signal followed the actual amount of 1,4-BDT for surface coverages up to 100% and reached the saturation at 10-fold excess despite amount 1,4-BDT was approx. 4-fold higher (8-fold higher amount of sulfur per Au) as quantified by inductively coupled plasma mass spectrometry (ICP-MS) analysis (Figure 4).
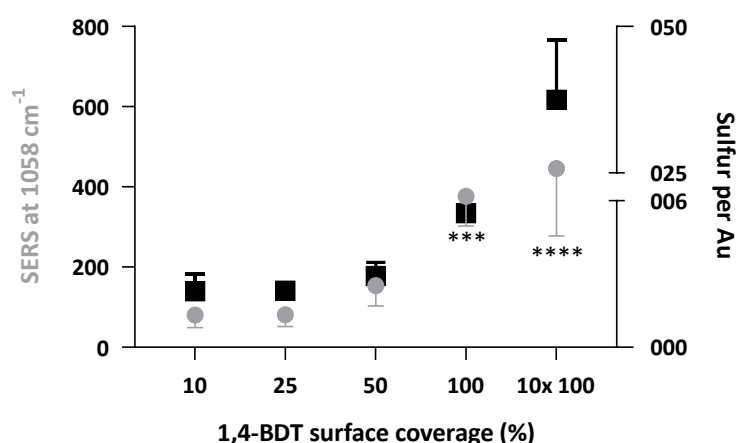
Figure 4. Influence of Raman reporter surface coverage on SERS intensity. Intensity of SERS signal at 1'058 cm^{-1} relative to increasing 1,4-BDT surface coverages. Raman measurements done with confocal Raman microscope (WITec GmbH, Germany), λ_{ex} 785 nm, laser power 50 mW, integration time 0.5 s, 10 accumulations, 50x objective, ***$p \leq 0.001$, ****$p \leq 0.0001$ vs 10% 1,4-BDT surface coverage, n=3, mean ± SD. Amount of sulfur per Au was quantified with 8800 ICP-qqq-MS instrument (Agilent technologies), n=2, mean ± SD.

3.1.2 PEGylation for improved stability and biocompatibility

PEG is considered the gold-standard cloaking agent to increase stability and biocompatibility of nanoparticles. Furthermore, it can act as linker for antibody conjugation. Therefore, GNPs were functionalized with a mixture of bifunctional linkers, cPEG and mPEG. SERS spectrum of PEGylated GNPs ensured that PEG coating did not displace the Raman reporter and did not interfere with its detection (data not shown). Particles without 1,4-BDT reached dimensions up to 90 nm, while hydrodynamic size

gradually decreased with 10 and 25% Raman reporter surface coverages and stayed

constant at 75 nm when 50% and higher percentages of Raman reporter were applied

(Figure 5A). Zeta potential measurements and ICP-MS analysis (Figure 5B) showed

higher surface charge values and amounts of sulfur per Au, respectively, after

immobilization of mPEG independently on the surface coverage of 1,4-BDT applied in

the previous functionalization step.
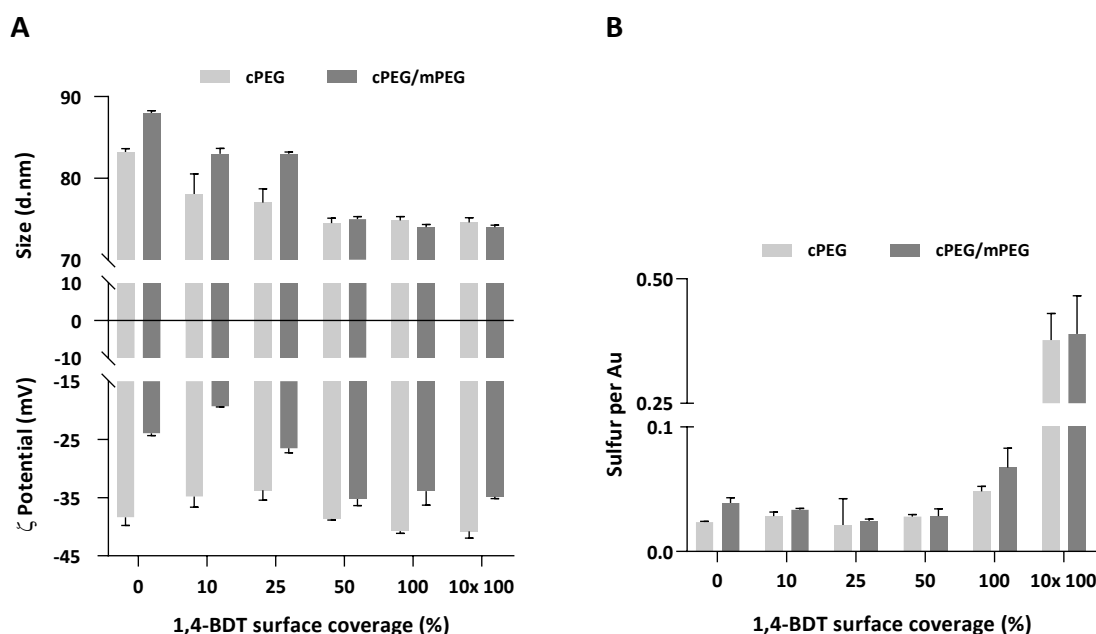
Figure 5. Chemico-physical properties of unconjugated GNPs. A) Hydrodynamic size and zeta potential measurements depending on increasing 1,4-BDT surface coverages. Analysis done with Zetasizer ZS dynamic light scattering instrument (Malvern Panalytical Ltd, UK), T 25°C, pH 7, n=3, mean ± SD. B) Amount of sulfur per Au of immobilized PEG quantified with 8800 ICP-qqq-MS instrument (Agilent technologies), n=2, mean ± SD.

3.1.3 Anti-EGFR mediated active targeting

To promote active targeting of tumor cells, as the last step of surface functionalization,

increasing surface coverages of anti-EGFR antibody, from 3 to 30%, were covalently

conjugated to the carboxy terminal groups of cPEG. To differentiate active targeting

from passive accumulation, unconjugated GNPs (GNPs with no antibodies) were used

as negative control. Despite antibody immobilization was not always accompanied by a

clear increase in size or a change in surface charge (Figure 6A), successful conjugation

was corroborated by detecting anti-EGFR antibodies with immunofluorescence analysis

(Figure 6B). Furthermore, quantification of the number of antibodies per GNP, modified

with 10% Raman reporter surface coverage, relieved that the highest conjugation efficiency of 40% was achieved with 3% anti-EGFR antibody surface coverage.
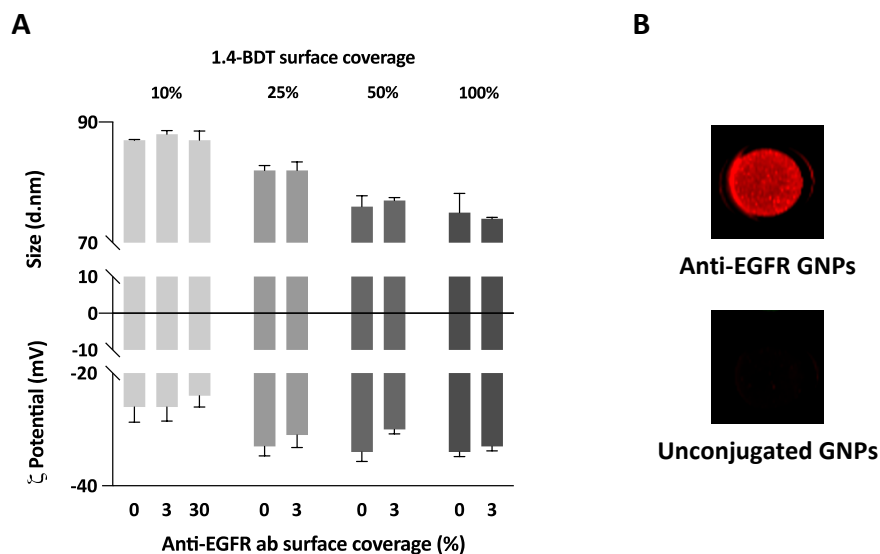
Figure 6. Anti-EGFR antibody conjugation to PEGylated GNPs. A) Hydrodynamic size and zeta potential depending on increasing anti-EGFR antibody surface coverages. Analysis done with Zetasizer ZS dynamic light scattering instrument (Malvern Panalytical Ltd, UK), T 25°C, pH 7, n=3, mean ± SD. B) Immunofluorescence detection of anti-EGFR antibodies on GNPs. Anti-EGFR and unconjugated GNPs encased by 100% 1,4-BDT were incubated with fluorescent secondary antibody and imaging was performed with Odyssey infrared imaging system (Li-cor, Biosciences).

Conversely, it was reduced to 16.5 and 5% when 7.5 and 30% anti-EGFR antibody surface coverages were used, respectively (Table 2). Therefore, 3% anti-EGFR antibody surface coverage was chosen to produce tumor cell specific GNPs.

Raman reporter surface coverage (%)	Anti-EGFR antibody surface coverage (%)	Theoretical anti-EGFR antibodies per GNP	Empirical anti-EGFR antibodies per GNP	Conjugation efficiency (%)
	3	164	64±4	40
10	7.5	410	67±10	16.5
	30	1'640	84±9	5

Table 2. Anti-EGFR antibody immobilization on GNPs. GNPs with 10% 1,4-BDT were conjugated to increasing surface coverages of anti-EGFR antibody. Theoretical and effective number of antibodies per GNP and relative conjugation efficiency are reported.

3.1.4 Anti-EGFR GNPs bio-functionality and stability in cell culture medium

Functionality of anti-EGFR GNPs is an essential requirement to achieve active targeting. Therefore, it was evaluated first through immune dot blot. Human recombinant EGFR

was spotted on a nitrocellulose membrane and probed with anti-EGFR or unconjugated GNPs. A pink spot was visualized only upon binding of anti-EGFR GNPs, confirming antibody bio-activity and binding specificity (Figure 7A). Results were confirmed by western blot (Figure 7B).

A **B**

Anti-EGFR GNPs   Unconjugated GNPs   M   Anti-EGFR GNPs Unconjugated GNPs
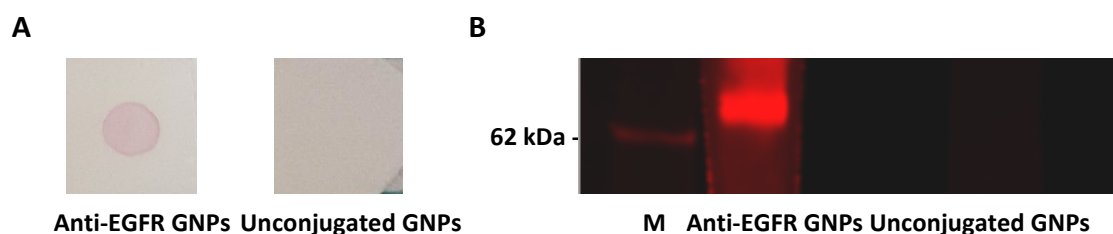
Figure 7. Bio-functionality of anti-EGFR GNPs. Human recombinant EGFR was spotted (A) on a nitrocellulose membrane or (B) run through a gel, transferred to a PDVF membrane and imaged with Odyssey infrared imaging system (Li-cor, Biosciences). Bound GNPs were evaluated through the presence of a bright pink spot or a fluorescence band at the expected EGFR molecular weight of 70 kDa.

Long term stability of GNPs introduced to biological environment is critical since it is directly linked to the cellular response outcomes. To test their stability, anti-EGFR and unconjugated GNPs were mixed with Dulbecco's Modified Eagle's Medium - high glucose (DMEM) supplemented with 10% fetal calf serum (FCS) in a ratio of 1:2 and kept at 37°C. Absorbance was measured at 450 nm at multiple time points over 24 h (Figure 8). Slightly increase was observed during the first 4 h, likely due to evaporation, but stayed constant over the remaining 20 h vouching the stability of GNPs in biological medium.
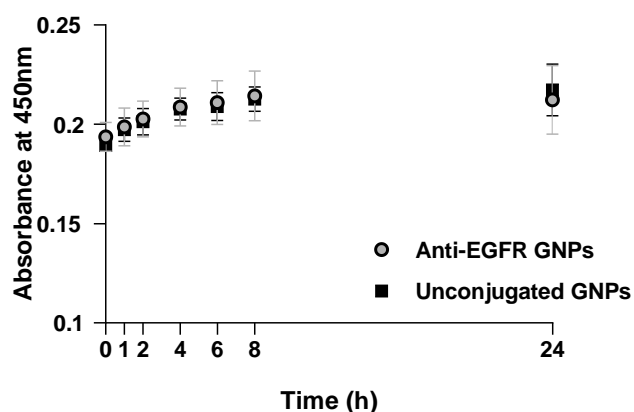
Figure 8. Stability of anti-EGFR and unconjugated GNPs in cell culture medium. GNPs were incubated in DMEM + 10% FCS (1:2) and mixed at 37°C at 450 rpm. Absorbance was measured at 450 nm at multiple time points over 24 h, n=3, mean ± SD. Data obtained with Sinergy H1 microplate reader (BioTek Instrument, GmbH).

3.2 *In vitro* cancer cell targeting by anti-EGFR GNPs

3.2.1 Cellular EGFR expression

SERS tag specificity was evaluated on EGFR-positive GBM cell lines, LN229wtEGFR, BS153 and U87MG. Decreasing levels of EGFR expression were confirmed by immunofluorescent staining (Figure 9A) and western blot (Figure 9B).
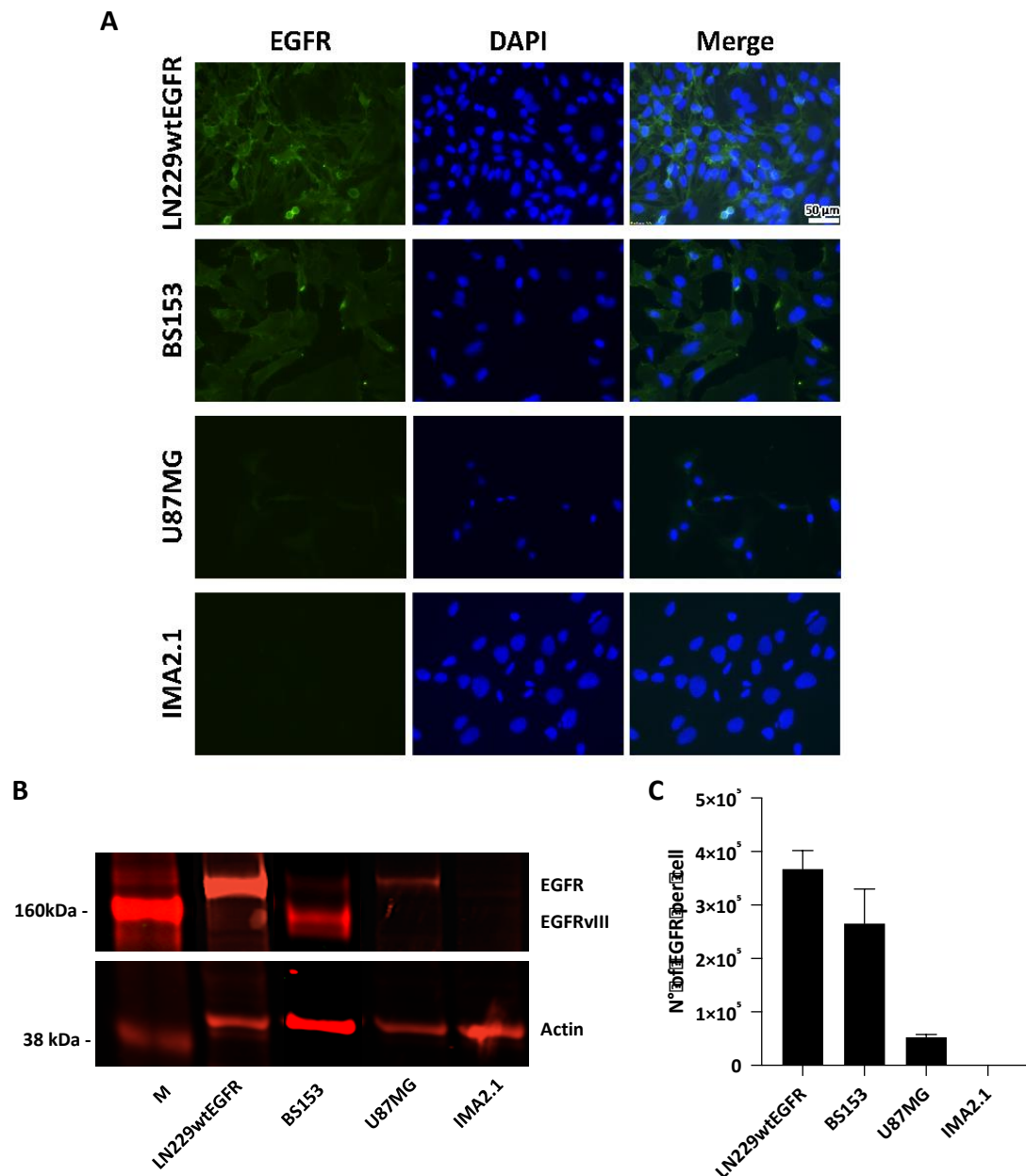
Figure 9. Different expression levels of the EGFR protein in GBM cell lines. A) Immunofluorescent staining of EGFR-positive GBM cells (LN229wtEGFR, BS153 and U87MG) and immortalized glial cell line IMA2.1 used as negative control. Nuclei stained in blue and EGFR in green. Pictures taken with DMRE microscope (Leica Microsystem). Scale bar 50 μm. B) Western blot: EGFR detected at 170 kDa and actin at 42 kDa, EGFRvIII detected at 145 kDa in BS153. C) Number of receptors per cell quantified by qFACS, n=3, mean ± SD.

In addition to EGFR, BS153 also expressed EGFRvIII as ascertained by the presence of a second lower band detected at 145 kDa. The number of EGFR was found to be 36 x 10^4 25 x 10^4 and 5 x 10^4 per cell, respectively, as quantified by quantitative fluorescence-activated cell sorting (qFACS) (Figure 9C). In contrast, immortalized murine astrocytes IMA2.1 were used as EGFR-negative cell line.

3.2.2 Cellular viability response to GNPs

Whether GNPs produce or not adverse effects is still contradictory. Therefore, cellular viability in the presence of GNPs was investigated by incubating LN229wtEGFR with 4 x 10^5 anti-EGFR or unconjugated GNPs per cell. This amount was chosen to ensure complete saturation of EGFR at the cell surface. After 24 h of exposure, cells did not show decreased viability compared to the untreated ones confirming the lack of any noticeable toxicity of GNPs (Figure 10). Consistently, 4 x 10^5 or lower number of GNPs per cell were used in the following experiments (from now on expressed as μg/ml).
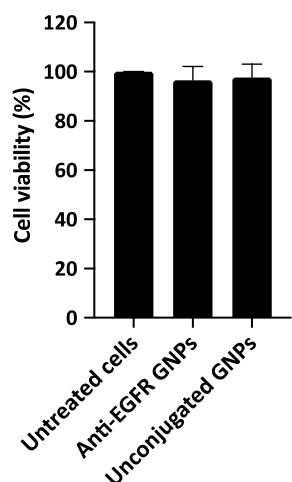
Figure 10. Absence of GNPs cytotoxicity. The release of formazan was determined after 24 h of incubation of LN229wtEGFR cells with 4 x 10^5 anti-EGFR or unconjugated GNPs/cell. Absorbance was read at 450 nm using FlexStation 3 microplate reader (Molecular Device, LCC). Values expressed as percentage of negative control (untreated cells), n=3, mean ± SD.

3.2.3 SERS based imaging of GBM cells

For SERS based imaging of anti-EGFR GNP-marked tumor cells, GNPs with 100% Raman reporter surface coverage and coupled with 3% anti-EGFR antibodies were used, unless otherwise specified, since they provided the strongest Raman signal for a fast and sharp detection of tumor cells. From now on, Raman maps were generated by plotting the SERS signal of Raman reporter bands at 1'058 cm^{-1} and 1'556 cm^{-1}. The brighter the color, the higher the number of GNPs attached to the cells. Measurements were done

with confocal Raman microscope (Witec, GmbH, Germany) according to the following setting: λ_{ex} 785 nm, laser power 25 mW, integration time 0.05 sec, 50x objective. Raman pictures are reported with the same scale in order to make Raman intensity comparable.

3.2.3.1 Time-dependent binding of anti-EGFR GNPs on EGFR-positive GBM cells

To determine how cellular accumulation of GNPs varies with time, LN229wtEGFR and IMA2.1 cells were incubated with 15 µg/ml of anti-EGFR or unconjugated GNPs for 30 min, 1, 4, 8 and 24 h. The longer the incubation, the higher the amount of anti-EGFR GNPs taken up by LN229wtEGFR as revealed by fluorescence and Raman analysis (Figure 11A).
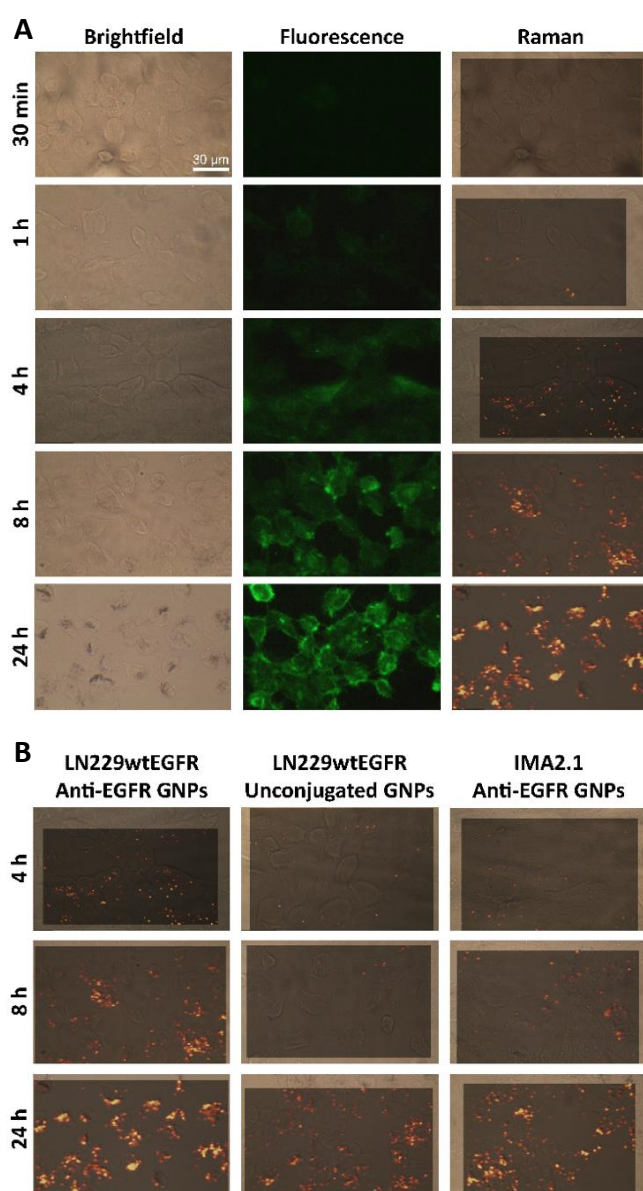
Figure 11. Time-dependent binding of anti-EGFR GNPs on EGFR-positive GBM cells.
A) Time-dependent uptake of anti-EGFR GNPs incubated with LN229wtEGFR cells for 30 min, 1, 4, 8 and 24 h and detected by fluorescent staining and Raman.
B) Time-dependent specificity of the binding of anti-EGFR or unconjugated GNPs incubated with LN229wtEGFR or IMA2.1 cells for 4, 8 and 24 h. Scale bar 30 µm.

However, incubation times longer than 4 h led to non-specific uptake of anti-EGFR GNPs by IMA2.1 cells and unconjugated GNPs by LN229wtEGFR cells (Figure 11B). Consistently, incubation time was fixed at 4 h for the subsequent experiments.

3.2.3.2 Time-dependent uptake and localization of anti-EGFR GNPs on EGFR-positive GBM cells

Confocal fluorescence pictures of LN229wtEGFR cells incubated with anti-EGFR GNPs were captured to investigate their cellular uptake over 24 h. Co-localization staining was performed to track the intracellular fate of endocytosed GNPs.
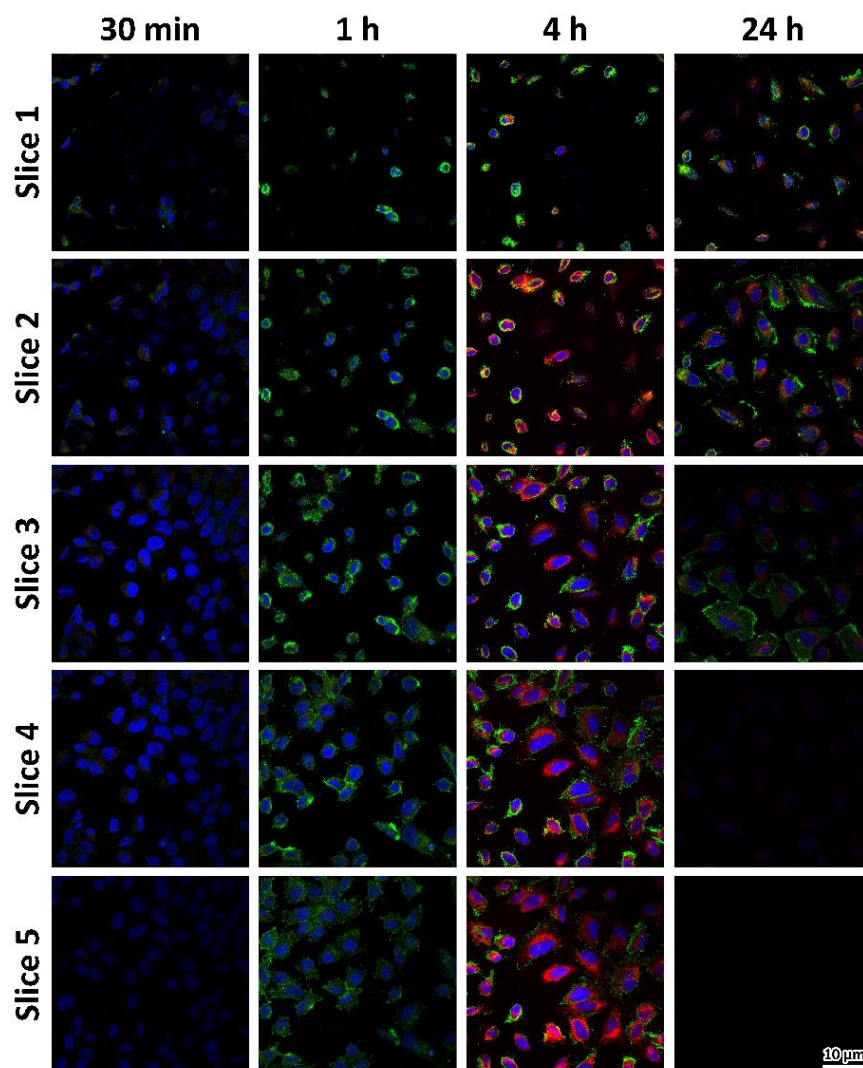
Figure 12. Time-dependent uptake and localization of anti-EGFR GNPs on EGFR-positive GBM cells. Anti-EGFR GNPs were incubated with LN229wtEGFR cells to monitor their cellular distribution after 30 min, 1, 4 and 24 h. Anti-EGFR antibodies on anti-EGFR GNPs were detected in green, lysosomes in red and nuclei in blue. Pictures were taken with laser confocal fluorescence microscope FV1000D (Olympus) and acquisition setting was changed at 30 min and 1 h to allow GNPs visualization. Scale bar 10 μm.

As shown in figure 12, weak uptake already started after 30 min of incubation and became stronger at 1 h. At 4 h, upon endocytosis, anti-EGFR GNPs moved to the lysosomes as proved by perinuclear co-localization (yellow spot) of anti-EGFR GNPs and lysosomes. Despite fluorescence signal was detected even in the cytoplasm, anti-EGFR GNPs were found to be mainly distributed at the cellular surface as expected since EGFR protein is located at the cellular membrane. This was more evident after 24 h of incubation.

3.2.3.3 Influence of cellular EGFR expression level on anti-EGFR GNPs binding

To assess the influence of different expression of EGFR at the cell membrane on anti-EGFR GNPs binding, LN229wtEGFR, BS153, U87MG and IMA2.1 cells were incubated with decreasing concentrations of anti-EGFR GNPs (70, 22, 5 µg/ml). Raman detection of anti-EGFR GNPs showed that signal increased in a concentration-dependent manner (Figure 13). Gathered GNPs were not sufficient at 5 µg/ml. Conversely, at 70 µg/ml amount of anti-EGFR GNPs was as much adequate as necessary for strong signal and distribution was uniform allowing a clear delineation of the cell shape.
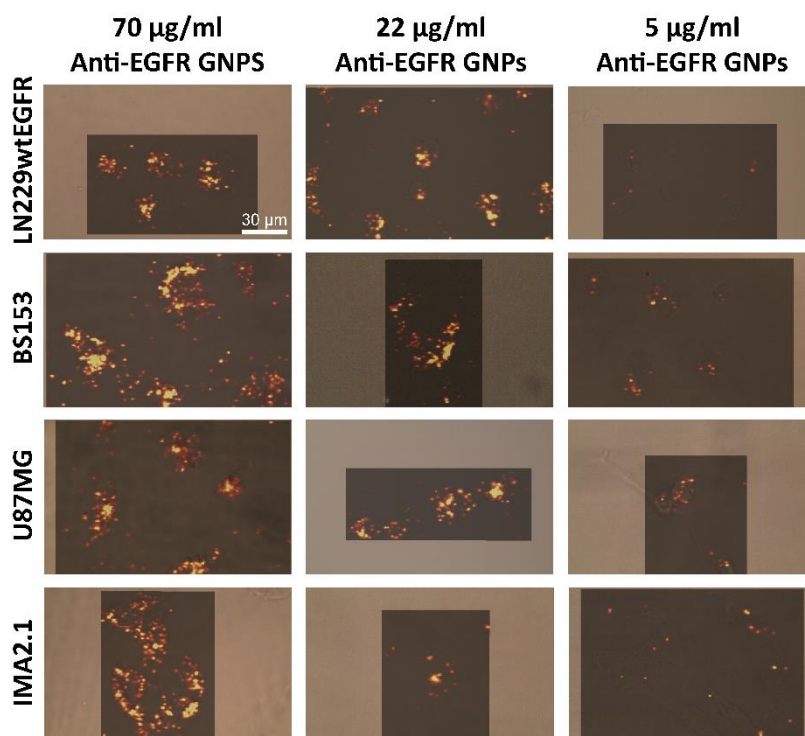
Figure 13. Effect of different EGFR expression level on anti-EGFR GNPs binding. LN229wtEGFR, BS153, U87MG and IMA2.1 cells were incubated with decreasing concentrations of anti-EGFR GNPs for 4 h and detected by Raman. Scale bar 30 µm.

However, absorption of anti-EGFR GNPs on IMA2.1 was too high. At 22 μg/ml, discrimination between EGFR-positive GBM and EGFR-negative cell lines was possible, and a comparable high Raman signal intensity was detected among the different GBM cell lines independent on the expression level of EGFR. Therefore, the concentration of 22 μg/ml anti-EGFR GNPs was further used.

3.2.4 Drawbacks of Raman reporter monolayer surface coverage

After conjugation of anti-EGFR antibodies, reproducibility of GNPs with 100% Raman reporter surface coverage appeared to be problematic due to frequent and random aggregation. This was revealed by significant changes in the absorption spectrum (Figure 14A), size (Figure 14B) and color of gold suspension from pink to violet (Figure 14C). In the worst-case aggregation followed by precipitation was noticed (Figure 14D).
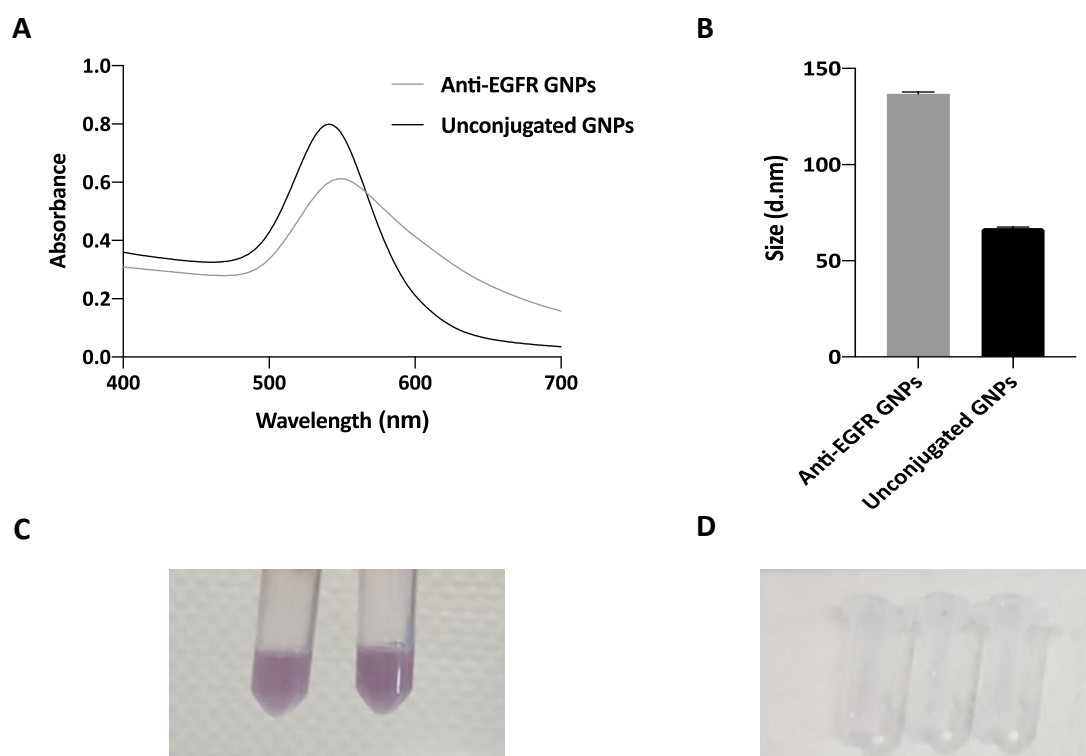
Figure 14. Aggregation of GNPs with 100% Raman reporter surface coverage after anti-EGFR antibodies conjugation. A) Red shift and broadening of the absorption spectrum. UV-Vis extinction spectra acquired with Sinergy H1 microplate reader (BioTek Instrument, GmbH). B) Doubling of the size. Analysis done with Zetasizer ZS dynamic light scattering instrument (Malvern Panalytical Ltd, UK), T 25°C, pH 7, n=3, mean ± SD. C) Change of the color suspension from pink to violet. D) In case of precipitation suspension color turned to transparent.
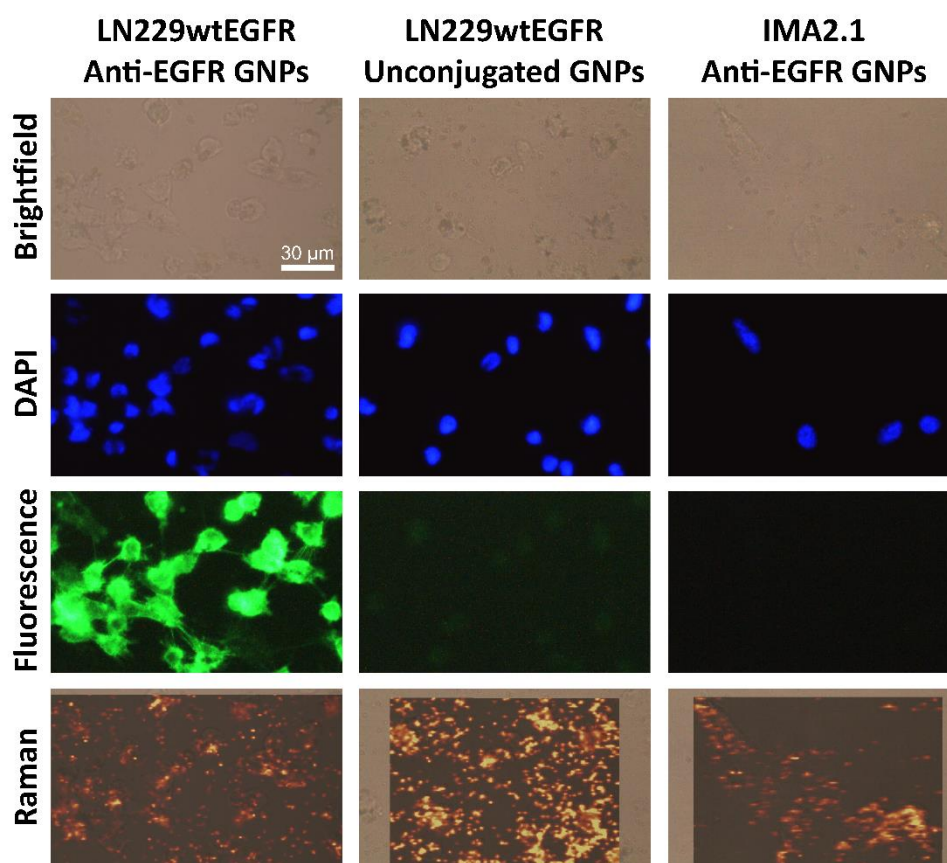
Figure 15. Impaired cell discrimination due to sedimentation and non-specific binding of GNPs. Anti-EGFR or unconjugated GNPs were incubated with LN229wtEGFR or IMA2.1 cells and detected by fluorescent staining and Raman. Scale bar 30 µm.

In addition, GNPs sedimentation and non-specific binding were two main concerns to face (Figure 15). In attempting to overcome these inconveniences, two new experimental setups were tested and concentration of GNPs was decreased. First, LN229wtEGFR or IMA2.1 cells were incubated in suspension with 5 µg/ml of anti-EGFR GNPs at 37°C (Figure 16A). Incubation time was only 1 h since this setup was performed out of the incubator to allow the shaking at 400 rpm in the thermomixer.

Second, BS153 or IMA2.1 cells were incubated with 10 µg/ml of anti-EGFR GNPs for 4 h, but the plate was kept under agitation throughout the duration of the incubation (Figure 16B). Raman analysis showed that sedimentation was completely solved with both settings, but non-specific binding persisted even at lower concentrations of anti-EGFR or unconjugated GNPs (data not shown). Because of similar outcomes and to avoid cellular stress due to the depletion of CO_2 when cells are kept outside of the incubator, the first setup was abandoned, while agitation was kept for the following experiments.
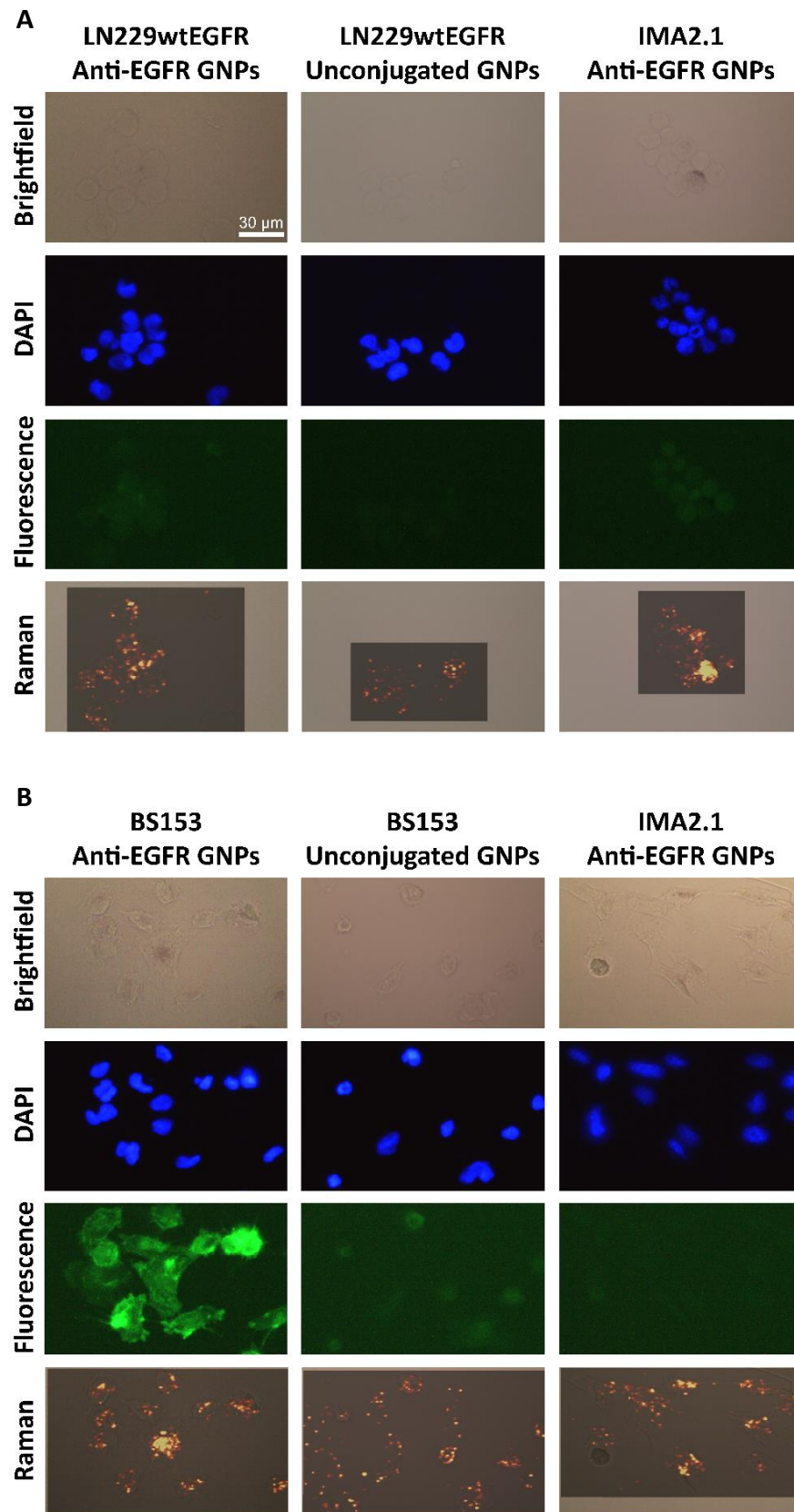
Figure 16. Persistence of non-specific binding. Anti-EGFR or unconjugated GNPs were incubated with GBM (LN229wtEGFR or BS153) or IMA2.1 cells (A) in suspension for 1 h or (B) under agitation for 4 h and detected by fluorescent staining and Raman. Scale bar 30 μm.

3.2.4.1 Modulation of surface charge of GNPs for minimizing non-specific binding
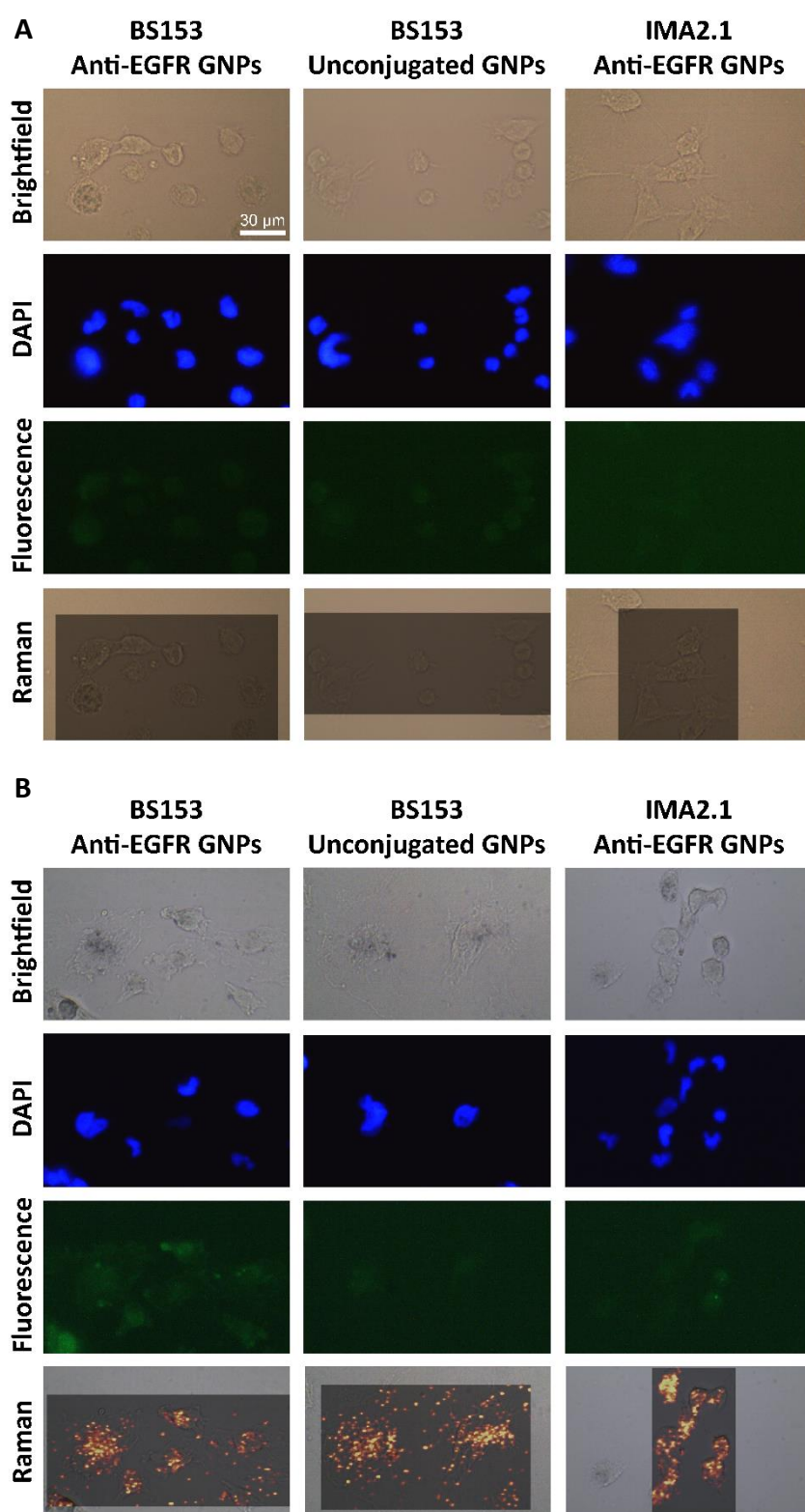
Figure 17. Influence of surface charge on GNPs binding. At 2 h from antibody incubation, anti-EGFR and unconjugated GNPs were further modified with (A) ethanolamine or (B) aPEG. Anti-EGFR or unconjugated GNPs were incubated with BS153 or IMA2.1 cells under agitation and detected by fluorescent staining and Raman. Scale bar 30 μm.

Surface charge is known to be one of the parameters influencing GNPs binding. Indeed, GNPs contain a lot of carboxy terminal groups, which are negatively charged at pH 7. Blocking agents replace the carboxy groups with hydroxy or methoxy groups making GNPs less negatively charged. In order to reduce non-specific binding, surface charge was manipulated by adding an excess of blocking agents such as ethanolamine or amino-PEG-methoxy (aPEG) after either 2 h or overnight incubation of GNPs with anti-EGFR antibodies. The adjunct of 1% ethanolamine after 2 h caused the depletion of Raman and fluorescent signal even on BS153 incubated with 10 μg/ml of anti-EGFR GNPs (Figure 17A). Conversely, the addition of 1% ethanolamine after overnight incubation or excess of aPEG after 30 min, 2 h or overnight incubation did not interfere with antibody conjugation as confirmed by the restored, even though weak, fluorescent signal on BS153 cells (Figure 17B). However, it did not improve the non-specific binding of anti-EGFR GNPs on IMA2.1 or the passive absorption of unconjugated GNPs on BS153 cells.

### 3.2.4.2 Effect of PEG coating on non-specific binding and SERS sensitivity

To prove that the ratio of 1,4-BDT and PEG affects the binding specificity, SERS signal was measured after incubation of BS153, U87MG and IMA2.1 cells with 10 μg/ml of anti-EGFR GNPs carrying increasing amounts of Raman reporter. As negative control, BS153 cells were incubated with same amount of unconjugated GNPs (Figure 18A).

Under these conditions, the strongest SERS signal was acquired on cells exposed to GNPs with 100% Raman reporter surface coverage as confirmed by its quantification, but it co-occurred with non-specific binding of GNPs on the two negative controls resulting in false positive results. Increased PEG surface coverage, as a consequence of lower surface coverage of 1,4-BDT, minimized progressively the non-specific binding in IMA2.1 incubated with anti-EGFR GNPs (80% decrease and no signal with 50% and lower surface coverages of 1,4-BDT, respectively) and in BS153 incubated with unconjugated GNPs (unchanged, 93% decrease and no signal with 50, 25 and 10% surface coverages of 1,4-BDT, respectively). Moreover, the lower the Raman reporter surface coverage, the smaller the SERS signal intensity in BS153 (unchanged, 98 and 99% decrease with 50, 25 and 10% surface coverages of 1,4-BDT, respectively) and in U87MG (40, 96 and

98% decrease with 50, 25 and 10% surface coverages of 1,4-BDT, respectively) incubated with anti-EGFR GNPs. To note that, in BS153 and in U87MG exposed to anti-EGFR GNPs encased by 10 and 25% surface coverages of 1,4-BDT, the detected signal was attributable to isolated particles and its intensity was not considered strong enough for a clear discrimination between EGFR-positive GBM and EGFR-negative cells.
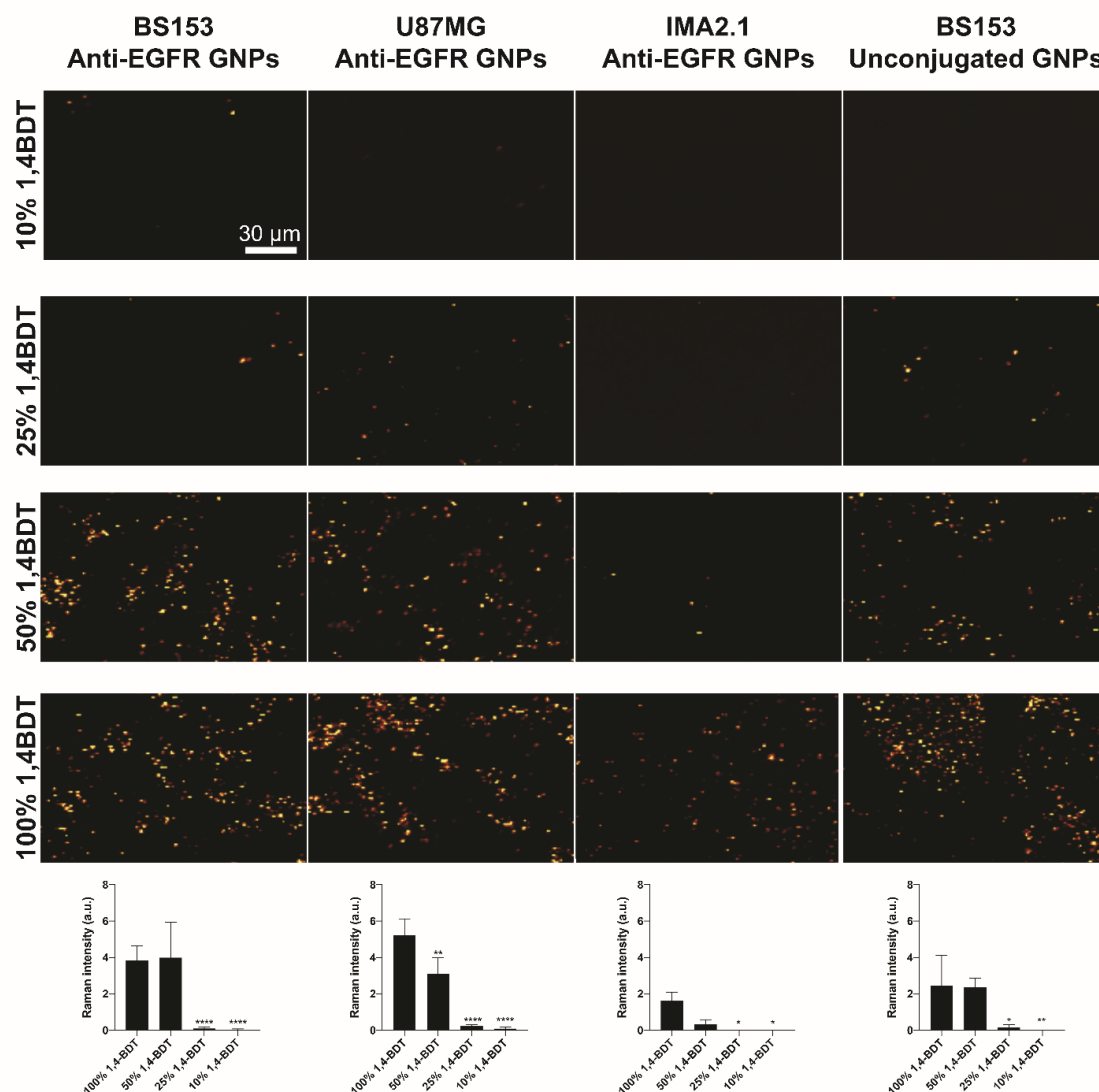
Figure 18. Increased PEG surface coverage minimized non-specific binding. EGFR-positive GBM (BS153 and U87MG) and EGFR-negative (IMA2.1) cells were incubated with anti-EGFR or unconjugated GNPs functionalized with increasing surface coverages of 1,4-BDT and detected by Raman. Quantification of relative SERS signal is reported below. Pictures of three random areas for each specimen were transformed in 16-bit images and signal was quantified with Image J software. *p≤0.05, **p≤0.01, ****p≤0.0001 vs 100% 1,4-BDT, n=3, mean ± SD. Scale bar 30 μm.

GNPs with 10% surface coverage of 1,4-BDT coupled to 84 anti-EGFR antibodies (as quantified in section 3.1.3) were used to improve binding ability and to boost the SERS signal accordingly. However, Raman detection did not raise (Figure 19) not even after

increasing the concentration of GNPs or the laser power (data not shown). Decreased Raman signal was not ascribed to the absence of the GNPs on the cells whose presence was confirmed by immunofluorescent staining and dark field analysis. Indeed, due to the strong SPR light scattering, GNPs were visualized as bright points further confirming the binding specificity due to higher PEG surface coverage. It was not even ascribed to the displacement of the Raman marker from the GNPs surface as proven by the detection of its fingerprint spectrum in the supernatant collected after incubation with cells (data not shown).
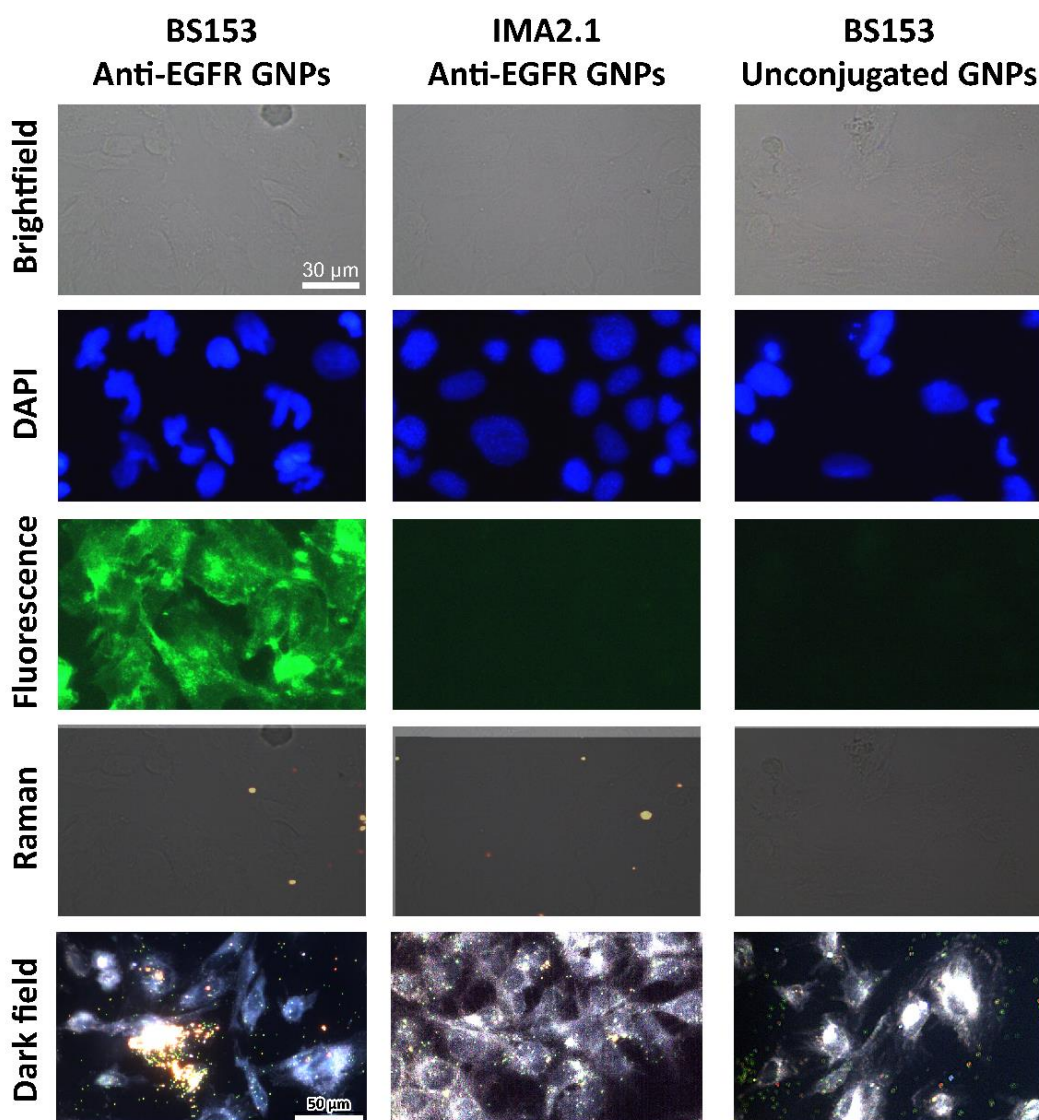
Figure 19. Reduced SERS signal of GNPs with 10% Raman reporter surface coverage. BS153 and IMA2.1 cells were incubated with GNPs coupled to 84 anti-EGFR antibodies. Unconjugated GNPs were incubated with BS153 cells. Anti-EGFR GNPs were detected by fluorescent staining, Raman (scale bare 30 µM) and as bright points by dark field microscopy (pictures taken with hyperspectral imaging system, CytoViva, Inc, US, scale bar 50 µM).

Based on these results, GNPs functionalized with 50% Raman reporter and 50% PEG showed the balanced chemistry surface to enable a clear detection of GNPs while reducing non-specific binding. Further, improved binding specificity was confirmed by transmission electron microscopy imaging that showed a higher number of anti-EGFR GNPs internalized by BS153 cells compared to the negative controls (Figure 20). Consistently, these particles were used for further *in vitro* experiments.
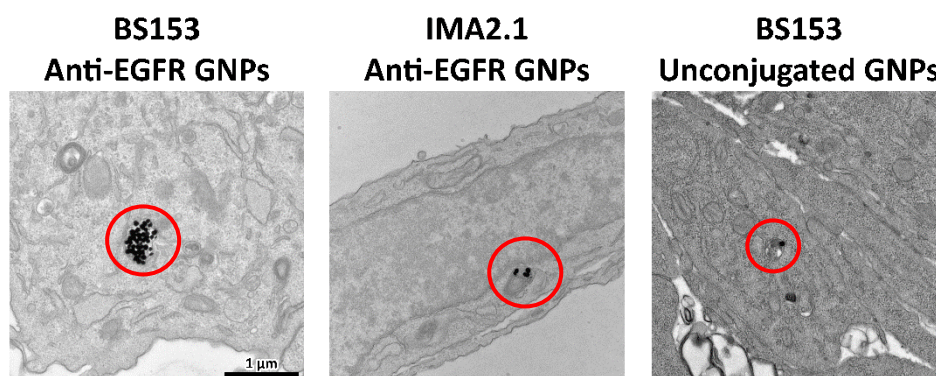
Figure 20. Improved binding specificity of GNPs with balanced surface chemistry. Transmission electron microscopy pictures of BS153 and IMA2.1 cells incubated with anti-EGFR or unconjugated GNPs functionalized with 50% Raman reporter and 50% PEG. Red circles highlight internalized particles. Images captured with FEI Tecnai T12 transmission electron microscope, acceleration voltage 80 kV. Scale bar 1 µM.

3.3 *In vitro* studies of GNPs transit through the BBB

A major concern of targeting brain tumor cells is the ability of GNPs to cross the BBB. This was evaluated *in vitro* using a transwell BBB model. The simplest form of transwell model consists of a monoculture of brain endothelial cells seeded on the apical surface of a support filter as shown in figure 20.
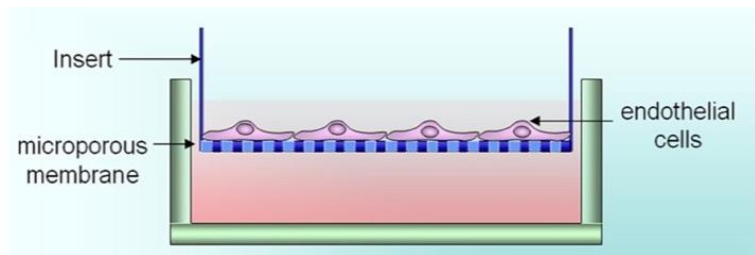
Figure 21. Illustrative representation of an *in vitro* transwell BBB model [104].

3.3.1 Characterization of the BBB model

The human brain endothelial cells, hCMEC/D3 (referred as D3), were used for the creation of the BBB model. Formation of a continuous and functional tight monolayer was observed after 5 days of culture on the insert membrane. Cells then expressed the TJs proteins ZO-1 and claudin-5 at cell-cell contacts (Figure 21A).
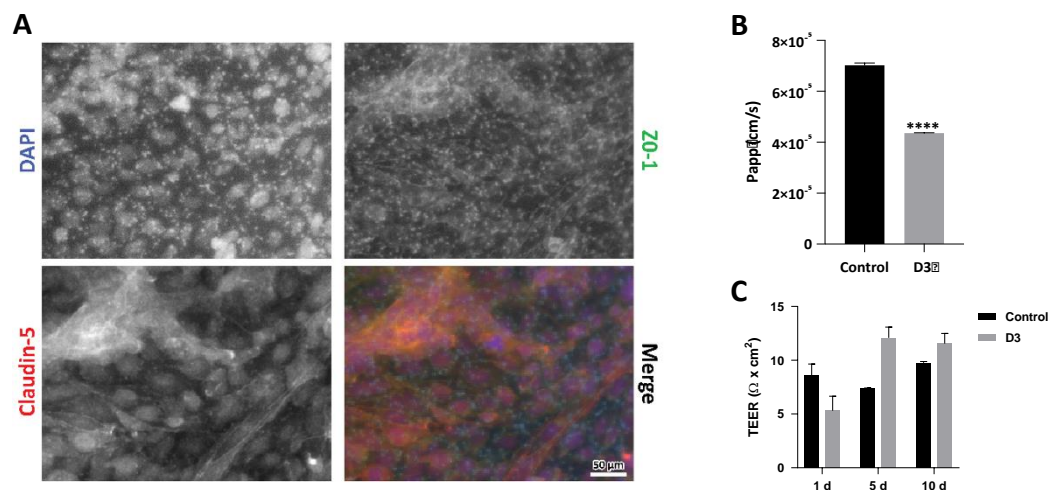
Figure 22. BBB model characterization. A) Expression of BBB markers: TJs proteins ZO-1 and claudin-5 were detected by fluorescent staining in green and in red, respectively. Pictures taken with Axiovert 40 CFL microscope (Zeiss). Scale bar 50 µM. B) Paracellular permeability: 10 µg/ml of LY were added to the apical part of the transwell and, after 1 h of incubation, aliquot was taken from the basolateral chamber and fluorescence read at λ_{ex} 428 nm; λ_{em} 540 nm using FlexStation 3 microplate reader (Molecular Device, LCC). ****$p \leq 0.0001$ vs control (transwell with only collagen), n=3, mean ± SD. C) 2×10^4 cells were seeded into the apical part of the transwell and let attach overnight. TEER values were recorded over 10 days with CellZscope instrument (NanoAnalytics, GmbH); control (transwell with only collagen), n=2, mean ± SD; D3, n=4, mean ± SD.

Barrier integrity was also tested by measuring its paracellular permeability to lucifer yellow (LY) in apical to basolateral direction. Higher restriction was exerted by the cells compared to the control inserts without endothelial cells (Figure 21B). Despite barrier formation appeared to be successful, TEER was found to remain at constant low levels and was only slightly higher compared to transwell inserts without cells after 5 days (figure 21C). Longer cell culture time up to 10 days did not help to achieve higher TEER values and the formation of multiple cell layers was often observed after prolonged period of culture.

3.3.2 Transport of GNPs across the BBB

To investigate the permeation of GNPs through the BBB, 10 and 35 µg/ml of anti-EGFR GNPs were added to the apical side of the inserts after 6 days of culture. After 24 h of incubation, the presence of gold in the basolateral medium was measured by ICP-MS.
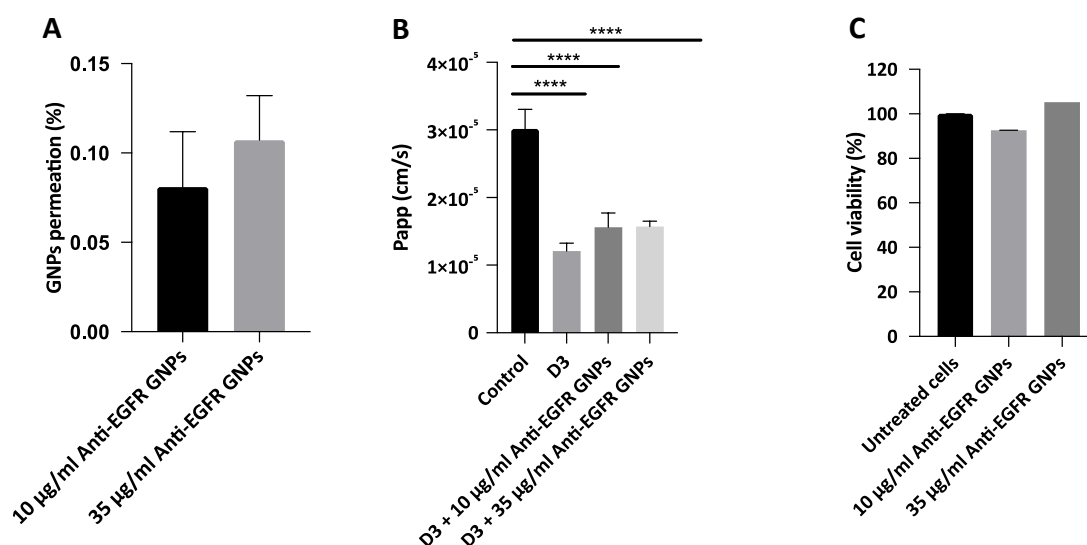
Figure 23. Passage of GNPs through an *in vitro* BBB. After 24 h of incubation with 10 and 35 µg/ml anti-EGFR GNPs: A) Amount of gold was measured in the basolateral chamber with 8800 ICP-qqq-MS instrument (Agilent technologies), n=3, mean ± SD; B) Cell monolayer integrity was evaluated by measuring the paracellular permeability of LY. ****$p \leq 0.0001$ vs control (transwell with only collagen), n=3, mean ± SD; C) Cell viability was determined by the release of formazan. Absorbance was read at 450 nm using FlexStation 3 microplate reader (Molecular Device, LCC). Values expressed as percentage of negative control (untreated cells), n=3, mean ± SD.

About 0.08% and 0.1% of the applied concentrations of gold (10 e 35 µg/ml, respectively) were found to go through the cell monolayer and the membrane of the insert (Figure 22A). The effects of GNPs on BBB integrity were monitored by measuring

the LY permeability (Figure 22B). Even in this case, higher restriction was exerted by the cells compared to the control inserts. Moreover, the permeability of the inserts exposed to GNPs was only slightly higher compared to the untreated cells, meaning that cell monolayer integrity was preserved. Furthermore, both concentrations of GNPs did not affect cell viability (Figure 22C). TEER values also remained unchanged after 24 h of incubation with 10 µg/ml of anti-EGFR GNPs as monitored in a separate experiment (data not shown).

4. Discussion

Improved visualization of brain tumor cells during Raman intraoperative surgery can be achieved by using anti-EGFR GNPs as SERS tags. Surface functionalization is shown to significantly influence anti-EGFR GNPs performance. Indeed, an appropriate combination of the functionalities immobilized on the gold surface is required, especially when the gold core is used as the only accessible surface for all the functionalities as done in this thesis. This decision was made to keep the size of anti-EGFR GNPs as small as possible due to the requirement to cross the BBB in the clinical situation. Hence, the challenge was to combine the three essential components: i) Raman reporter for a maximal SERS signal; ii) inert, protective PEG coating to prevent non-specific binding; iii) and antibody with high receptor binding affinity towards tumor cells, in order to obtain the highest and most specific SERS signal. Finding the optimal balance among these three components depends on the accurate characterization of GNPs. This was one of the main challenges met in this project due to the limited sensitivity of the analytical methods available. Indeed, several techniques, such as X-ray photoelectron spectroscopy, Fourier-transform infrared spectroscopy or energy dispersive X-ray were used but none of them allowed a sensitive detection of surface binding ligands. Possible solution would be to scale up the production process to facilitate their analysis.

4.1 Raman reporter to enhance SERS signal

The SERS enhancement mechanism was confirmed by the assessment of the two strong Raman bands, assigned to ring breathing and ring stretching vibrations [105], which showed 35 and 55 times higher signals for 1,4-BDT immobilized on GNPs compared to free 1,4-BDT, respectively. Furthermore, characteristic SERS peaks of the immobilized 1,4-BDT were shifted and broadened while others disappeared. These changes arise because of the formation of surface complexes upon immobilization [36].

Within the range of tested surface coverages, from 10 to 10-fold excess, the highest SERS signal was recorded at 100% 1,4-BDT.

Despite the presence of multilayers at 10-fold excess surface coverage, SERS signal improved of only 18% compared to the one achieved at full monolayer surface coverage. This is counterintuitive since SERS enhancement is a long-range effect and extends to approx. 10 nm away from the metallic surface. Based on the distance dependence decay, a contribution of the subsequent layers from 77% to 46% for a distance of 0.8 nm (second layer) to 2.4 nm (fourth layer), respectively, from the gold surface would be expected [50]. However, it is worth mentioning that metallic surface only influences chemically molecules in first layer. In addition, at large surface coverage, the adsorption geometry may vary and the LSPR and the electromagnetic properties of the Raman reporter may be affected [36]. The absence of the band at 536 cm^{-1} that usually dictates the formation of S-S bond [106], the relatively low coating thickness of 0.8 nm of the Raman reporter monolayer [51] and the protonation of thiol group at pH 6.5 - 7 further implied that the formation of multilayers rather involved π-π stacking than S-S bond. This explained the unaffected size and charge of GNPs.

4.2 Inert coating to prevent non-specific adsorption

In order to prevent non-specific interactions and for increased biocompatibility, the inert, protective coating of PEG was necessary. Under the assumption that the more complete the PEG functionalization, the better the stability and the reduction of non-specific binding, 100% PEG surface coverage was only possible on GNPs without 1,4-BDT. Then, the higher the surface coverage percentage of 1,4-BDT, the lower the amount of PEG up to inhibition of its binding for 100% Raman reporter surface coverage. Experimental results confirmed a progressively decreasing PEGylation process that however involved even GNPs with full Raman reporter surface coverage. Chen *et al.* showed that PEG conformation is dependent on its density [67]. At higher surface coverages it stretches out in a brush conformation explaining the increased hydrodynamic size up to 14 nm of GNPs functionalized with 0 to 25% 1,4-BDT (Figure 5A, see results, page 45). Conversely, at lower surface coverages it assumes a mushroom configuration with a radius of gyration as low as 2.8 nm justifying the negligible change

in size of GNPs with 50 and 100% 1,4-BDT. However, GNPs with full Raman reporter surface coverage were found to be noticeably prone to random aggregation after conjugation of anti-EGFR antibody at surface coverages equal and higher than 3%. Aggregation was accompanied by an increased average size of 140 nm (consistent with the formation of dimers), a red shift as well as broadening of the SPR adsorption peak and an optical density (OD) decrease of approx. 30% (Figure 14A, see results, page 53). This indicated that the amount of PEG was too low to maintain GNPs stability. In the worst-case, GNPs with full Raman reporter surface coverage underwent aggregation followed by precipitation that was visibly detected by the change in color of the suspension from red to violet or to transparent and OD decrease to the baseline. In addition, GNPs with full Raman reporter surface coverage showed a stronger negative charge (-33 ± 0.8 mV) (Figure 6A, see results, page 46). If on one hand, value < -30 mV are known to make GNPs more stable due to electrostatic repulsions [107], on the other hand the same particles displayed a high level of non-specific binding with cells similarly to what observed in literature with quantum dots (QDs) [108], [109]. Moreover, the higher the surface coverage percentage of 1,4-BDT, the higher the degree of non-specific binding. Indeed, GNPs with 10 and 25% Raman reporter surface coverages exhibited a reduction of non-specific interaction with the cell surface up to 100%. This had less to do with the surface charge, which was still negative (-26 ± 2.5 and -31 ± 2.2 mV, respectively) than to the passivation of GNPs surface because of the presence of PEG [108]. Nonetheless, decreasing the amount of Raman reporter to 10 and 25% surface coverages on behalf of PEG resulted in the complete depletion of Raman sensitivity after incubation of GNPs with cells. This could be overcome by increasing the integration time (from 0.05 to 0.5 sec) or reducing the working distance (from 16.5 to 0.3 mm). However, both methods meant longer acquisition times and are not desirable in view of the final clinical application.

Consistently to what discussed so far, 50% Raman reporter surface coverage was identified as the percentage to achieve the optimal balance. In fact, despite a theoretical value of approx. 30'000 molecules of PEG per GNP has also been reported by Qian *et al.* to be necessary to stabilize gold colloids against aggregation [53], approx. 16'000 PEG molecules were already sufficient to prevent aggregation. 80% reduction of non-specific binding was observed on IMA2.1 incubated with anti-EGFR GNPs compared to the

particles with full Raman reporter surface coverage. Persisting non-specific binding in BS153 incubated with unconjugated GNPs was attributed to highly negative carboxylated GNPs (-34 ± 2.2 mV). A possible alternative to reduce non-specific binding, without affecting Raman sensitivity, was acting on GNPs surface charge by the deactivation of the residual carboxy-end terminated PEG with ethanolamine or aPEG. This strategy has been successful adopted for QDs [109] where weakening the electrostatic interactions led consequently to the reduction of non-specific binding with cell membranes. Indeed, it worked successfully for unconjugated GNPs treated with ethanolamine (Figure 17A, see results, page 56), whose non-specific binding was completely suppressed. Though, a complete suppression of antibody activity after deactivation of anti-EGFR GNPs was observed probably due to side reaction with the anti-EGFR binding sites.

This confirmed that it is not necessary to functionalize every site on the surface of nanoparticles to reduce non-specific binding as also defined by Benzten *et al.* [108] as long as it is accompanied by the deactivation of negatively charged groups on GNPs surface (either through antibody conjugation or blocking agents). Therefore, we suggest using nanoparticles conjugated to a non-specific IgG as proper negative control for non-specific binding.

At the same time, Raman sensitivity was reduced of 40% compared to the particles with full Raman reporter surface coverage. However, it was high enough for a sharp detection of GNPs detected in the picomolar range in agreement to what reported by Kircher *et al.*[10].

4.3 Antibody concentration for improved active targeting

PEG surface coverage influenced the GNPs stability also in terms of the possible number of antibodies conjugated. If, on one hand, GNPs with maximum surface coverage of Raman reporter were susceptible to aggregation when antibody surface coverage was equal or higher than 3%, on the other hand, GNPs with 10 or 25% Raman reporter surface coverage allowed conjugation of antibody surface coverages up to 30%. Independently on the amount of antibody used, the hydrodynamic size of anti-EGFR GNPs compared to the unconjugated ones was compatible with its horizontal

orientation on the GNPs surface since the length of the IgG is approximately 7–10 nm [110]. Despite conjugation protocol with ethyl dimethylaminopropyl carbodiimide (EDC) /N-hydroxysulfosuccinimide (sulfo-NHS) did not allow to control the orientation of the antibodies, they kept their functionality after conjugation. Even though increasing the number of antibodies up to 10 times in the conjugation reaction gave rise to a higher antibody content at the surface of GNPs, the conjugation efficiency remained significantly low from 40 to 5% resulting in 64 and 84 antibodies per GNP, respectively. Moreover, higher number of antibodies per GNP did not help enhancing the Raman sensitivity if compared to the lower amount and suggested that the excess of antibodies is not necessary for improved active binding of the GNPs to the cellular target. The phenomenon in which increasing the number of antibodies per GNP does not increase the binding affinity was already observed by Elias *et al.*, who showed that an intermediate ligand density provided statistically significant improvements in cell binding in comparison to higher and lower densities [111]. This trend can be explained by examining the state in which the EGFR resides on the cellular membrane. Needham *et al.* have reported that EGFR exists as "receptor clusters" whose diameter goes from 8 (dimers) to 57 nm (homo-polymers of 10 receptors). Considering the calculated number of antibodies and assuming a homogeneous distribution beside a straight and site control orientation of the antibodies on GNPs, there would be a maximum distance of 10 nm between two molecules. This would mean that only in case of dimers two antibodies would be able to bind two close dimers while, in case of cluster, up to 5 antibodies would be occupied to bind several receptors in the same cluster preventing other GNPs from binding to the same cluster. In real conditions, inhomogeneous distribution and random orientation of the antibodies would rather increase the steric hindrance causing competition between two close molecules for a single receptor and limiting the access that antibodies have to the receptors [110]. Despite here retention of functionality was shown, investigation of the number of antibodies with unaltered functionality was not carried out and lack of control for ligand orientation could result in antibodies with reduced or eliminated functionality thus altering the perceived "functional" density of ligands. The size of GNPs has further to be considered since it is almost 90 or 30% bigger compared to one dimer or one cluster, respectively. In this case, the shielding would be due to cellular EGFR interaction with the nearby GNPs. The

considerations set out so far are summarized in figure 1.

Anti-EGFR GNPs showed stability in cell culture medium and negligible cytotoxicity on GBM cells over a period of 24 h confirming what reported in literature [10]. GNPs selective uptake by GBM tumor cells in culture was concentration and time-dependent with the optimum incubation time fixed to 4 h. This is in agreement with their final clinical application considering that GBM surgery lasts in average 4 h. Furthermore, anti-EGFR GNPs allowed SERS based imaging of all EGFR-positive GBM cells, including cells expressing EGFRvIII such as BS153, which were known not to show any fluorescence after 5-ALA administration [15]. This opens a new chance to visualize even those GBM or low-grade glioma that are known not to respond to 5-ALA treatment.
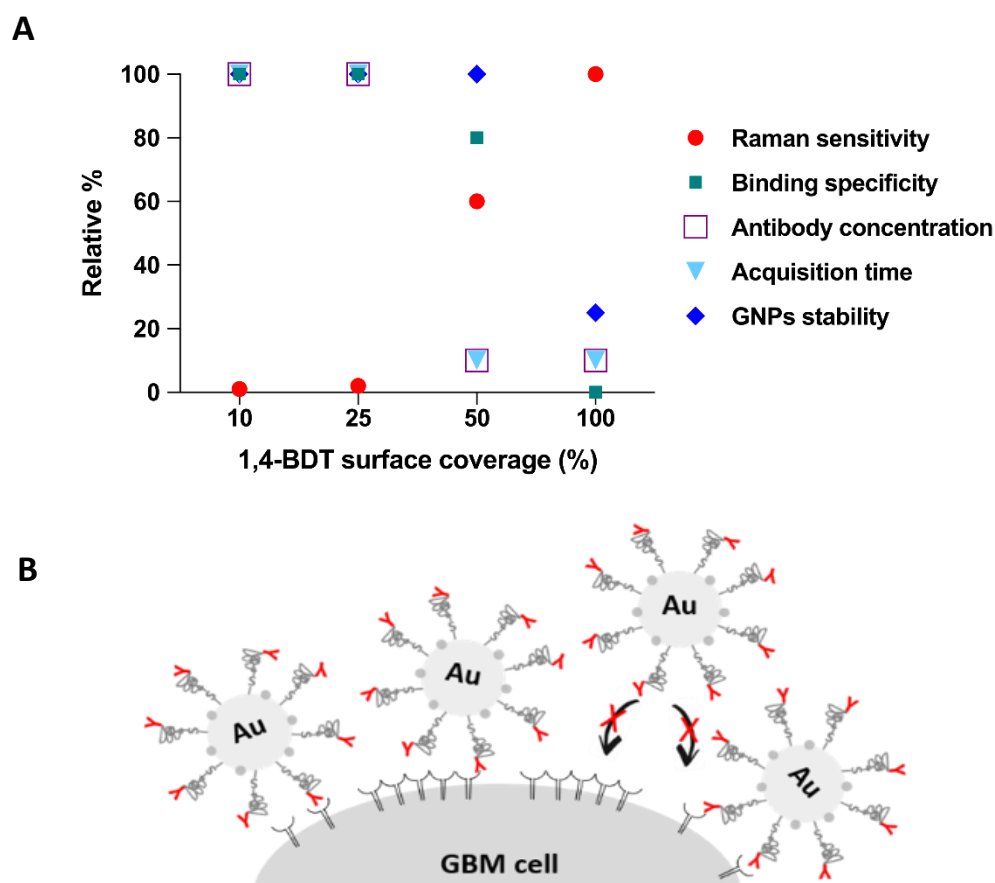
Figure 1. Illustration of the principal findings. A) Correlation between increasing 1,4-BDT surface coverages and Raman sensitivity, cellular binding specificity, applied concentration of anti-EGFR antibodies, acquisition speed and gold colloidal stability. Results are presented as relative percentage to the highest value recorded (100%) for each parameter. B) Possible organization of EGFR on the GBM cell membrane and interaction with anti-EGFR GNPs.

4.4 Crossing the BBB

Higher performance of anti-EGFR GNPs with 50% surface coverage of Raman reporter and PEG presented in this study, especially in terms of detection sensitivity and binding specificity, give reasons for further investigations *in vivo* using animal models before moving to the final clinical application. However, a major criticism regarding the injection of GNPs *in vivo* is their strongly limited delivery to the brain due to the BBB. Thus, anti-EGFR GNPs showed to be able to cross the *in vitro* BBB model without altering the barrier integrity. Indeed, about 0.1% of the initial applied concentration of GNPs was found in the basolateral compartment of a transwell system mimicking the BBB after 24 h of incubation. This percentage needs to be improved but it was deemed promising considering the 0.3% of 10 nm GNPs or 0% of 50 or 100 nm particles present in the brain after intravenous administration in rats [65]. Furthermore, when working with an *in vitro* BBB model like the one described, it is worth keeping in mind technical limitations such as GNPs adhesion to the transwell pores of the filter or agglomeration within the pores, thus obstructing the transport [101]. The estimation of the delivery through the membrane could therefore be underestimated. Application of GNPs in animal models would further address some critical issues that could limit their use such as long-term stability in the blood circulation by escaping the opsonization processes, toxicity at higher dosage, possible immune responses, biodistribution and elimination from the body. Further, human EGFR-positive GBM cells xenograft in mice brains mimicking closely the BBB could pave the way for a deeper and more reliable understanding of the ability of anti-EGFR GNPs to reach their final targets. Despite *in vivo* exploration is mandatory, the ability of SERS based imaging to visualize *in vitro* GBM cells with high sensitivity and specificity, when GNPs are properly engineered, is promising for its definitive implementation in the operation room to identify and remove residual cancer cells for better outcomes of patients suffering from brain tumors.

5. Conclusions and outlooks

To achieve a complete resection of GBM during surgical operation, improved visualization of residual cancer cells is indispensable. Raman based imaging, coupled with GNPs as SERS tags, offers several advantages over current visualization technologies as long as GNPs with high stability, Raman sensitivity and binding specificity to tumor cells are produced. In view of this, this work provided a noteworthy understanding of the influence that surface functionalization exerts on GNPs performance for SERS based imaging. Non-toxic SERS tags were developed with several ratios of inert and receptor specific active molecules. Full Raman reporter or PEG surface coverage maximized Raman sensitivity and binding specificity, respectively. However, these statements were valid only when considered individually. Therefore, the optimal balance among all the functionalities was identified to allow a fast, sensitive and specific Raman detection of GBM cells. It was even shown that higher amounts of antibody on the GNPs surface did not improve the cellular binding stressing that the optimal ligand concentration does not always match the highest. In addition, the ability of anti-EGFR GNPs to cross a BBB model *in vitro* was attested.

With regards to GBM, whose challenging treatment pushed the start of this study, the results revealed the potential of SERS based imaging to visualize GBM or low-grade gliomas, which show variable fluorescence or do not respond after 5-ALA administration. Moreover, they would justify further *in vivo* experiments using animal models. A possible strategy would also involve the conjugation of more than one moiety on GNPs either to target two different cell types within the same tumor or to improve specificity toward a single cancer cell type prone to extreme heterogeneity of overexpressed cell surface receptors, as observed in GBM. Even using GNPs with rod shape could be beneficial since it would reduce significantly the size (approx. 3 times smaller) of conjugated particles facilitating their ability to cross the BBB and to reach their targets.

The considerations raised in this work can be extended to the visualization of any other kind of tumor and to any other application implying the use of GNPs. By clarifying the effect of surface chemistry on SERS tags specificity, affinity and sensitivity, this work adds new aspect to the current literature. It also highlights the need to perform a detailed characterization of SERS tags to clearly distinguish between theoretical added functionalities and the ones effectively present on the surface of the nanoparticles. Only the conscious knowledge of SERS tags properties allows to achieve a system with high reproducibility and reliability to give to the clinicians an adequate tool to reduce the occurrence of relapses thus improving patients survival.

6. Materials and methods

6.1 Nanoparticles functionalization

Ultrapure water (18.2 mΩ/cm) was used throughout the work. GNPs suspension, dimethyl sulfoxide (DMSO) and 0.1 mM phosphate buffered saline (PBS) were degassed under nitrogen in the ultrasound for 1 h. Citrate stabilized GNPs (60 nm diameter) were used. Raman reporter, 1,4-BDT, was dissolved in DMSO and 0, 1, 2, 4 or 40 μl of 1 mM solution were added to 1 ml of GNPs suspension (1.9 x 10^{10} particles per ml) and sonicated for 1 h at 25°C. 400 μl of 0.4 μM cPEG (3.5 kDa) solution were added to the Raman active GNPs before sonication for 1 h at 25°C followed by mixing for 4 h at 25°C at 750 rpm. 600 μl of 10 μM mPEG (5 kDa) were added and samples were incubated overnight at 25°C at 750 rpm. To remove the excess of PEG, samples were centrifuged for 30 min at 4'500 rpm and resuspended in 1 ml of 0.1 mM PBS. To activate the carboxy groups, 200 μl of 5 μM EDC/sulfo-NHS mixture were added to the samples and mixed for 20 min at 25°C at 750 rpm. To remove the excess of EDC/sulfo-NHS, samples were centrifuged for 30 min at 4'500 rpm and resuspended in 0.5 ml of 20 mM 4-(2-hydroxyethyl)-1-piperazineethanesulfonic acid (HEPES) buffer, pH 7.4. Activated carboxy groups were covalently linked to 4, 10 or 40 μl of 200 μg/ml rabbit anti-EGFR antibody (10001-R021) for 2 h at 25° C at 750 rpm and the mixture was kept overnight at 4°C. Unbound antibodies were separated from anti-EGFR GNPs by two centrifugations for 30 min at 4'500 rpm. The final pellet was resuspended in 0.1 mM PBS and stored at 4°C. Unconjugated GNPs were synthetized by using the same procedure but 0.1 mM PBS was added instead of anti-EGFR antibodies. To modulate surface charge of GNPs, 1% (v/v) ethanolamine or 1 μl of 1.5 mM solution of aPEG (750 Da) was added to anti-EGFR and unconjugated GNPs either after 2 h or overnight incubation of GNPs with anti-EGFR antibodies. All chemicals were purchased from Sigma-Aldrich, except

mPEG and anti-human EGFR antibody that were obtained from Rapp polymere and Sino biological, respectively.

6.1.1 Nanoparticles characterization

UV-Vis spectra were acquired in the range 400-700 nm, 1 nm step, with Sinergy H1 microplate reader (BioTek Instrument, GmbH). GNPs concentration was calculated by using a calibration curve (R^2=0.9988) from known concentrations of bare GNPs and relative absorbance at 450 nm.

Hydrodynamic size distribution by Dynamic light scattering and zeta potential were determined with Zetasizer ZS dynamic light scattering instrument (Malvern Panalytical Ltd, UK). Each sample was measured at 25°C, pH 7.

For transmission electron microscopy analysis, 2 µl of bare GNPs were placed onto standard 3.5 mm transmission electron microscopy grid (Formvar/Carbon 200 Mesh, Copper grids). After drying, grid was rinsed with milliQ water and visualized with EM 900 transmission electron microscope (Zeiss), acceleration voltage 50 kV.

SERS spectra of dry GNPs were recorded with confocal Raman alpha300 R microscope (Witec, GmbH, Germany) equipped with a 785 nm excitation wavelength. Laser power was set at 50 mW with an integration time of 0.5 sec, 10 accumulations, 50x objective unless otherwise specified. Spectra were processed with Witec Project 4.1 software.

ICP-MS was used to quantify the amount of gold and thiol ligand (by sulfur measurement). To avoid overestimation of sulfur, GNPs were functionalized as described above but acetone, instead of DMSO, was used to dissolve 1,4-BDT. Quantification was carried out using an external calibration from single-element standards (Sigma-Aldrich) prepared in milliQ water from 0-100 µg/L. Samples were diluted accordingly and analyzed with 8800 ICP-qqq-MS system (Agilent technologies). Au quantification was performed on $^{197}Au^+$ using helium as a collision gas (5 ml/min),

$^{32}S^+$ was measured in triple quad mass-shift mode using O_2 as a reaction gas. $^{103}Rh^+$ was used as an internal standard to account for possible matrix effects.

6.1.2 Quantification of the number of antibodies per nanoparticle

To quantify the number of antibodies per GNP, an excess of Alexa Fluor® 680 goat anti-rabbit antibody (Invitrogen) was added to the anti-EGFR and unconjugated GNPs. Known concentrations of the antibody were used to prepare a standard curve. Samples and the standards were mixed for 1 h at 25°C at 450 rpm. Samples were then washed twice with PBS 0.1 mM for 15 min at 4'500 rpm to remove any residual free antibody. Fluorescence detection was performed with Odyssey® CLx infrared imaging system (Li-cor, Biosciences). The fluorescence of unconjugated GNPs was used to estimate the fluorescence signal due to absorbance by GNPs and the non-specific binding of secondary antibody. The number of antibodies per GNP was determined by using the calibration curve (R^2=0.98581) and by normalizing the result to total amount of GNPs in the sample as measured by absorbance values.

6.1.3 Nanoparticles optical stability in cell culture medium

To evaluate the impact of biological media on GNPs stability, anti-EGFR and unconjugated GNPs were diluted 1:2 in DMEM (Sigma-Aldrich) supplemented with 10% FCS (Sigma-Aldrich) and 1% penicillin–streptomycin (P/S) (Sigma-Aldrich). Samples were run for 24 h at 37°C at 450 rpm. Absorbance at 450 nm was measured after 0, 1, 2, 4, 6, 8 and 24 h.

6.1.4 Immuno dot blot

Antibody functionality after conjugation onto GNPs was evaluated by immuno dot blot. 2 µl of 250 µg/ml human recombinant EGFR (Sino Biological) were spotted onto nitrocellulose membrane (GE Healthcare). After blocking with 1% (w/v) dry milk for 30 min at room temperature (RT), membrane was incubated with 70 µl of 40 µg/ml anti-EGFR or unconjugated GNPs for 3 h at RT. Membrane was washed three times for 5 min

with blocking solution and the presence of bound GNPs (bright pink spot) was visually evaluated.

6.2 Cell culture

The following cell lines were used to carry out *in vitro* experiments: the human GBM cell line U87MG was obtained from ATCC; the human GBM cell line BS153 was provided by Prof. Monika Hegi (University Hospital Lausanne, Switzerland); the human GBM cell line LN229, overexpressing the *EGFR* gene (LN229wtEGFR), was provided by Prof. Michael Weller (University Hospital Zürich, Switzerland); the immortalized astrocyte cell line IMA2.1 was provided by Dr. Stefan Schildknecht (University of Konstanz, Germany) and was used as EGFR-negative cell line. Cells were cultured in DMEM, supplemented with 10% FCS and 1% P/S. To maintain high EGFR expression level in LN229wtEGFR, medium was enriched with 60 μg/ml hygromycin B (Sigma-Aldrich). All the cells were kept at 37°C, in a 5% CO_2 atmosphere.

6.2.1 Fluorescence staining

Cellular EGFR expression was investigated by fluorescent immunocytochemistry. At 80% confluency, cells were fixed with 4% (v/v) paraformaldehyde (PFA) (Thermofisher Scientific) for 10 min at RT and permeabilized with 0.2% (v/v) Triton X-100 in PBS + 5% (v/v) normal donkey serum (NDS) for 20 min at RT. Cells were incubated with rabbit anti-human EGFR antibody, diluted 1:250, overnight at 4°C, then with FITC donkey anti-rabbit antibody (Jackson ImmunoResearch), diluted 1:300, for 1 h at RT. Cell nuclei were stained with 300 nM DAPI (Sigma-Aldrich) added to the secondary antibody. Slides were mounted in FluorSave™ Reagent (Calbiochem) and pictures taken with a F-View camera coupled to DMRE microscope (Leica Microsystem). Washings with PBS were performed between each step for 5 min each.

6.2.2 Western blot

Cellular EGFR expression was evaluated by western blot. Whole-cell extracts were obtained by lysing cell pellets in radioimmunoprecipitation assay buffer enriched with

protease inhibitors (Sigma-Aldrich), diluted 1:100. Protein concentration was determined using the bicinchoninic acid protein assay kit (Thermofisher Scientific). 30 µg of protein extracts were separated in a 8% precast polyacrylamide gel (Invitrogen) and transferred onto polyvinylidene difluoride (PVDF) membrane (Merk Millipore) by wet electroblotting. Membrane was blocked with Odyssey® blocking buffer (Li-cor, Biosciences) for 1 h at RT and incubated with rabbit anti-human EGFR and goat anti-human actin antibodies (Abcam), diluted 1:500 and 1:1'000 respectively, overnight at 4°C. IRDye® 680 donkey anti-goat (Li-cor, Biosciences) and Alexa Fluor® 680 goat anti-rabbit antibodies, diluted 1:10'000, were then added for 1h at RT. Blot was scanned with Odyssey® CLx infrared imaging system (Li-cor, Biosciences). Washings with PBS-T were performed between each step for 5 min each.

For the evaluation of antibody functionality after conjugation onto GNPs, human recombinant EGFR protein (1.9 µg) was separated in a 8% precast polyacrylamide. Protein was transferred onto PVDF membrane by wet electroblotting and incubated with anti-EGFR or unconjugated GNPs for 3 h at RT. Anti-EGFR antibodies on GNPs were probed with Alexa Fluor® 680 goat anti-rabbit antibody, diluted 1:10'000. Blot was then scanned with Odyssey® CLx infrared imaging system (Li-cor, Biosciences).

6.2.3 Quantitative expression of EGFR at the cell membrane

To quantify EGFR expressed at the cell membrane of each cell line, qFACS was performed by using QIFIKIT®* (Dako) according to the manufacturer's instructions. Briefly, 10^6 cells/ml were incubated with a saturating concentration (1 µg/ml) of mouse anti-human EGFR antibody (BioXCell) for 1 h at 4°C in the dark. Incubation without primary antibody served as negative control. To prevent EGFR internalization, cells were washed for 5 min at 4°C at 2'500 rpm and fixed with 1% PFA for 10 min at RT and incubated with FITC goat anti-mouse antibody (supplied in the kit) diluted 1:50 for 45 min at 4°C in the dark. Cells were centrifuged three times for 5 min at 4°C at 2'500 rpm and resuspended in 0.1 M Ethylenediaminetetraacetic acid + 1% (w/v) bovine serum albumin (BSA). Cells were analyzed with CytoFlex S flow cytometer (Beckman Coulter). Data were subsequently processed with FlowJo 10.4 software. EGFR density/cell was

obtained by comparing the mean fluorescence intensity (MFI) of the cells to the MFI of five populations of calibration beads with known numbers of antibody binding sites used to generate a standard curve. Values were corrected for the autofluorescence signal of cells and for unspecific binding of the secondary antibody on negative controls.

6.2.4 GNPs cytotoxicity

To determine GNPs cytotoxicity, LN229wtEGFR were plated at a density of 1×10^3 cell/well in a 384 well plate and allowed to attach for 2 h at 37°C. Then, 4×10^5 anti-EGFR GNPs/cell were added to each well. Cells incubated only with medium were used as control. After 24 h of incubation, 100 µl of fresh phenol free-DMEM (Thermofisher Scientific) containing 10% of cell counting kit 8 reagent (Sigma-Aldrich) were added to each well for 3 h at 37°C. The amount of formazan dye generated, directly proportional to the number of live cells, was measured with Sinergy H1 microplate reader at 450 nm. Cell viability was calculated as the ratio of the absorbance of the samples incubated with GNPs to that of the control and expressed as percentage of untreated control cells.

6.3 *In vitro* cancer cell targeting

To investigate the specificity of particle binding, EGFR-positive GBM and EGFR-negative cells were grown into 8 wells chamber slide until confluence. Anti-EGFR or unconjugated GNPs were added to each well at the concentration range of 5-70 µg/ml over 24 h. 30 min before the end of the incubation time, cells were incubated with 50 nM LysoTracker™ Deep Red (Thermofisher Scientific). To remove unbound GNPs, cells were washed three times with PBS for 10 min and fixed with 4% PFA for 10 min at RT. Staining of anti-EGFR GNPs was performed by using Alexa Fluor® 488 donkey anti-rabbit antibody (Abcam), diluted 1:250, for 1 h at RT. Cell nuclei were stained with 300 nM DAPI (Sigma-Aldrich) added to the secondary antibody.

Raman measurements were carried out with confocal Raman alpha300 R microscope (Witec, GmbH, Germany) equipped with a 785 nm excitation wavelength. Laser power was set at 25 mW with an integration time of 0.05 sec, 50x objective. Raman maps were

generated by plotting the SERS signals of 1,4-BDT bands at 1'058 cm^{-1} and 1'556 cm^{-1}. Fluorescence images were acquired from the same sample spots for comparison with their SERS images. For quantification of SERS signal, pictures of three random areas for each specimen were converted in 16-bit images and quantify with Image j software. Area (1'000 x 500 pixel), % area was used for comparison, gray value threshold 35-65'535.

Cellular distribution of anti-EGFR GNPs was investigated with laser confocal scanning microscope FV1000D (Olympus). Pictures were analyzed with Image J software.

Dark field analysis was done using hyperspectral imaging system (VNIR Version, CytoViva, Inc, US).

Cellular uptake of GNPs was investigated by transmission electron microscopy imaging. Briefly, 3.5 x 10^6 BS153 and IMA2.1 cells were seeded into 100-cm plate overnight. 10 µg/ml of anti-EGFR or unconjugated GNPs were added for 4 h under agitation. Cells were washed three times with PBS for 10 min and fixed with 1:1 (v/v) medium-double strength fixative mixture for 20 min. Cells were harvested using a cell scraper and centrifuged at 600 rpm for 5 min. Supernatant was replaced with single strength fixative for at least 45 min. Cells were washed three times and resuspended in cold washing buffer.

Double strength fixative in normal strength buffer (0.1 M): 4% PFA (Electron Microscope Science) + 5% Glutaraldehyde (GA, Electron Microscope Science) in 0.1 M piperazine-N,N'-bis(2-ethanesulfonic acid) (PIPES, Sigma-Aldrich) buffer pH 7.0-7.2. Single strength fixative: 2% PFA + 2.5% GA in 0.1 M PIPES buffer pH 7.0-7.2. Washing buffer: 0.1M PIPES buffer pH7.0-7.2.

The following steps were performed at the BioEM lab (C-Cina, University of Basel). Fixed cells were embedded in agarose (Sigma-Aldrich), post-fixed in 1% buffered osmium tetroxide (Electron Microscope Science) for 1 h at 4°C and stained with aqueous uranyl acetate (Electron Microscope Science) for 1 h at 4°C in the dark. Samples were dehydrated in an ethanol series (30, 50, 75, 95 and 100%), washed in acetone and finally embedded in pure Epon 812 resin (Electron Microscope Science) for 48 h at 60°C. Cut

sections were placed on copper grids and observed with FEI Tecnai T12 transmission electron microscope operating at 80 kV. Images were recorded using a CCD Veleta digital camera.

6.4 *In vitro* BBB model

The human endothelial cell line hCMEC/D3 was provided by Prof. Luc Stoppini (Hepia-Haute ecole du paysage, d'ingenierie et d'architecture de Geneve, Geneva, Switzerland). Cells were cultured in EndoGRO™-MV complete medium Kit (Millipore, SCME004) supplemented with 1 ng/ml FGF-2 (Thermofisher Scientific) in flasks pre-coated with collagen type I solution diluted 1:20 (Sigma-Aldrich), and kept at 37°C, in a 5% CO_2 atmosphere. To establish the BBB model, 6.5 mm transwell with 0.4 μm pore polyester membrane inserts were used (Sigma, CLS3470). 2×10^4 cells were seeded on the apical surface of the membrane, pre-coated with collagen at density of 10 μg/cm^2 and grown up to 12 days.

6.4.1 Fluorescence staining of TJs

Formation of a tight monolayer was evaluated by detecting the expression of TJs proteins ZO-1 and claudin-5. After 5 days of culture, inserts were fixed with 2% PFA for 10 min at RT, permeabilized with 0.1% Triton X-100 in PBS for 5 min and blocked with 3% BSA in PBS for 1 h at RT. Cells were incubated with Alexa Fluor® 488 mouse anti-human ZO-1 (Invitrogen, ZO1-1A12) and rabbit anti-human claudin-5 antibodies (Abcam), diluted 1:50 and 1:100 respectively, overnight at 4°C, then with Alexa Fluor® 546 goat anti-rabbit antibody (Invitrogen), diluted 1:500, for 45 min at RT. Cell nuclei were stained with 300 nM DAPI for 15 min at RT. Cells were mounted in FluorSave™ Reagent and pictures taken with an AxioCam MRm camera coupled to Axiovert 40 CFL microscope (Zeiss). Washings with PBS were performed between each step for 5 min each.

6.4.2 TEER measurement

Beside traditional permeability assay, the formation of a continuous and tight monolayer was monitored by measuring the TEER. Inserts with hCMEC/D3 cells and with collagen only as control were placed into "cellware" plate, a prototype developed by the group of Prof. Luc Stoppini (Hepia, Geneva, Switzerland). It is provided with an adaptor to be used with CellZscope system (nanoAnalytics, GmbH). Since TEER values are highly temperature sensitive, the plate was placed in the incubator and let to equilibrate at 37°C overnight. The day after, values were recorded in real-time every 4 h and analyzed with the CellZscope software.

6.4.3 BBB permeability assay

To assess the tightness of cell monolayer, paracellular permeability of LY CH dipotassium salt (Sigma-Aldrich) was investigated. Inserts with hCMEC/D3 cells and with collagen only as control were moved into new 24 wells plate containing 600 µl of pre-warmed cell culture medium. 100 µl of 10 µg/ml LY solution were added to the apical chamber of the insert and the plate was placed on an orbital shaker at 100 rpm, at 37°C for 1h. Then 100 µl aliquots were collected from the basolateral chamber and LY fluorescence was read at Λ_{ex} 428 nm and Λ_{em} 540 nm with FlexStation 3 (Molecular Device, LCC). Amount of LY was determined using a calibration curve generated with known concentration of LY diluted in cell culture medium. Apparent permeability coefficient (Papp) was calculated in cm/s according to the following equation: Papp (cm/s) = $V_B/(AC_{AO})$ x ($\Delta C_B/\Delta_T$), where V_B is the volume in the basolateral chamber, A is the surface area of the filter, C_{AO} is the initial concentration in the apical chamber, $\Delta C_B/\Delta_T$ is the change of concentration in the basolateral chamber over time.

6.4.4 Permeation of GNPs through the BBB

After 7 days of culture, the medium in the apical chamber was replaced with 150 µl of 10 or 35 µg/ml of anti-EGFR GNPs to investigate their transport through the BBB. Plate was placed on an orbital shaker at 100 rpm at 37°C for 24 h. At the end of the incubation,

medium was collected from the basolateral compartment and the amount of gold measured by ICP-MS.

6.5 Statistical analysis

Data evaluation was performed with GraphPad Prism 8 (GraphPad Software, inc.) and results are presented as means ± standard deviation (SD) of three independent experiments, unless otherwise specified. The Student t test was used for comparison between two groups, P<0.05 was considered significant. Data from three or more groups were analyzed by one or two-way ANOVA analysis with Dunnet's multiple comparisons test.

References

1. I. Jovčevska, N. Kočevar, and R. Komel, "Glioma and glioblastoma - how much do we (not) know?," *Mol. Clin. Oncol.*, vol. 1, no. 6, pp. 935–941, Nov. 2013.

2. R. Henriksson, T. Asklund, and H. S. Poulsen, "Impact of therapy on quality of life, neurocognitive function and their correlates in glioblastoma multiforme: a review," *J. Neurooncol.*, vol. 104, no. 3, pp. 639–646, Sep. 2011.

3. "About Brain Tumors - Learn More or Donate Today! | ABTA," *American Brain Tumor Association*. https://www.abta.org/about-brain-tumors.

4. "Surgery for Cancer," *National Cancer Institute*, 29-Apr-2015. https://www.cancer.gov/about-cancer/treatment/types/surgery.

5. H. Karabeber *et al.*, "Guiding Brain Tumor Resection Using Surface-Enhanced Raman Scattering Nanoparticles and a Hand-Held Raman Scanner," *ACS Nano*, vol. 8, no. 10, pp. 9755–9766, Oct. 2014.

6. D. G. Barone, T. A. Lawrie, and M. G. Hart, "Image guided surgery for the resection of brain tumours," *Cochrane Database Syst. Rev.*, Jan. 2014.

7. S. Hu, H. Kang, Y. Baek, G. El Fakhri, A. Kuang, and H. S. Choi, "Real-Time Imaging of Brain Tumor for Image-Guided Surgery," *Adv. Healthc. Mater.*, vol. 7, no. 16, p. 1800066, Aug. 2018.

8. D. A. Orringer, A. Golby, and F. Jolesz, "Neuronavigation in the surgical management of brain tumors: current and future trends," *Expert Rev. Med. Devices*, vol. 9, no. 5, pp. 491–500, Sep. 2012.

9. C. Senft, A. Bink, K. Franz, H. Vatter, T. Gasser, and V. Seifert, "Intraoperative MRI guidance and extent of resection in glioma surgery: a randomised, controlled trial," *Lancet Oncol.*, vol. 12, no. 11, pp. 997–1003, Oct. 2011.

10. M. F. Kircher *et al.*, "A brain tumor molecular imaging strategy using a new triple-modality MRI-photoacoustic-Raman nanoparticle," *Nat. Med.*, vol. 18, no. 5, pp. 829–834, May 2012.

11. L. G. Tataranu *et al.*, "Current Trends in Glioblastoma Treatment," in *Brain Tumors - An Update*, A. Agrawal and L. R. Moscote-Salazar, Eds. InTech, 2018.

12. N. Erdoğan, B. Tucer, E. Mavili, A. Menkü, and A. Kurtsoy, "Ultrasound guidance in intracranial tumor resection: correlation with postoperative magnetic resonance findings," *Acta Radiol.*, vol. 46, no. 7, pp. 743–749, Nov. 2005.

13.   M. Ottenhausen, S. M. Krieg, B. Meyer, and F. Ringel, "Functional preoperative and intraoperative mapping and monitoring: increasing safety and efficacy in glioma surgery," *Neurosurg. Focus*, vol. 38, no. 1, p. E3, Jan. 2015.

14.   W. Stummer and E. Suero Molina, "Fluorescence Imaging/Agents in Tumor Resection," *Neurosurg. Clin. N. Am.*, vol. 28, no. 4, pp. 569–583, Oct. 2017.

15.   A. O. Fontana *et al.*, "Epithelial growth factor receptor expression influences 5-ALA induced glioblastoma fluorescence," *J. Neurooncol.*, vol. 133, no. 3, pp. 497–507, Jul. 2017.

16.   P. Schucht *et al.*, "5-ALA complete resections go beyond MR contrast enhancement: shift corrected volumetric analysis of the extent of resection in surgery for glioblastoma," *Acta Neurochir. (Wien)*, vol. 156, no. 2, pp. 305–312, Feb. 2014.

17.   K. Roessler, A. Becherer, M. Donat, M. Cejna, and I. Zachenhofer, "Intraoperative tissue fluorescence using 5-aminolevolinic acid (5-ALA) is more sensitive than contrast MRI or amino acid positron emission tomography (^{18} F-FET PET) in glioblastoma surgery," *Neurol. Res.*, vol. 34, no. 3, pp. 314–317, Apr. 2012.

18.   W. Stummer, U. Pichlmeier, T. Meinel, O. D. Wiestler, F. Zanella, and H.-J. Reulen, "Fluorescence-guided surgery with 5-aminolevulinic acid for resection of malignant glioma: a randomised controlled multicentre phase III trial," *Lancet Oncol.*, vol. 7, no. 5, pp. 392–401, May 2006.

19.   A. Nabavi *et al.*, "Five-aminolevulinic acid for fluorescence-guided resection of recurrent malignant gliomas: a phase ii study," *Neurosurgery*, vol. 65, no. 6, pp. 1070–1077, Dec. 2009.

20.   C. G. Hadjipanayis, G. Widhalm, and W. Stummer, "What is the Surgical Benefit of Utilizing 5-Aminolevulinic Acid for Fluorescence-Guided Surgery of Malignant Gliomas?:," *Neurosurgery*, vol. 77, no. 5, pp. 663–673, Nov. 2015.

21.   S. Utsuki *et al.*, "Possibility of using laser spectroscopy for the intraoperative detection of nonfluorescing brain tumors and the boundaries of brain tumor infiltrates," *J. Neurosurg.*, vol. 104, no. 4, pp. 618–620, Apr. 2006.

22.   S. Utsuki *et al.*, "Histological Examination of False Positive Tissue Resection Using 5-Aminolevulinic Acid-Induced Fluorescence Guidance," *Neurol. Med. Chir. (Tokyo)*, vol. 47, no. 5, pp. 210–214, 2007.

23.   L.-C. Huang *et al.*, "Glioblastoma cells labeled by robust Raman tags for enhancing imaging contrast," *Biomed. Opt. Express*, vol. 9, no. 5, p. 2142, May 2018.

24.   M. Reinert *et al.*, "Quantitative Modulation of PpIX Fluorescence and Improved Glioma Visualization," *Front. Surg.*, vol. 6, p. 41, Jul. 2019.

25.   P. A. Valdés, D. W. Roberts, F.-K. Lu, PhD, and A. Golby, "Optical technologies for intraoperative neurosurgical guidance," *Neurosurg. Focus*, vol. 40, no. 3, p. E8, Mar. 2016.

26.   B. Zhang, X. Wang, F. Liu, Y. Cheng, and D. Shi, "Effective Reduction of Nonspecific Binding by Surface Engineering of Quantum Dots with Bovine Serum Albumin for Cell-Targeted Imaging," *Langmuir*, vol. 28, no. 48, pp. 16605–16613, Dec. 2012.

27.   I. P. Santos *et al.*, "Raman spectroscopy for cancer detection and cancer surgery guidance: translation to the clinics," *The Analyst*, vol. 142, no. 17, pp. 3025–3047, 2017.

28.   M. Ji *et al.*, "Rapid, Label-Free Detection of Brain Tumors with Stimulated Raman Scattering Microscopy," *Sci. Transl. Med.*, vol. 5, no. 201, pp. 201ra119-201ra119, Sep. 2013.

29.   S. N. Kalkanis *et al.*, "Raman spectroscopy to distinguish grey matter, necrosis, and glioblastoma multiforme in frozen tissue sections," *J. Neurooncol.*, vol. 116, no. 3, pp. 477–485, Feb. 2014.

30.   M. Jermyn *et al.*, "Intraoperative brain cancer detection with Raman spectroscopy in humans," *Sci. Transl. Med.*, vol. 7, no. 274, pp. 274ra19-274ra19, Feb. 2015.

31.   R. Huang *et al.*, "High Precision Imaging of Microscopic Spread of Glioblastoma with a Targeted Ultrasensitive SERRS Molecular Imaging Probe," *Theranostics*, vol. 6, no. 8, pp. 1075–1084, 2016.

32.   X. Gao *et al.*, "Guiding Brain-Tumor Surgery via Blood-Brain-Barrier-Permeable Gold Nanoprobes with Acid-Triggered MRI/SERRS Signals," *Adv. Mater.*, vol. 29, no. 21, p. 1603917, Jun. 2017.

33.   N. D. Israelsen, C. Hanson, and E. Vargis, "Nanoparticle Properties and Synthesis Effects on Surface-Enhanced Raman Scattering Enhancement Factor: An Introduction," *Sci. World J.*, vol. 2015, pp. 1–12, 2015.

34.   T. A. Zdobnova, E. N. Lebedenko and S. M. Deyev, "Quantum Dots for Molecular Diagnostics of Tumors," *Acta Naturae*, vol. 3, no. 1, pp. 29–47, Mar. 2011.

35.   R. P. Bagwe, L. R. Hilliard, and W. Tan, "Surface Modification of Silica Nanoparticles to Reduce Aggregation and Nonspecific Binding," *Langmuir*, vol. 22, no. 9, pp. 4357–4362, Apr. 2006.

36. E. C. Le Ru and P. G. Etchegoin, *Principles of surface-enhanced Raman spectroscopy: and related plasmonic effects*, 1st ed. Amsterdam ; Boston: Elsevier, 2009.

37. "Theory of Raman Scattering - B&W Tek." https://bwtek.com/raman-theory-of-raman-scattering/.

38. L. Wei and W. Min, "Electronic Preresonance Stimulated Raman Scattering Microscopy," *J. Phys. Chem. Lett.*, vol. 9, no. 15, pp. 4294–4301, Aug. 2018.

39. "What is resonance Raman spectroscopy? - HORIBA." https://www.horiba.com/us/en/scientific/products/ramanspectroscopy/raman academy/raman-faqs/what-is-resonance-raman-spectroscopy/.

40. C. S. Liao and J. X. Cheng, "Probing Cancer by Exploiting Spontaneous and Stimulated Raman Scattering". https://www.photonics.com/Articles/Probing_ Cancer_ by_ Exploiting_ Spontaneous_ and/a61678.

41. "International Journal of Engineering and Technical Research (IJETR)," *Raman Spectrosc.*, vol. 6, no. 1, p. 16, 2016.

42. F. Madzharova, Z. Heiner, and J. Kneipp, "Surface enhanced hyper Raman scattering (SEHRS) and its applications," *Chem. Soc. Rev.*, vol. 46, no. 13, pp. 3980–3999, 2017.

43. H. Wei, S. M. Hossein Abtahi, and P. J. Vikesland, "Plasmonic colorimetric and SERS sensors for environmental analysis," *Environ. Sci. Nano*, vol. 2, no. 2, pp. 120–135, 2015.

44. T. Yin, L. Jiang, and Z. Shen, "Recent progress on photoluminescence from plasmonic nanostructures: Phenomenon, mechanism, and application," *Chin. Phys. B*, vol. 27, no. 9, p. 097803, Sep. 2018.

45. E. Petryayeva and U. J. Krull, "Localized surface plasmon resonance: Nanostructures, bioassays and biosensing—A review," *Anal. Chim. Acta*, vol. 706, no. 1, pp. 8–24, Nov. 2011.

46. A. J. McQuillan, "The discovery of surface-enhanced Raman scattering," *Notes Rec. R. Soc.*, vol. 63, no. 1, pp. 105–109, Mar. 2009.

47. Pilot, Signorini, Durante, Orian, Bhamidipati, and Fabris, "A Review on Surface-Enhanced Raman Scattering," *Biosensors*, vol. 9, no. 2, p. 57, Apr. 2019.

48. S. Abalde-Cela, P. Aldeanueva-Potel, C. Mateo-Mateo, L. Rodríguez-Lorenzo, R. A. Alvarez-Puebla, and L. M. Liz-Marzán, "Surface-enhanced Raman scattering biomedical applications of plasmonic colloidal particles," *J. R. Soc. Interface*, vol. 7, no. suppl_4, Aug. 2010.

49.   M. Moskovits, "Surface-enhanced Raman spectroscopy: a brief retrospective," *J. Raman Spectrosc.*, vol. 36, no. 6–7, pp. 485–496, Jun. 2005.

50.   J. A. Dieringer *et al.*, "Introductory Lecture : Surface enhanced Raman spectroscopy: new materials, concepts, characterization tools, and applications," *Faraday Discuss*, vol. 132, pp. 9–26, 2006.

51.   N. Gandra and S. Singamaneni, "Bilayered Raman-Intense Gold Nanostructures with Hidden Tags (BRIGHTs) for High-Resolution Bioimaging," *Adv. Mater.*, vol. 25, no. 7, pp. 1022–1027, Feb. 2013.

52.   G. von Maltzahn *et al.*, "SERS-Coded Gold Nanorods as a Multifunctional Platform for Densely Multiplexed Near-Infrared Imaging and Photothermal Heating," *Adv. Mater.*, vol. 21, no. 31, pp. 3175–3180, Aug. 2009.

53.   X. Qian *et al.*, "In vivo tumor targeting and spectroscopic detection with surface-enhanced Raman nanoparticle tags," *Nat. Biotechnol.*, vol. 26, no. 1, pp. 83–90, Jan. 2008.

54.   S. Lee *et al.*, "Biological Imaging of HEK293 Cells Expressing PLCγ1 Using Surface-Enhanced Raman Microscopy," *Anal. Chem.*, vol. 79, no. 3, pp. 916–922, Feb. 2007.

55.   X. Qian, S. R. Emory, and S. Nie, "Anchoring Molecular Chromophores to Colloidal Gold Nanocrystals: Surface-Enhanced Raman Evidence for Strong Electronic Coupling and Irreversible Structural Locking," *J. Am. Chem. Soc.*, vol. 134, no. 4, pp. 2000–2003, Feb. 2012.

56.   K. K. Maiti *et al.*, "Development of biocompatible SERS nanotag with increased stability by chemisorption of reporter molecule for in vivo cancer detection," *Biosens. Bioelectron.*, vol. 26, no. 2, pp. 398–403, Oct. 2010.

57.   L. Jiang, J. Qian, F. Cai, and S. He, "Raman reporter-coated gold nanorods and their applications in multimodal optical imaging of cancer cells," *Anal. Bioanal. Chem.*, vol. 400, no. 9, pp. 2793–2800, Jul. 2011.

58.   S. Keren, C. Zavaleta, Z. Cheng, A. de la Zerda, O. Gheysens, and S. S. Gambhir, "Noninvasive molecular imaging of small living subjects using Raman spectroscopy," *Proc. Natl. Acad. Sci.*, vol. 105, no. 15, pp. 5844–5849, Apr. 2008.

59.   J. V. Jokerst, T. Lobovkina, R. N. Zare, and S. S. Gambhir, "Nanoparticle PEGylation for imaging and therapy," *Nanomed.*, vol. 6, no. 4, pp. 715–728, Jun. 2011.

60.   C.-C. Huang, C.-H. Huang, I.-T. Kuo, L.-K. Chau, and T.-S. Yang, "Synthesis of silica-coated gold nanorod as Raman tags by modulating cetyltrimethylammonium bromide concentration," *Colloids Surf. Physicochem. Eng. Asp.*, vol. 409, pp. 61–

68, Sep. 2012.

61.   R. Karim, C. Palazzo, B. Evrard, and G. Piel, "Nanocarriers for the treatment of glioblastoma multiforme: Current state-of-the-art," *J. Controlled Release*, vol. 227, pp. 23–37, Apr. 2016.

62.   A. Meola, J. Rao, N. Chaudhary, M. Sharma, and S. D. Chang, "Gold Nanoparticles for Brain Tumor Imaging: A Systematic Review," *Front. Neurol.*, vol. 9, p. 328, May 2018.

63.   B. Aslan, B. Ozpolat, A. K. Sood, and G. Lopez-Berestein, "Nanotechnology in cancer therapy," *J. Drug Target.*, vol. 21, no. 10, pp. 904–913, Dec. 2013.

64.   R. A. Petros and J. M. DeSimone, "Strategies in the design of nanoparticles for therapeutic applications," *Nat. Rev. Drug Discov.*, vol. 9, no. 8, pp. 615–627, Aug. 2010.

65.   W. H. De Jong, W. I. Hagens, P. Krystek, M. C. Burger, A. J. A. M. Sips, and R. E. Geertsma, "Particle size-dependent organ distribution of gold nanoparticles after intravenous administration," *Biomaterials*, vol. 29, no. 12, pp. 1912–1919, Apr. 2008.

66.   A. B. Etame, C. A. Smith, W. C. W. Chan, and J. T. Rutka, "Design and potential application of PEGylated gold nanoparticles with size-dependent permeation through brain microvasculature," *Nanomedicine Nanotechnol. Biol. Med.*, vol. 7, no. 6, pp. 992–1000, Dec. 2011.

67.   H. Chen *et al.*, "'Living' PEGylation on gold nanoparticles to optimize cancer cell uptake by controlling targeting ligand and charge densities," *Nanotechnology*, vol. 24, no. 35, p. 355101, Sep. 2013.

68.   J. V. Jokerst, Z. Miao, C. Zavaleta, Z. Cheng, and S. S. Gambhir, "Affibody-Functionalized Gold-Silica Nanoparticles for Raman Molecular Imaging of the Epidermal Growth Factor Receptor," *Small*, vol. 7, no. 5, pp. 625–633, Mar. 2011.

69.   M. L. Goodenberger and R. B. Jenkins, "Genetics of adult glioma," *Cancer Genet.*, vol. 205, no. 12, pp. 613–621, Dec. 2012.

70.   P. Wesseling and D. Capper, "WHO 2016 Classification of gliomas," *Neuropathol. Appl. Neurobiol.*, vol. 44, no. 2, pp. 139–150, Feb. 2018.

71.   C. Adamson *et al.*, "Glioblastoma multiforme: a review of where we have been and where we are going," *Expert Opin. Investig. Drugs*, vol. 18, no. 8, pp. 1061–1083, Aug. 2009.

72.   G. Perazzoli *et al.*, "Temozolomide Resistance in Glioblastoma Cell Lines: Implication of MGMT, MMR, P-Glycoprotein and CD133 Expression," *PLOS ONE*,

vol. 10, no. 10, p. e0140131, Oct. 2015.

73. J. J. Corso, E. Sharon, S. Dube, S. El-Saden, U. Sinha, and A. Yuille, "Efficient Multilevel Brain Tumor Segmentation With Integrated Bayesian Model Classification," *IEEE Trans. Med. Imaging*, vol. 27, no. 5, pp. 629–640, May 2008.

74. J. Siddiqui and A. S. Krishnan, "Butterfly Glioma," *N. Engl. J. Med.*, vol. 378, no. 3, pp. 281–281, Jan. 2018.

75. M. Scaltriti, "The Epidermal Growth Factor Receptor Pathway: A Model for Targeted Therapy," *Clin Cancer Res*, p. 6, 2006.

76. H. Xu *et al.*, "Epidermal growth factor receptor in glioblastoma," *Oncol. Lett.*, vol. 14, no. 1, pp. 512–516, Jul. 2017.

77. M. McNamara, S. Sahebjam, and W. Mason, "Emerging Biomarkers in Glioblastoma," *Cancers*, vol. 5, no. 4, pp. 1103–1119, Aug. 2013.

78. H. K. Gan, A. N. Cvrljevic, and T. G. Johns, "The epidermal growth factor receptor variant III (EGFRvIII): where wild things are altered," *FEBS J.*, vol. 280, no. 21, pp. 5350–5370, Nov. 2013.

79. T. E. Taylor, F. B. Furnari, and W. K. Cavenee, "Targeting EGFR for Treatment of Glioblastoma: Molecular Basis to Overcome Resistance," *Curr. Cancer Drug Targets*, vol. 12, no. 3, pp. 197–209, Mar. 2012.

80. H. K. Gan, A. H. Kaye, and R. B. Luwor, "The EGFRvIII variant in glioblastoma multiforme," *J. Clin. Neurosci.*, vol. 16, no. 6, pp. 748–754, Jun. 2009.

81. "Biopsy versus resection for high-grade glioma." /CD002034/GYNAECA_biopsy-versus-resection-high-grade-glioma.

82. K. L. Chaichana *et al.*, "When Gross Total Resection of a Glioblastoma Is Possible, How Much Resection Should Be Achieved?," *World Neurosurg.*, vol. 82, no. 1–2, pp. e257–e265, Jul. 2014.

83. K. L. Chaichana *et al.*, "Establishing percent resection and residual volume thresholds affecting survival and recurrence for patients with newly diagnosed intracranial glioblastoma," *Neuro-Oncol.*, vol. 16, no. 1, pp. 113–122, Jan. 2014.

84. "Glioblastoma Multiforme – Symptoms, Diagnosis and Treatment Options." https://www.aans.org/.

85. R. Stupp *et al.*, "Radiotherapy plus Concomitant and Adjuvant Temozolomide for Glioblastoma," *N. Engl. J. Med.*, p. 10, 2005.

86. "Chemotherapy/American Brain Tumor Association" http://ww.abta.org/brain-

tumor-treatment/treatments/chemoterapy.html

87.   U. Weinberg, "Novocure's Tumor Treating Fields: Innovative brain cancer therapy with survival and safety benefits," p. 4.

88.   R. Stupp *et al.*, "Effect of Tumor-Treating Fields Plus Maintenance Temozolomide vs Maintenance Temozolomide Alone on Survival in Patients With Glioblastoma: A Randomized Clinical Trial," *JAMA*, vol. 318, no. 23, p. 2306, Dec. 2017.

89.   L. Orellana, A. Hospital, and M. Orozco, "Oncogenic mutations of the EGF-Receptor ectodomain reveal an unexpected mechanism for ligand-independent activation," Biophysics, preprint, Sep. 2014.

90.   S. J. Bagley, A. S. Desai, G. P. Linette, C. H. June, and D. M. O'Rourke, "CAR T-cell therapy for glioblastoma: recent clinical advances and future challenges," *Neuro-Oncol.*, vol. 20, no. 11, pp. 1429–1438, Oct. 2018.

91.   Y. Cheng *et al.*, "Blood-Brain Barrier Permeable Gold Nanoparticles: An Efficient Delivery Platform for Enhanced Malignant Glioma Therapy and Imaging," *Small*, p. n/a-n/a, Aug. 2014.

92.   A. Appelt-Menzel *et al.*, "Establishment of a Human Blood-Brain Barrier Co-culture Model Mimicking the Neurovascular Unit Using Induced Pluri- and Multipotent Stem Cells," *Stem Cell Rep.*, vol. 8, no. 4, pp. 894–906, Apr. 2017.

93.   J. J. Jamieson, P. C. Searson, and S. Gerecht, "Engineering the human blood-brain barrier in vitro," *J. Biol. Eng.*, vol. 11, no. 1, p. 37, Dec. 2017.

94.   B. T. Hawkins and T. P. Davis, "The Blood-Brain Barrier/Neurovascular Unit in Health and Disease," *Pharmacol. Rev.*, vol. 57, no. 2, pp. 173–185, Jun. 2005.

95.   D. M. Long, "Capillary Ultrastructure and the Blood-Brain Barrier in Human Malignant Brain Tumors," *J. Neurosurg.*, vol. 32, no. 2, pp. 127–144, Feb. 1970.

96.   D. Y. Joh *et al.*, "Selective Targeting of Brain Tumors with Gold Nanoparticle-Induced Radiosensitization," *PLoS ONE*, vol. 8, no. 4, p. e62425, Apr. 2013.

97.   F. ELAmrawy, A. A. Othman, C. Adkins, A. Helmy, and M. I. Nounou, "Tailored nanocarriers and bioconjugates for combating glioblastoma and other brain tumors," *J. Cancer Metastasis Treat.*, vol. 2, no. 3, p. 112, Mar. 2016.

98.   A. B. Etame, R. J. Diaz, C. A. Smith, T. G. Mainprize, K. Hynynen, and J. T. Rutka, "Focused ultrasound disruption of the blood-brain barrier: a new frontier for therapeutic delivery in molecular neurooncology," *Neurosurg. Focus*, vol. 32, no. 1, p. E3, Jan. 2012.

99.   B. G. Harder *et al.*, "Developments in Blood-Brain Barrier Penetrance and Drug

Repurposing for Improved Treatment of Glioblastoma," *Front. Oncol.*, vol. 8, p. 462, Oct. 2018.

100. W. Debinski and S. B. Tatter, "Convection-enhanced delivery for the treatment of brain tumors," *Expert Rev. Neurother.*, vol. 9, no. 10, pp. 1519–1527, Oct. 2009.

101. D. Ye *et al.*, "Nanoparticle accumulation and transcytosis in brain endothelial cell layers," *Nanoscale*, vol. 5, no. 22, p. 11153, 2013.

102. B. B. Weksler *et al.*, "Blood-brain barrier-specific properties of a human adult brain endothelial cell line," *FASEB J.*, vol. 19, no. 13, pp. 1872–1874, Nov. 2005.

103. E. A. L. M. Biemans, L. Jäkel, R. M. W. de Waal, H. B. Kuiperij, and M. M. Verbeek, "Limitations of the hCMEC/D3 cell line as a model for Aβ clearance by the human blood-brain barrier: Limitations hCMEC/D3 Model to Study Aβ Clearance," *J. Neurosci. Res.*, vol. 95, no. 7, pp. 1513–1522, Jul. 2017.

104. G. Xu, S. Mahajan, I. Roy, and K.-T. Yong, "Theranostic quantum dots for crossing blood–brain barrier in vitro and providing therapy of HIV-associated encephalopathy," *Front. Pharmacol.*, vol. 4, 2013.

105. Y. Shao, C. Li, Y. Feng, and W. Lin, "Surface-enhanced Raman scattering and density functional theory study of 1,4-benzenedithiol and its silver complexes," *Spectrochim. Acta. A. Mol. Biomol. Spectrosc.*, vol. 116, pp. 214–219, Dec. 2013.

106. S. W. Joo, S. W. Han, and K. Kim, "Adsorption of 1,4-Benzenedithiol on Gold and Silver Surfaces: Surface-Enhanced Raman Scattering Study," *J. Colloid Interface Sci.*, vol. 240, no. 2, pp. 391–399, Aug. 2001.

107. M. Mioc *et al.*, "The Cytotoxic Effects of Betulin-Conjugated Gold Nanoparticles as Stable Formulations in Normal and Melanoma Cells," *Front. Pharmacol.*, vol. 9, p. 429, May 2018.

108. E. L. Bentzen *et al.*, "Surface Modification To Reduce Nonspecific Binding of Quantum Dots in Live Cell Assays," *Bioconjug. Chem.*, vol. 16, no. 6, pp. 1488–1494, Nov. 2005.

109. B. A. Kairdolf, M. C. Mancini, A. M. Smith, and S. Nie, "Minimizing Nonspecific Cellular Binding of Quantum Dots with Hydroxyl-Derivatized Surface Coatings," *Anal. Chem.*, vol. 80, no. 8, pp. 3029–3034, Apr. 2008.

110. N. A. Byzova, I. V. Safenkova, E. S. Slutskaya, A. V. Zherdev, and B. B. Dzantiev, "Less is More: A Comparison of Antibody–Gold Nanoparticle Conjugates of Different Ratios," *Bioconjug. Chem.*, vol. 28, no. 11, pp. 2737–2746, Nov. 2017.

111. D. R. Elias, A. Poloukhtine, V. Popik, and A. Tsourkas, "Effect of ligand density,

receptor density, and nanoparticle size on cell targeting," *Nanomedicine Nanotechnol. Biol. Med.*, vol. 9, no. 2, pp. 194–201, Feb. 2013.

List of abbreviations

Abbreviation	Full name
1,4-BDT	1,4-Benzenedithiol
3D	Three dimensions
5-ALA	5-aminolevulinic acid
AMT	Absorption mediated transport
aPEG	Amino polyethylene glycol methoxy
BBB	Blood brain barrier
BSA	Bovine serum albumin
BTB	Brain tumor barrier
CARS	Coherent anti-Stokes Raman scattering
cPEG	Carboxy polyethylene glycol thiol
CT	Computerized tomography
DMEM	Dulbecco's modified Eagle's medium
DMSO	Dimethyl sulfoxide
EDC	Ethyl dimethylaminopropyl carbodiimide
EDTA	Ethylenediaminetetraacetic acid
EGFR	Epidermal growth factor receptor
EPR	Enhanced retention and permeability
FCS	Fetal calf serum
FECH	Ferrochelatase
FUS	Focused ultrasound
GA	Glutaraldehyde
GBM	Glioblastoma
GNP	Gold nanoparticle
HEPES	4-(2-hydroxyethyl)-1-piperazineethanesulfonic acid
HO-1	Heme oxygenase-1
ICG	Indocyanine green
ICP-MS	Inductively coupled plasma mass spectrometry

IDH	Isocitrate dehydrogenase
iMRI	Intraoperative magnetic resonance imaging
iUS	Intraoperative ultrasonography
LSPR	Localized surface plasmon resonance
LY	Lucifer yellow
MFI	Mean fluorescence intensity
MG	Malachite green
MGITC	Malachite green isothiocyanate
mPEG	Methoxy polyethylene glycol thiol
MRI	Magnetic resonance imaging
NDS	Normal donkey serum
NIR	Near-infrared
NOS	Not otherwise specified
OD	Optical density
P/S	Penicillin/streptomycin
Papp	Apparent permeability
PBS	Phosphate buffered saline
PBS-T	Phosphate buffered saline Tween
PEG	Polyethylene glycol
PET	Positron emission tomography
PFA	Paraformaldehyde
PIPES	Piperazine-N,N'-bis(2-ethanesulfonic acid)
PPIX	Protoporphyrin IX
PVDF	Polyvinylidene difluoride
QD	Quantum dot
qFACS	Quantitative fluorescence-activated cell sorting
RES	Reticuloendothelial system
RMT	Receptor mediated transcytosis
RRS	Resonance Raman scattering
RT	Room temperature
SD	Standard deviation

SERRS	Surface enhanced resonance Raman spectroscopy
SEHRS	Surface enhanced hyper Raman scattering
SERS	Surface enhanced Raman spectroscopy
SPR	Surface plasmon resonance
SRS	Stimulated Raman scattering
Sulfo-NHS	N-hydroxysulfosuccinimide
TEER	Transendothelial electrical resistance
TERS	Tip enhanced Raman spectroscopy
TJ	Tight junction
TMZ	Temozolomide
TTF	Tumor treating field
UV-Vis	Ultraviolet-visible
WHO	World health organization
ZO	Zonula occludens

Acknowledgments

My professor always says: "Ph.D. is a roller coaster with many up and even more down". He is right since this experience drove me through moments with several mixed emotions. I doubted I was good enough and I wondered whether it was worth carrying out the same experiment again and again to achieve the desired outcomes. However, If I could go back, I would do it again because it raised the awareness of myself. More importantly, I had the chance to meet special people, some of which are currently part of my life.

I want to start by expressing my deepest gratitude to my supervisors, Uwe Pieles and Michael Reinert, who always trusted me and my work, and to Jörg Huwyler, who kindly accepeted to be my co-referee.

I want to thank many other people who differently contributed to this experience. Luigi Mariani and Laura Suter-Dick kindly welcomed me in their laboratories. Felix, with the machine "Paula", carried out the ICP analysis of my sticky samples and took time to understand the incomprehensible results. Luc Stoppini and Adrien Roux kindly allowed me to use their TEER system and provided the cells. Monica Schönenberger and Nils Warfving kindly let me use the Raman and the dark field microscopes, respectively. Theo taught me to use the Raman microscope. Carine Gaiser, all members of the Nanoteam (specially Sina, Theo, Marcus, Lucy, Jochen, Franzi, Lena and Ana Bela) and the BTB team (Marie-Françoise, Cris, Jean-Louis, Tala, Thomas, Philips, Anna and Simona) made the laboratory a pleasant place to work in.

Alessandra, Anna, Marta, Christel, Yasmin and Salima always cheered me up during difficult times in and outside the lab. Deborah warmly welcomed me whenever I was in Lugano.

My heartfelt thanks go to two ladies mentioned above, who specially supported me during the whole experience. Marie-Françoise, with your empathy and friendly attitude, you put me at ease right away. There never was a time you refused to help me. Thank you for the funny moments spent in the lab and for letting me know the song "Can't you feel it". Sina, with your constructive criticism and advises, you pushed me to be a better scientist. You believed in me more than I did. I want you both to know that your human and scientific support was crucial throughout the completion of this research project and personal development.

It is time to thank those people who have been with me for a very long time. Noemi, with your sensitivity and the right words at the right time, you always made me feel better over the last 25 years. Giuliana, Vincenzo and Rosi, you listened to me every single time I was disappointed, sad or happy.

I must express my deepest admiration and gratitude to my mother, Rosita, my father, Claudio and my brother, Daniele. You always encouraged me to find my way although it took me far from you and you opened your arms whenever I came back home. I thank you for showing me that is possible to move on even in the darkest moments when there are unconditional love and mutual support.

Finally, Raffaele, you patiently endured all my mood swings and stood by me even when changing direction would have been much easier. With your different attitude, you helped me to give due weight to each situation and to be less uncompromising.

Curriculum vitae

Personal information

Floriana Burgio

01.06.1989

Italian

Work experience

Sept. 2015 - Nov. 2019	Ph.D. in Neurobiology, University of Basel. Joined Ph.D. between University of Applied Sciences Northwestern Switzerland (Muttenz, CH), Department of Biomedicine (Basel, CH) and Ente Ospedaliero Cantonale (Lugano, CH).

Education

Oct. 2012 - Mar. 2015	Master degree in Biotecnologie per l'industria e la ricerca scientica, University of study of Palermo (Palermo, IT). Thesis: *Osteoinduction and survival of human osteosarcoma cells on hydroxyapatite scaffolds under static and dynamic culture conditions.*
Oct.2013 - Oct. 2014	Visiting Erasmus student at the University of Applied Sciences Northwestern Switzerland (Muttenz, CH).
Oct.2008 - Oct. 2012	Beachelor degree in Biotecnologie, University of study of Palermo (Palermo, IT). Thesis: *Evaluation of the activity of two recombinant collagenases derived from Clostridium histolyticum.*

Publications

- Burgio F, Piffaretti D, Schmidt F, Pieles U, Reinert M, Ritz M-F, Saxer S. Tuning the Surface Chemistry of Gold Nanoparticles to Specifically Image Glioblastoma Cells Using Surface-Enhanced Raman Spectroscopy. *ACS Appl. Nano Mater*. Feb. 2020.

- Piffaretti D, Burgio F, Thelen M, Lang AK, Paganetti P, Reinert M, D'Angelo ML. Protoporphyrin IX tracer fluorescence modulation for improved brain tumor cell lines visualization. *J Photochem Photobiol B*. Oct. 2019.

- Brodard P, Dabros M, Marti R, Vanoli E, Zinn M, Frey U, Adlhart C, Kind L, Koch F, Burgio F, Stenqvist J, Saxer S, Pieles U, Shahgaldian P, Wenderborn S. Material Science at Swiss Universities of Applied Sciences. *Chimia International Journal for Chemistry*. Aug. 2019.

- Burgio F, Rimmer N, Pieles U, Buschmann J, Beaufils-Hugot M. Characterization and in ovo vascularization of a 3D-printed hydroxyapatite scaffold with different extracellular matrix coatings under perfusion culture. *Biol Open*. Oct. 2018.

- Burgio F, Piffaretti D, Mariani L, Pieles U, Reinert M. P04.06 Gold nanoparticles development for Raman guided Glioblastoma visualization during surgical resection. *Neuro Oncol*. May 2017.

- Fontana AO, Piffaretti D, Marchi F, Burgio F, Faia-Torres AB, Paganetti P, Pintos S, Pieles U, Reinert M. Epithelial growth factor receptor expression influences 5-ALA induced glioblastoma fluorescence. *J Neurooncol*. May 2017.

Conferences

- Oral presentation at the 8th Swiss Raman user meeting, Nov. 2019, Muttenz (CH).

- Oral presentation at the International Conference On Nanomedicine and Nanobiotechnology, Sept. 2018, Roma (IT).

- Poster presentation at the 14th Confocal Raman Imaging Symposium, Sept. 2017, Ulm (DE).

- Poster presentation at the World Federation of Neuro-Oncology Societies Conference, May 2017, Zürich (CH).

- 7th Research Day of Southern Switzerland, Apr. 2017, Lugano (CH).

- Poster presentation at the Biointerface International Conference, Aug. 2016, Zürich (CH).

- Poster presentation at the 6th Research Day of Southern Switzerland, Apr. 2016, Lugano (CH).

- Rapid fire presentation at the Raman Microscopy Workshop, ETH Zürich, Feb. 2016, Zürich (CH).

- Poster presentation and rapid-fire presentation at the 26th Annual Conference of the European Society for Biomaterials, Aug. 2014, Liverpool (UK).
- Poster presentation at the 20th Annual Meeting of the Swiss Society for Biomaterials and Regenerative Medicine, May 2014, Basel (CH).
- 8th International Summer School on Advanced Biotechnology, Sept. 2013, Innsbrück (A).